POLITECNICO
MILANO 1863

SCUOLA DI INGEGNERIA INDUSTRIALE
E DELL'INFORMAZIONE

Method of characteristics to design symmetric and asymmetric converging-diverging nozzles for real gas applications

Tesi di Laurea Magistrale in
Mechanical Engineering - Ingegneria Meccanica

Author: **Riccardo Gioia**

Student ID: 989879
Advisor: Prof. Alessandro Romei
Co-advisors: Dr. Noraiz Mushtaq
Academic Year: 2022-23

Acknowledgements

I would like to express my sincere gratitude to my parents for their constant support throughout this five-year journey.

Additionally, I extend my sincere thanks to my advisor, Professor Alessandro Romei, for proposing this challenging and captivating topic and providing essential guidance during my master thesis. I am also grateful for the valuable assistance and support from Dr. Noraiz Mushtaq.

Finally, I want to acknowledge and thank all my friends who have been part of my life both within and outside the university over the past five years. A special note of thanks goes to Andrea, my steadfast companion throughout all the projects I undertook during my university studies.

Abstract

The purpose of this thesis is to develop methods of characteristics (MoC). The methods include both symmetric and asymmetric formulations and are applied to the design of converging-diverging planar nozzle and nozzle cascades, which expand both ideal and non-ideal flows.

To account for non-ideal flow features, the traditional MoC based on the Hoffman theory is recast in terms of the generalized isentropic coefficient. The reliability of the developed MoC is verified through dedicated computational fluid dynamic (CFD) simulations in Ansys Fluent, demonstrating the ability to accomplish efficient supersonic expansions of non-ideal flows without the formation of shocks.

In the final part, the MoC was extended to the design of nozzle cascades for supersonic turbine applications. A method for the implementation of blades with asymmetric MoC is also devised and implemented, in addition to the conventional design method based on the symmetric MoC. Viscous CFD simulations have shown that symmetric MoC remains the preferred method over the asymmetric MoC as the designed blades exhibit lower losses (the pressure loss coefficients are 19.3% for symmetric MoC, against 24.3 % for the asymmetric one in the worst-case scenario). However, the method presented here for the blade design with asymmetric MoC is still preliminary, and the flexibility of this method may have unexplored potential to allow the design of more efficient vanes.

Keywords: method of characteristics, converging-diverging nozzle, non-ideal flows, supersonic turbines

Sommario

Lo scopo di questa tesi è di sviluppare metodi delle caratteristice (MoC). I metodi sviluppati includono formulazioni sia simmetriche che asimmetriche e sono applicati alla progettazione di ugelli planari convergenti-divergenti e schiere di pale statoriche, che espandono flussi ideali e non.

Per considerare gli effetti di flussi non ideali, il MoC tradizionale basato sulla teoria formulata da Hoffman è riformulato basandosi sul coefficiente isentropico generalizzato. L'affidabilità del MoC appena sviluppato è verificata attraverso simulazioni di fluidodinamica computazionale (CFD) dedicate, dimostrando che è in grado di realizzare ugelli che garantiscono un'efficiente espansione di flussi non ideali senza la formazione di shock.

Nella parte finale, il MoC è esteso alla progettazione di statori per turbine supersoniche. Un metodo che permette la realizzazione di pale con MoC asimmetrico è ideato e implementato, in aggiunta al metodo utilizzato convenzionalmente, basato sul MoC simmetrico. Simulazioni fluidodinamiche viscose hanno dimostrato che il MoC simmetrico rimane il metodo preferibile rispetto all'asimmetrico, in quanto le pale disegnate basandosi sul primo mostrano minori perdite (per esempio, nel caso peggiore trattato, il coefficiente di perdita basato sulla pressione è 19.3% per il simmetrico rispetto a 24.3% per l'asimmetrico). Comunque, il metodo presentato in questa tesi basato sul MoC asimmetrico è ancora preliminare e la flessibilita garantita da esso potrebbe celare un potenziale inesplorato per il design di statori più efficienti.

Parole chiave: metodo nelle caratteristiche , ugello convergente-divergente, flussi non ideali, turbine supersoniche

Summary

List of Figures

List of Tables

1 | Introduction

Today all of humanity is confronting one of the most complex and crucial challenges in its history: finding a way to limit and, if possible, halt climate change. The author believes that this fundamental goal has to be reached without compromising the quality of life of the wealthier part of the society, and, at the same time, allowing the poorer part of the people to reach equivalent life quality.

One of the main factors that has guaranteed an enhancement in the quality of life is for sure electricity. As highlighted by the IEA World Energy Outlook [1], in the next years an increase in electric energy consumption is expected. This trend is linked to the rise of the energy demand in emerging markets, caused by the increase in the average wealth. Additionally, there is a growing need for clean energy among end-users, facilitating the decarbonization of sectors where fossil fuels, such as transport and heating, currently predominate. To give an example, in a net zero scenario, the electricity produced is expected to grow by two-and-half-times compared to the production in 2021.

This implies that this sector is facing two challenges: increase production and, at the same time, decarbonize it. To address both challenges, low-emission sources of electricity must expand rapidly, reaching 75% of the total generation by 2030, almost twice in share of 2021. This increase is led mainly by wind and solar PV, with a combined total share in electricity production passing from 10% in 2021 to 70% in 2050.

These two technologies present two limitations that, if not accurately addressed, may render it impossible to maintain energy security: they are non-dispatchable and have low power density [2]. These limitations involve the necessity of the incorporation of dispatchable low-emission technologies, which can either be renewable, such as hydropower, geothermal, and bioenergy, or based on fossil fuels but with technologies enabling emissions reduction, such as the utilization of low-emissions hydrogen and ammonia in natural gas and coal plants, or addition of carbon capture technologies. A comprehensive discussion of this issue is provided in [3] and [4], where to ensure the continuity of electricity production, the use of natural gas is suggested as a temporary solution, which needs to be phased out in the second half of the 21^{st} century.

The decarbonization of the transport sector, responsible for 40 % of the total emissions from end-use sectors, will be obtained through different technologies. While the electrification trend is certain in land transport, encompassing both road and railway, the same cannot be said for the aviation industry. In aviation, the main trend involves substituting jet kerosene with sustainable aviation fuel, such as biojet kerosene or hydrogen, coupled with a decrease in its use as a transport method. This reduction is attributed to both a decline in business trips and a shift towards high-speed rail [1].

It is also important to underline that the increase in electric energy production through low-emission sources has to be supported by an overhaul increase of the efficiency of both the production and use phases. This necessity is higher for example in the industrial sector [1], where this is not limited to only electricity, but also to the use of materials and other types of energy, such as heat.

In this scenario, the demand for nonconventional turbomachinery is destined to rise, serving as a means to support low-power energy sources in energy production or to facilitate emission reduction in the aviation industry. Examples of nonconventional turbomachinery include hydrogen-fire as gas-turbine [5], turbomachinery for supercritical CO_2 [6] and ORC [7] or gas turbines with pressure gain combustor [8].

This interest has to deal with the low readiness level of such turbomachines, implying significant potential for performance improvements, which are not only feasible but recommended [9].

To obtain that, an overall enhancement of design methodology, manufacturing techniques, and materials is necessary. A perfect example of turbomachines that can benefit from this technological advancement are the ones where the flow is transonic and supersonic.

1.1. Supersonic turbines

This type of turbine currently plays a vital role in a series of applications, where the need for a high power output combined with compact size and lightweight design is essential [10] such as military aircraft engines. Other examples may be high expansion ratio steam and gas turbines, small auxiliary turbines, and ORC turbines [2].

The interest in this last technology has risen in the past years, due to the possibility of exploiting low enthalpy sources, where the efficiency of a standard power cycle is not enough to justify the investment, like geothermal, biomass [11], solar radiation [12], waste heat from an industrial process, as steelmaking, heat from the combustion of urban solid waste or heat rejected from other prime movers, as internal combustion engine [13, 14],

turbines or thermodynamic cycle [15]. This possibility makes its role fundamental for the exploitation of dispatchable renewable sources, like geothermal and biomass, as well as enhancing industrial sector efficiency by waste heat recovery.

This interesting possibility is enabled by the use of a variety of organic fluids in substitution of water in a Rankine cycle. The selection of the fluid is usually made through an optimization process, that guarantees the maximum efficiency for a given and fixed maximum cycle temperature. This approach facilitates the utilization of all sources of low-enthalpy heat that would otherwise remain unexploited with traditional technologies due to their low efficiency [7].

While the viability of large-scale ORC power plants has been demonstrated by a series of installations worldwide [11], the same cannot be said for small-scale plants, where the energy conversion efficiency remains low [2]. The only way found today to address this limitation is the use of a single-stage turbine with a very high pressure ratio. This, combined with the low speed of sound of the fluid used [16], results in the presence of a supersonic flow. Consequently, specialized tools are necessary for the design of the blades to avoid shocks, the main cause of low turbine efficiency, leading to both direct losses and the formation of nonuniform flow at the stator outlet. The non-uniformity can also induce structural fatigue and premature failure in the rotor blades [17]. The situation is further complicated by the strong non-ideal gas effects observed inside an ORC turbine, which, as has been proved [18], has a significant impact on turbine efficiency

This master thesis fits within this context as it involves the implementation and verification of a Python code that incorporates the method of characteristics (MoC) with a non-ideal gas model. Initially employed for designing convergent-divergent nozzles [19] under the assumption of ideal flow, the MoC has been employed as a starting point for the design of a nearly shock-free stator [20].

This method has been recently enhanced to account for the presence of non-ideal and dense gas effects [13, 18, 21, 22] due to a renovated interest in high-efficiency supersonic turbine and, more specifically, into the ORC field. The significance of correct stator design, and so the implementation of a method that takes into account all the possible effects, can be demonstrated by considering that, in a single-stage ORC turbine, this component is responsible for two-thirds of the total stage losses [2].

It is important to point out that the MoC developed here, although tested using organic fluids, can be applied in all applications where the non-ideal and dense gas effects have a pivotal role in the gas dynamics of the working fluid and so in the efficiency of the turbine.

1.2. Thesis overview

This work is structured as follows:

- **Chapter 2** explains the theory behind the MoC applied to a supersonic flow. It outlines the implementation of a planar symmetric divergent nozzle in Python. After code verification, the chapter delves into the implementation of a non-ideal gas model. The influence of non-ideal and dense gas effects on the design of a divergent nozzle is discussed.
- **Chapter 3** explores the application of the MoC on a planar asymmetric nozzle. It focuses on the main differences compared to the symmetric case detailed in the previous chapter and on the verification of the new code.
- **Chapter 4**: to illustrate an example of MoC application, the design of a convergent-divergent stator blade is described, both using the previously mentioned symmetric and asymmetric planar MoC, focusing on how this blade is constructed and a brief series of examples.

2 | MoC for the design of a convergent-divergent planar symmetric nozzle

2.1. Derivation of the method of characteristics applied to a supersonic flow

In general, a steady, two-dimensional, planar or axisymmetric, irrotational, flow can be described by three equations [23]:

$$\left(u^2 - c^2\right)\frac{\partial u}{\partial x} + \left(v^2 - c^2\right)\frac{\partial v}{\partial y} + 2uv\frac{\partial u}{\partial y} - \frac{\delta c^2 v}{y} = 0 \tag{2.1}$$

$$\frac{\partial u}{\partial y} - \frac{\partial v}{\partial x} = 0 \tag{2.2}$$

$$c = c\left(V\right) = c\left(u, v\right) \tag{2.3}$$

where the first is the gas dynamic equation (2.1), equation (2.2) is the irrotational condition, and equation (2.3) is a relation that connects the speed of sound with the flow field velocity.

By considering only the first two equations, is possible to notice that they constitute a set of quasi-linear nonhomogeneous partial differential equations of the first order for functions of two independent variables. These variables are the velocity component along the horizontal direction (u) and vertical direction (v) and can be computed supposing that the speed of sound c is known from (2.3) and δ is equal to zero if the flow is planar or equal to 1 if the flow is axisymmetric.

It can be observed that the set of equations is linear with respect to the first partial

derivative of the two independent variables. Therefore the MoC can be used to derive the exact solution more simply, by transforming a partial differential equation into a total differential equation along a specific curve, known as a characteristic curve.

From a mathematical perspective, a characteristic curve, or characteristic, is defined as a curve along which the governing partial differential equation is reduced to an interior operator which is a total differential equation. This interior operator is known as the compatibility equation. Along a characteristic, the dependent variable can take every value that satisfies the compatibility equation. It is also important to note that across a characteristic curve, a physical property is continuous but its derivative may be discontinuous. Thus, regions of flow with continuous properties and derivatives within each region but a discontinuity in the derivatives at their interface may be joined together. An example of this is a Prandtl-Meyer expansion fan that is connected to the uniform upstream and downstream flow regions along Mach lines.

From a physical point of view, a characteristic is defined as the path of propagation of a physical disturbance. If we focus on a supersonic flow field, disturbances propagate along the Mach lines for the flow. It is possible to demonstrate that, for the system of equations defined previously, a characteristic curve is a Mach line.

More specifically, if we applied the mathematical procedure to compute the characteristic equation to the set of equations made by (2.1) and (2.2) we obtain that the characteristics can be computed as: [23, 24]:

$$\lambda_{\pm} = \left(\frac{dy}{dx}\right)_{\pm} = \frac{uv \pm c^2\sqrt{M^2-1}}{u^2-c^2} \tag{2.4}$$

Based on the Mach number (M), the characteristics of the system can be categorized as follows:

- If M>1 there are two real characteristics through each point of the flowfield, and equation (2.1) can be defined as a hyperbolic partial differential equation.
- If M=1 there is one real characteristic through each point of the flow, and equation (2.1) can be defined as a parabolic partial differential equation.
- If M<1 the characteristics are imaginary, and equation (2.1) can be defined as an elliptic partial differential equation.

This implies that this method can be used only to resolve supersonic flow because it is the only case in which two real solutions and, consequently, two real characteristics can be

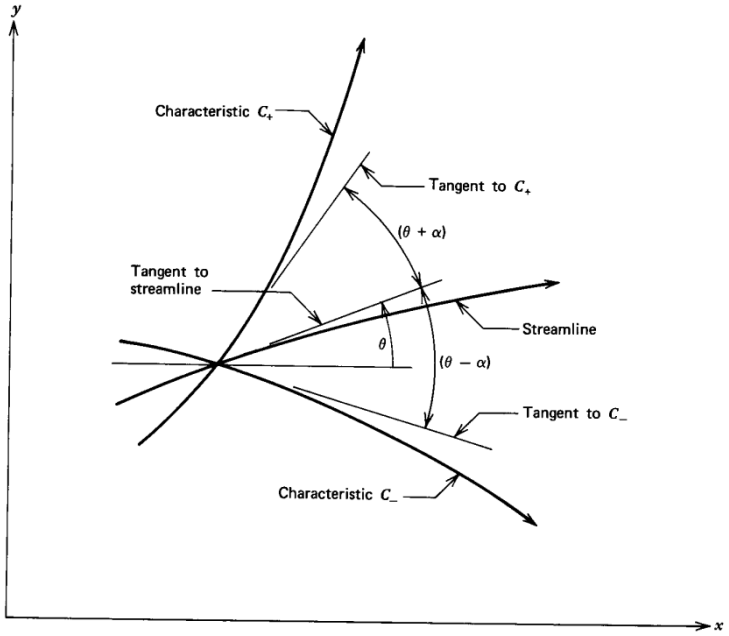

Figure 2.1: Characteristics from a given point in the flow [23].

identified. The detailed motivation because two characteristics are necessary is provided in Section 2.2.

Now, if we focus on equation (2.4) in case of M>1, it is possible to reduce it as:

$$\lambda_{\pm} = \tan(\theta \pm \alpha) \tag{2.5}$$

where:

$$\theta = \arctan\left(\frac{v}{u}\right) \tag{2.6}$$

and

$$\alpha = \arcsin\left(\frac{1}{M}\right) \tag{2.7}$$

Equation (2.5) allows to define two characteristics for every point, known as left-running and right-running characteristics, or C_+ and C_- respectively. These characteristics are functions of the streamlines and the Mach angles. Specifically, C_+ and C_- are at angles α and $-\alpha$ respectively, with respect to the streamline.

The compatibility equation can now be derived by substituting in the system made by

the equations (2.1) and (2.2) the equation (2.4) obtaining:

$$\left(u^2 - c^2\right) du_{\pm} + \left[2uv - \left(u^2 - c^2\right) \lambda_{\pm}\right] dv_{\pm} - \left(\frac{\delta c^2 v}{y}\right) dx_{\pm} = 0 \tag{2.8}$$

This last solution can be also expressed, after some algebraic manipulation, in the form of equation (2.9), as demonstrated by Anderson [24].

$$d\theta = \pm\sqrt{M^2 - 1}\frac{dV}{V} \tag{2.9}$$

This last equation is equal to the one for Prandtl-Meyer flow, and therefore it can be integrated to obtain the Prandtl-Meyer function $\nu(M)$. Thus, the compatibility equation can also be written in an algebraic form along the characteristics:

$$\theta + \nu(M) = const = K_{-} \text{ (along } C_{-}) \tag{2.10}$$

$$\theta - \nu(M) = const = K_{+} \text{ (along } C_{+}) \tag{2.11}$$

where K_{-} and K_{+} are constant along their respective characteristics.

The equations (2.10) and (2.11), also referred to as hodograph characteristics in the literature, describe the relationship between velocity magnitude and direction along a characteristic and may be useful for graphical solutions or hand calculations. Interestingly, these two equations have no information about the spatial coordinates, making them independent of the geometry. This holds only for two-dimensional irrotational cases

This alternative representation of the compatibility equation, even if it is simpler than equation (2.8), requires knowledge of the value of $\nu(M)$. This quantity is straightforward to compute in the case of perfect flow, where a simple algebraic equation exists [24], but not in the case of a non-ideal flow. Various methods have been proposed to compute it, such as an explicit equation by Wheeler and Ong [18], which is formulated under the hypothesis of non-ideal and polytropic fluid. Another approach is presented by Restrepo et al. [25], where the equation of the Prandtl-Meyer angle is iteratively integrated.

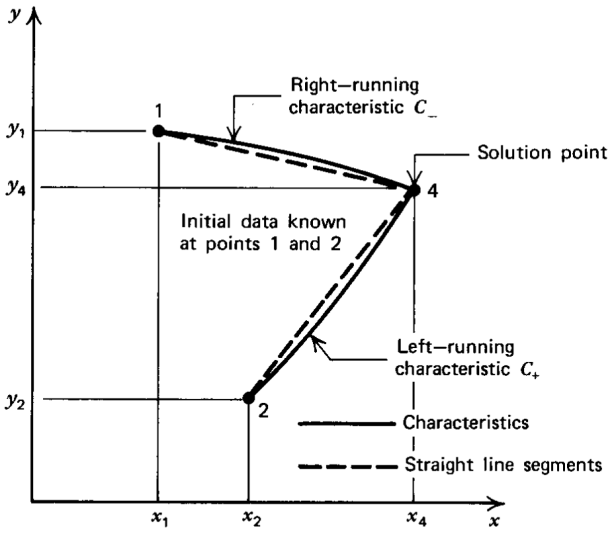

Figure 2.2: Example of the numerical application of the MoC in an interior point unit [23].

2.2. Numerical implementation of the MoC

By applying a finite difference technique is possible to resolve the nonlinear system made by equations (2.5) and (2.8). In practice, is not possible to apply this method to a single point and obtain the independent values of u and v. This is because, for each characteristic, there are two unknowns, u and v, but only one equation, the compatibility one, to define them. This issue can be resolved by computing the position and the velocity, in its magnitude and direction, of a point as the intersection of right and left running characteristics coming from two previously computed points. Thus, two compatibility equations, one for each characteristic, are defined and the value of u and v can be computed. This means that to apply this method a network of points has to be devised.

In Figure 2.2, it is possible to observe how both the position and the velocity of a solution point, called 4, are computed. Starting from points 1 and 2, where the flow velocity is known, two characteristics are drawn, more precisely a C_- is computed starting from 1 and a C_+ starting from 2. The intersection of these two curves is the position of point 4. To find the value of u_4 and v_4, the equation (2.8) can be integrated along the two previously computed characteristics. The problem has now shifted to how the integration process can be done.

Notice that in Figure 2.2 an example of a processing unit is given. This name indicates the blocks upon which the MoC is built. A more precise description of the processing units, along with their operational principles, is presented in Section 2.2.2.

2.2.1. Euler predictor-corrector method

As mentioned earlier, to find both the position and the flow velocity of point 4 a system of four equations with four unknowns needs to be solved. This system, which is made by applying both equations (2.5) and (2.8) for each of the already known points 1 and 2, can be resolved by applying the modified Euler predictor-corrector method. This method is a second-order technique for integrating total differential equations, with the corrector algorithm based on the average property method that, as demonstrated by Hoffman and Zucrow, [23] allows to obtain more accurate results.

A brief explanation of this algorithm can be provided by considering the differential equation:

$$\frac{dy}{dx} = f\left(x, y\right) \tag{2.12}$$

which may be rewritten as:

$$dy = f\left(x, y\right) dx \tag{2.13}$$

Our goal is to numerically integrate the equation (2.13), beginning from a know point (x_i, y_i), to obtain the solution of the unknown point (x_{i+1}, y_{i+1}), considering that $x_{i+1} = x_i + \Delta x$, where Δx is the stepsize of the finite difference algorithm. To do that, firstly a predictor algorithm, or predictor, is applied, allowing the solution to be found as:

$$y_{i+1}^0 = y_i + f(x_i, y_i)\Delta x \text{ (predictor algorithm)} \tag{2.14}$$

By applying only the previously mentioned equation the error varies linearly with Δx.

It is possible to increase the accuracy by employing the previously computed y_{i+1}^0 to compute y_{i+1}^1 by using $y_{i+1/2} = y(x_i + \Delta x/2)$ as substitution for (x_i, y_i) in f(x,y). This implies that the corrected value y_{i+1}^1 can be computed using the so-called corrector algorithm as:

$$y_{i+1}^1 = y_i + f\left(x_i + \frac{\Delta x}{2}, \frac{y_i + y_{i+1}^0}{2}\right)\Delta x \text{ (corrector algorithm)} \tag{2.15}$$

It can be demonstrated that the accumulated error for the corrector is second order concerning the step size. A method to increase the accuracy of the solution involves replacing y_{i+1}^0 with y_{i+1}^1 in equation (2.15) and so repeating the corrector algorithm for a

second time, obtaining the modified Euler predictor-corrector method with iteration:

$$y_{i+1}^{n} = y_i + f\left(x_i + \frac{\Delta x}{2}, \frac{y_i + y_{i+1}^{n-1}}{2}\right)\Delta x \text{ (corrector algorithm with iteration)} \tag{2.16}$$

In general, for an isentropic flow, the permissible maximum step size Δx that guarantees the numerical stability of the method is very large and is rarely a problem. It is also interesting to consider that in many cases the number of iterations needed to find a sufficiently accurate result is generally low and, in some cases, equal to one.

In reality, the method presented in Figure 2.2 is one of the two possible methods, called the direct marching method. In this case, continuous families of left and right characteristics are followed through the flow fields. By using the information from the two previously computed points 1 and 2, it is possible to compute the information for point 4.

A second method, called the inverse marching method, may be used. In this case, the points that have been computed lie along the so-called solution lines, which are usually predetermined. For example, these lines can be equally spaced and perpendicular to the flow, as the line AB in Figure 2.3. The processing unit is obtained in this case by projecting rearward-running characteristics from a point in the solution line to intercept the previous solution line. The properties derived from the intersection are then used to compute the solution point properties.

This last method is rarely used because, despite having a slight advantage in the computation logic, the need to compute point 1 and 2 with iterations cause higher disadvantages, particularly in the efficiency of the code.

2.2.2. Processing units

To resolve the system previously mentioned numerically, the characteristic and the compatibility equations are discretized respectively as [23]:

$$\Delta y_{\pm} = \lambda_{\pm}\Delta x_{\pm} \tag{2.17}$$

$$Q_{\pm}\Delta u_{\pm} + R_{\pm}\Delta v_{\pm} - S_{\pm}\Delta x_{\pm} = 0 \tag{2.18}$$

$$\lambda_{\pm} = \tan\left(\theta \pm \alpha\right) \tag{2.19}$$

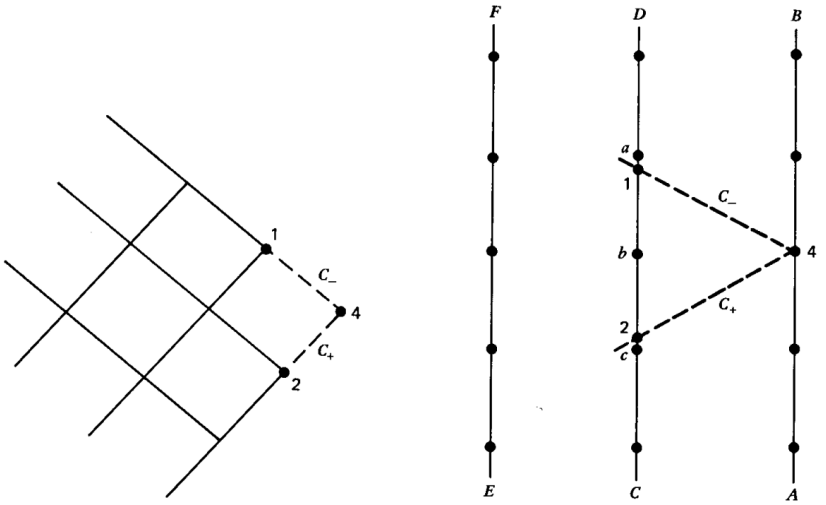

Figure 2.3: Example of direct marching method (left) and indirect marching method (right) [23].

$$Q = u^2 - c^2 \tag{2.20}$$

$$R = 2uv - \left(u^2 - c^2\right)\lambda \tag{2.21}$$

$$S = \delta\frac{c^2 v}{y} \tag{2.22}$$

where + or - denotes C_+ or C_- respectively. Because of the discretization process, the characteristics become straight lines.

Now it is possible to describe the processing units used in the MoC computation. In these units, the Eulerian predictor-corrector algorithm is employed to find the position and speed of the solution point given one or two already known points, depending on the type of unit.

Internal point unit

This unit uses as input the position and velocity components of two already-known points to find a solution point.

By referring to the points names in Figure 2.2, it is possible to rewrite equation (2.17) as:

$$y_4 - \lambda_+ x_4 = y_2 - \lambda_+ x_2 \tag{2.23}$$

$$y_4 - \lambda_- x_4 = y_1 - \lambda_- x_1 \tag{2.24}$$

Where $\lambda_{\pm}$ is computed following the equation (2.19), inside which

$$\theta_{\pm} = \arctan\left(\frac{v_{\pm}}{u_{\pm}}\right) \tag{2.25}$$

and

$$\alpha_{\pm} = \arcsin\left(\frac{1}{M_{\pm}}\right) \tag{2.26}$$

From these last equations is evident that the only thermodynamic information necessary to resolve this problem is the speed of sound, which allows us to compute the value of $M_{\pm}$. This thermodynamic property can be expressed as $c_{\pm} = c\left(V_{\pm}\right)$, where $V_{\pm} = \sqrt{u_{\pm}^2 + v_{\pm}^2}$. Thus $\lambda_{\pm}$ is a function of u and v only. To compute c, an external function is created, as suggested by Hoffman and Zucrow [19], allowing the decoupling between the processing unit and the gas model utilized.

Now this possible to rewrite equation (2.18) as

$$Q_{+}u_4 + R_{+}v_4 = T_{+} \tag{2.27}$$

$$Q_{-}u_4 + R_{-}v_4 = T_{-} \tag{2.28}$$

where

$$T_{+} = S_{+}\left(x_4 - x_2\right) + Q_{+}u_2 + R_{+}v_2 \tag{2.29}$$

$$T_{-} = S_{-}\left(x_4 - x_1\right) + Q_{-}u_1 + R_{-}v_1 \tag{2.30}$$

obtaining a system of two equations with two unknowns that can be solved.

The Eulerian predictor-corrector method is used to solve this system by updating the coefficients of the equations (2.27) and (2.28) at every iteration, using the following equations:

$$Q_{+} = u_{+}^2 - c_{+}^2 \tag{2.31}$$

$$R_{+} = 2u_{+}v_{+} - Q_{+}\lambda_{+} \tag{2.32}$$

$$S_{+} = \delta\frac{c_{+}^2 v_{+}}{y_{+}} \tag{2.33}$$

$$Q_- = u_-^2 - c_-^2 \tag{2.34}$$

$$R_- = 2u_-v_- - Q_-\lambda_- \tag{2.35}$$

$$S_- = \delta\frac{c_-^2 v_-}{y_-} \tag{2.36}$$

At the first iteration, so in the Euler predictor algorithm, the values of $u_\pm, v_\pm$ and $y_\pm$ are defined as:

$$u_+ = u_2 \qquad v_+ = v_2 \qquad y_+ = y_2 \tag{2.37}$$

$$u_- = u_1 \qquad v_- = v_1 \qquad y_- = y_1 \tag{2.38}$$

The values of x_4^0, y_4^0, u_4^0 and v_4^0 can be computed by substituting the values obtained from equations (2.37) and (2.38) in the previously mentioned ones.

After this initialization, the Euler corrector algorithm is employed and so the values of $u_\pm, v_\pm$ and $y_\pm$ are defined as:

$$u_+ = \frac{u_2 + u_4}{2} \qquad v_+ = \frac{v_2 + v_4}{2} \qquad y_+ = \frac{y_2 + y_4}{2} \tag{2.39}$$

$$u_- = \frac{u_1 + u_4}{2} \qquad v_- = \frac{v_1 + v_4}{2} \qquad y_- = \frac{y_1 + y_4}{2} \tag{2.40}$$

Thus the values of x_4^1, y_4^1, u_4^1 and v_4^1 can be computed.

Now the corrector algorithm with iteration is applied to improve the accuracy of the solution. This is done by substituting x_4, y_4, u_4 and v_4 in equations (2.39) and (2.40) with the results of the previous iteration of the corrector algorithm. For example at the second iteration the results of the previous one, x_4^1, y_4^1, u_4^1 and v_4^1, are substituted into equations (2.39) and (2.40), which results are used in equations (2.23), (2.24) and from (2.27) to (2.36) to find the values of x_4^2, y_4^2, u_4^2 and v_4^2.

The corrector algorithm is iterated until the convergence condition, which has been defined in the implemented code as the relative tolerance $\frac{|P^n - P^{n-1}|}{|P^n|} \leq$ (specified tolerance), is met. The value of the specified tolerance is set equal to 10^{-6}. This check is made usually on two variables, which can be x_4 and y_4 or u_4 and v_4. Additionally, there is also a check on the maximum number of iterations after which the convergence condition is reached,

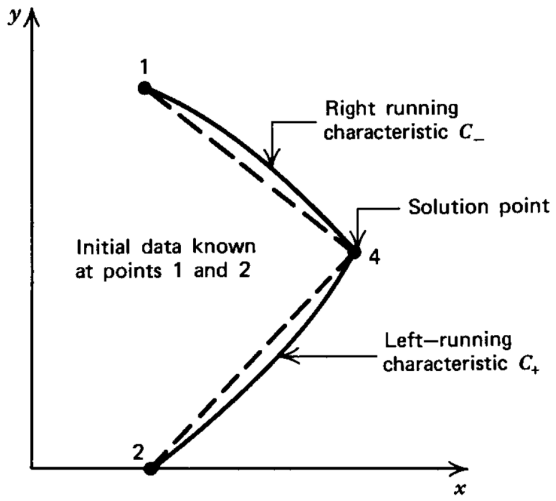

Figure 2.4: Example of the application of an internal point unit with an initial point on the axis of symmetry [19].

but usually, the iterations necessary are quite limited. The convergence speed is a function of the gradients in the flow field: if they are low, very few iterations are necessary to reach convergence, while, in the case of large gradients a high number of iterations is necessary and, in the worst case, the desired tolerance may not be reached.

In Figure 2.4 it is possible to notice a case that can happen when point 2 is along the symmetric axis (planar case) or the axis of rotation (axisymmetric case). In both cases, $y_2 = 0$ and thus v_2/y_2 is substituted by v_1/y_1 for the predictor. In the corrector, where S_+ is based on the average values of y_+ and v_+ this is no more a concern.

Another problematic case may appear when $\lambda_- = \infty$ or $\lambda_+ = \infty$. To resolve that, x_4 is put equal to x_1 or x_2 respectively, and y_4 is computed with equation (2.24) or equation (2.23). This can happen only if:

$$\theta - \alpha = 90° \qquad \text{or} \qquad \theta + \alpha = 90° \tag{2.41}$$

A way to detect and resolve this eventuality is not implemented because, for the value of M and θ presented in the studied cases, none of the two equations (2.41) are true.

It is worth noting that all the processing units presented later in this section and in Section 3.1.2 are variations of the internal point unit.

Direct upper wall point unit

This unit can be viewed as a special case of the previously explained internal point unit, and it is applied when the flow is bounded by a prescribed physical wall, such as the wall of a nozzle.

In this section, only the case where the flow is below the wall, as in Figure 2.5, is treated. In the same figure is also possible to notice the main difference with the interior point unit: only one point, called 2, is used as a starting point for the computation because point 1 is external to the flow field. This means that only the equations referred to C_+, the only characteristic present, are used. In substitution to the ones referred to C_- the functions that describe the prescribed wall and its slope are employed:

$$y = y(x) \tag{2.42}$$

$$\frac{dy}{dx} = \tan(\theta) = \frac{v}{u} \tag{2.43}$$

The first equation derives from the definition of the direct wall point. The second describes a well-known property of a flow near a wall: the velocity of it must be tangent to the wall. The presence of a speed different from zero in the correspondence of a fixed wall is explained by the hypothesis of isentropic, and therefore inviscid case, made initially.

If we focus on the algorithm point of view, the equations (2.42) and (2.43) are solved simultaneously with equations (2.23) and (2.27) using the previously mentioned Eulerian predictor-corrector algorithm to obtain x_4, y_4, u_4 and v_4 as results.

For this processing unit an external function that computes the intersection between C_+ and the wall, together with the local first derivative, has to be implemented. In this way is possible to decouple the type of wall (circular arc, parabola, cubic) from the processing unit.

While this does not occur in the cases under consideration, it is possible that $\lambda_+ = \infty$. Therefore, it may be necessary to identify this possibility and enforce $x_4 = x_2$.

Axis point unit

This type of processing unit is used when the solution point 4 is located on the axis of symmetry, as shown in Figure 2.6.

Because the flow field is present both above and below the axis of symmetry, the previously

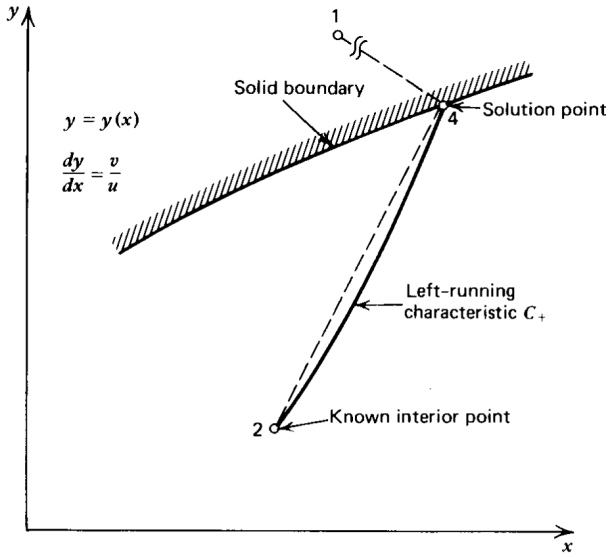

Figure 2.5: Example of application of the direct upper wall point unit [19].

mentioned internal point unit may be employed. However, with more detailed observation, is possible to notice that, by definition, $y_4 = v_4 = \theta_4 = 0$ and so this case may be treated as a special case of the direct wall unit, where the axis of symmetry is treated as a sort of wall that forces the flow to follow a prescribed direction and the solution point to be along it. This approach allows for a decrease in the computational cost.

Due to how the divergent nozzle is constructed, the input for this process is point 1, which is connected to solution point 4 through a C_-. Therefore the system is composed of equations (2.24) and (2.28), together with the condition $y_4 = v_4 = 0$, reducing the number of unknowns from four to two. These unknowns are u_4 and x_4.

In contrast with the previously described processing units, the presence of a characteristic with infinite slope does not occur, because $\lambda_- = \tan(\theta - \alpha) = \tan(-\alpha) = \frac{-1}{\sqrt{M^2-1}}$, thus the slope cannot be infinite because M>1.

2.3. Application of the MoC for the design of a planar symmetric divergent nozzle

Before explaining how the processing units may be employed to design a divergent nozzle, it is important to define which types of nozzle can be designed and their properties.

The first main classification can be made based on the shape of the passage area, dividing the nozzle into a planar or axisymmetric type. In the first case, the passage area is rectangular with fixed thickness and an area distribution defined by the MoC along the

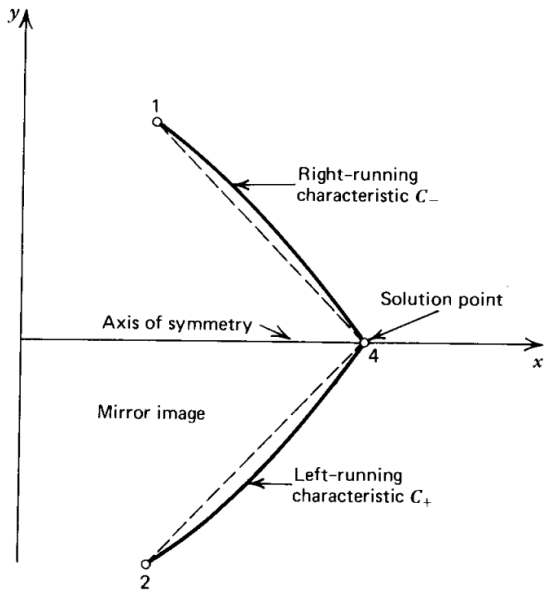

Figure 2.6: Example of application of the axis point unit [19].

nozzle axis of symmetry. In the second one, the passage area is a circle and so the designed profile will be rotated along its axis of symmetry to obtain the three-dimensional nozzle.

A second classification can be made based on the application type and the desired properties of the flow at the nozzle outlet. The first type of nozzle, known as a nozzle for maximum thrust, is employed in applications where the primary objective is to achieve a target expansion, typically expressed as a Mach number, with the minimum possible length and weight. The main drawback is the presence of a strongly nonuniform flow at the outlet. An illustrative application is a rocket nozzle, where weight and length are crucial, and the nonuniformity of the flow is not a significant concern [19].

The second type is the so-called supersonic wind tunnel nozzle design. In contrast to the nozzle for maximum thrust, the primary objective of this type of nozzle is to achieve the desired expansion with an outlet flow as uniform as possible, accepting a greater length and weight. An example of an application could be, as the name suggests, a wind tunnel nozzle, where the additional length and weight are not a concern.

Focusing on a convergent-divergent stator turbine, the length affects the viscous losses, making it desirable to limit. However, because a uniform outlet flow is preferable for the performance of the next cascade and weight is not a concern, a wind tunnel nozzle type is the best choice. About the other classification, a planar nozzle is the only viable option, as a passage area with a rectangular shape is the only suitable choice for constructing a blade passage.

In reality, examples of nozzles for maximum trust, have been developed, as shown in [25], demonstrating that a uniform flow at the outlet is possible to obtain also with this type of nozzle.

To start the design of a nozzle of the previously defined type, the main necessary inputs are:

- fluid definition;
- total quantities at the inlet, such as total pressure and temperature;
- a thermodynamic quantity that describes the expansion ratio inside the nozzle, usually one between the outlet Mach number or the outlet static pressure;
- throat height, that may be computed as a function of the mass flow;
- the evolution of a quantity in the kernel region has to be fixed. A possible choice may be the evolution of the pressure with respect to the total one [13] or a function that describes the kernel region wall [19].

As explained before, to apply the MoC a network, or grid, of points has to be built. This grid can be divided into four main regions: [19, 22, 26]: following the flow direction is possible to identify the initial-value line, the expansion of the initial-value line, the kernel region, and the reflex region. The results of the previous zone are used to initialize the subsequent one. The final results include the nozzle profile and the thermodynamic quantities of every computed point An example of the network with its division may be observed in Figure 2.7.

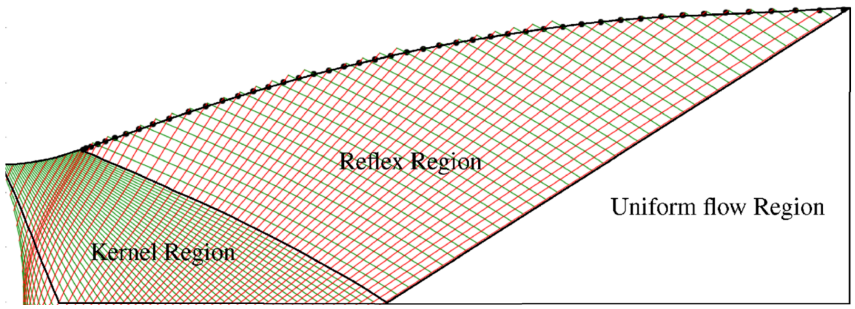

Figure 2.7: Example of the grid used to compute a planar, symmetric, supersonic nozzle. The red lines are C_+, the green ones the C_- [26].

2.3.1. Initial-value line definition

As explained earlier, the MoC works only if the flow is supersonic. So, to initialize it, a reliable numerical method has to be employed. It is important to consider that the

initialization phase has an important influence on the MoC results. This is because, as explained by Hoffman and Zucrow [19], a very well-written MoC algorithm may give completely wrong results if the initialization is done by using the wrong procedure.

This region has two other important consequences: firstly, the number of points used to discretize the initial line is the main and only method to control the number of solution points computed by the method, and so the accuracy and the computational cost of it. Secondly, if not directly given, the throat height is computed iteratively so that the mass flow passing through the throat is equal to the objective one. The iterative procedure is necessary because the mass flow is a function of the velocity and of the density of the flow, that are computed during the initialization process.

Because of what was said before, a mathematical description of the transonic flow in a nozzle throat is necessary. This description can be done by resolving the perturbation equation (2.44) [19].

$$\left(1 - M_\infty^2\right) \frac{\partial u}{\partial x} + \frac{\partial v}{\partial y} + \delta \frac{v}{y} = M_\infty^2 \left(\gamma + 1\right) \left(\frac{u}{U_\infty}\right) \frac{\partial u}{\partial x} \tag{2.44}$$

This equation describes the transonic flow under the hypothesis of two-dimensional, planar, or axisymmetric irrotational flow with perfect and ideal gas.

Initialization of the MoC using the Sauer method

Between the various solutions developed in the past years, in this work the method developed by Sauer in 1947 [27] and resumed by Hoffman and Zucrow [19] is used.

Under the hypothesis of one-dimensional and sonic flow, the undisturbed free-stream velocity U_∞ is equal to the critical speed of sound c^*, which may be described as a function of the total quantities at the inlet and the fluid, thus $M_\infty = 1$. Therefore equation (2.44) can be reduced as

$$\left(\gamma + 1\right) \left(\frac{u}{c^*}\right) \frac{\partial u}{\partial x} - \frac{\partial v}{\partial y} - \delta \frac{v}{y} = 0 \tag{2.45}$$

Because the flow is irrotational, it is possible to define the nondimensional perturbation velocity potential as:

$$\Phi = U_\infty x + \phi = c^* (x + \phi') \tag{2.46}$$

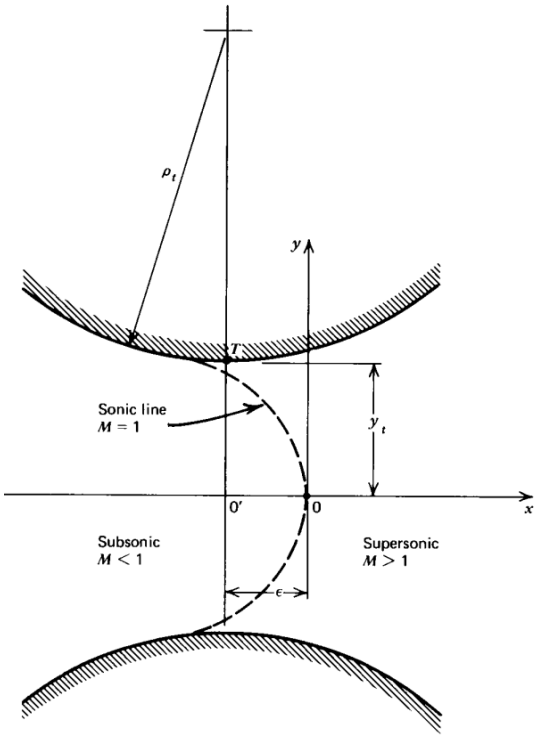

(a)

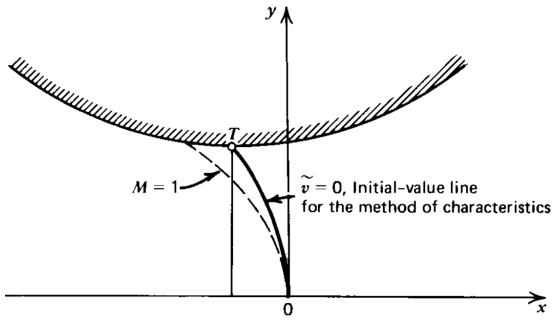

(b)

Figure 2.8: (a) Nozzle throat geometry and coordinate system for the transonic flow analysis made using Sauer [19]. (b) Initial-value line vs sonic line [19].

Thus the perturbation velocity field is defined as:

$$\tilde{u}(x,y) = c^* + u = c^*(1+u') = \Phi_x = c^*(1+\phi'_x) \tag{2.47}$$

$$\tilde{v}(x,y) = v = c^* v' = \Phi_y = c^* \phi'_y \tag{2.48}$$

where the nondimensional perturbation velocities are equal to:

$$u' = \frac{u}{c^*} \quad \text{and} \quad v' = \frac{v}{c^*} \tag{2.49}$$

As demonstrated in [19], by substituting equations (2.47) and (2.48) in equation (2.45) a nonlinear partial differential equation is obtained. This equation may be resolved approximately by assuming a power series solution, with coefficients selected so that the boundary conditions are satisfied.

Thus, it is possible to describe the velocity field in the neighborhood of the throat as

follows:

$$\tilde{u}(x,y) = c^*(1+u') = c^*\left(1+\alpha x + \frac{(\gamma+1)\alpha^2 y^2}{2(\delta+1)}\right) \tag{2.50}$$

$$\tilde{v}(x,y) = c^* v' = c^*\left(\frac{(\gamma+1)\alpha^2 xy}{1+\delta} + \frac{(\gamma+1)^2\alpha^3 y^3}{2(1+\delta)(3+\delta)}\right) \tag{2.51}$$

where α is a variable function of the wall slope near the throat and so of the selected wall function, In this work, the wall is selected as a circular arc of curvature ρ_t. This type of wall is a classical choice, as shown in [13, 19, 26], because it allows for a slope equal to zero at the throat, it is relatively simple to implement in a code, and it guarantees a controlled slope that avoids flow detachment. It is always possible to select a different wall shape and so compute a new equation of α.

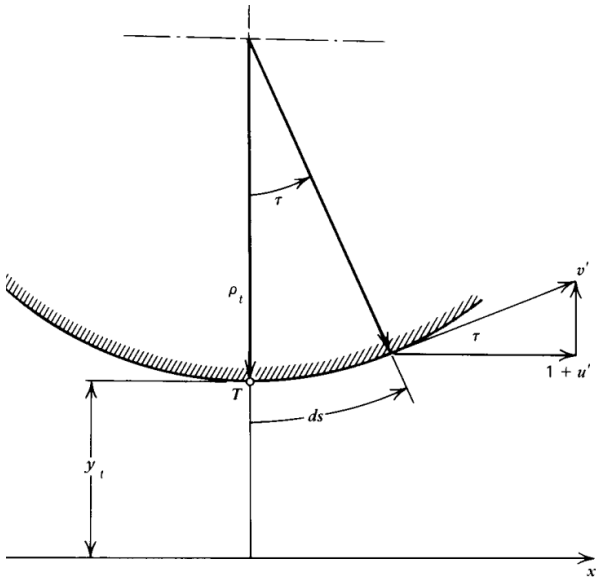

Figure 2.9: Model used to compute the value of α in case of wall made as a circular arc [19].

A way to compute α is to consider it as a means to apply a boundary condition to equations (2.50) and (2.51) and thus to indicate the shape of the wall contour. To do that, a linearized boundary condition applicable to an internal flow must be developed.

From Figure 2.9, is possible to observe that:

$$\tan(\tau) = \frac{v'}{1+u'} \cong v' \tag{2.52}$$

At the throat, knowing that the curvature k is the reciprocal of the radius of curvature

ρ_t, it is possible to write:

$$k = \frac{1}{\rho_t} = \left[\frac{d\left(\tan(\tau)\right)}{ds}\right]_T = \left(\frac{dv'}{ds}\right)_T \tag{2.53}$$

where

$$\frac{dv'}{ds} = \frac{\partial v'}{\partial x}\left(\frac{dx}{ds}\right) + \frac{\partial v'}{\partial y}\left(\frac{dy}{ds}\right) = \frac{\partial v'}{\partial x} \tag{2.54}$$

The last equality of equation (2.54) is true under the hypothesis of $\rho_t \gg y_t$, and thus $(dx/ds) \cong 1$ and $(dy/ds) \cong 0$.

By substituting the results of equation (2.54) into equation (2.53) yields:

$$\rho_t = \frac{1}{\left[\frac{\partial v'}{\partial x}(x,y)\right]_T} \tag{2.55}$$

and by deriving equation (2.51) with respect to x:

$$\frac{\partial v'}{\partial x} = \frac{(\gamma+1)\alpha^2 y}{1+\delta} \tag{2.56}$$

From this last equation the value of $\frac{\partial v'}{\partial x}$ can be computed at the throat and, by substituting equation (2.56) into equation (2.54) is possible to obtain the value of the radius of curvature as:

$$\rho_t = \frac{1+\delta}{(\gamma+1)\alpha^2 y_t} \tag{2.57}$$

Up to this point, it is assumed that u'(x,0) is known and the radius of curvature is computed so that the correct value of u'(x,0) is obtained.

But, if we invert the interpretation, and so we want to compute the value of u'(x,0) by using the geometrical properties of the nozzle throat, the value of α can be computed as:

$$\alpha = \left[\frac{1+\delta}{(\gamma+1)\rho_t y_t}\right]^{1/2} \tag{2.58}$$

In the case of different wall functions, a new expression of α can be computed so that the value of u'(x,0) is determined based on the geometry of the throat.

An observation can be made: the radius of curvature considered for the computation of α is that of the converging wall, which may differ from the diverging one, allowing a potential degree of freedom in nozzle design.

The equations (2.50) and (2.51) enable us to characterize the flow in the vicinity of the throat. Using these equations, we can compute various equations that describe the locus of points, each defined by a different property in common.

An example is the so-called sonic curve, or sonic line, where M=1 and $(\tilde{u}^2 + \tilde{v}^2) = c^{*2}$. To satisfy these conditions, we need to enforce $\tilde{u} = c^*(1 + u') = c^*$. This is done by matching equation (2.50) with c^*, obtaining the equation (2.59).

$$x = -\frac{(\gamma + 1)\alpha y^2}{2(1 + \delta)} \tag{2.59}$$

The sonic line is a parabola where, under the hypothesis of the symmetric nozzle, y varies from the axis of symmetry to the upper wall of the nozzle, or, using algebraic expressions, between $y = 0$ and $y = Y_t$, where Y_t is half of the total throat height.

By studying the shape of the sonic line as a function of the radius of curvature of the converging wall, it is possible to demonstrate that the line tends to be straight for a high radius because the flow in the throat tends to become one-dimensional. It is important to point out that, for highly distorted flow, the method presented here is no more reliable. For this reason, a lower limit on the radius is present, equal to $\frac{\rho_t}{Y_t} = 2$.

To initialize the flow of the MoC, the sonic line cannot be used, for two theoretical reasons. It is possible to notice, from Figure 2.8b, that the Mach lines departing from the sonic line intersect the wall upstream from the throat point T. But, because this point is used as a boundary condition in the evaluation of equation (2.57), the region upstream T is within the range of influence of T, and the MoC cannot be initialized by an initial-value line that is in the range of influence of a downstream point. The second reason is related to the value of M. If its value is equal to one, the two characteristics become coincident, making the method inapplicable. It is worth noting that if M is very close to one, a Mach number lower than one can appear due to a numerical error in the algorithm, causing the failure of the method.

A possible initial line, that has been used in this work, is the one where $\tilde{v} = 0$, which equation is:

$$x = -\frac{(\gamma + 1)\alpha y^2}{2(3 + \delta)} \tag{2.60}$$

This new curve is a parabola like the sonic line, that intersects the latter on the axis of symmetry, where, for definition, $\tilde{v} = 0$, and where the system of reference is centered. The curve $\tilde{v} = 0$ intersects the wall in T, satisfying the solid wall boundary condition exactly.

The point of this curve that intercepts the wall is fundamental because it is where the circumference arc that forms the wall is centered along the horizontal direction at a distance:

$$\epsilon = -\frac{(\gamma + 1)\alpha Y_t^2}{2(3 + \delta)} \tag{2.61}$$

upstream from the center of the reference system.

The selection of the initial line allows the maintenance of a flow with $M \geq 1$ consistently close to the sonic line, ensuring accurate results. However, this definition of the initial-value line is not the only option available. Another definition is, for example, a straight vertical line positioned at the intersection of the sonic line with the axis of symmetry [22].

For both of these two proposed initial-value lines, a detrimental effect on their accuracy is observed if a low curvature radius is present. This is because as the radius decreases, the sonic line tends to curve more, leading to an increased relative distance from an initial-value line. This increase in distance causes a rise in the flow field velocity along the initial-value lines, casting doubt on the assumption of small perturbation. It is worth noting that the locus of points where $\tilde{v} = 0$ also tends to become a straight line with increasing radius of curvature.

It is also important to point out that the system of reference used for Sauer is also maintained for the rest of the MoC computation. This last choice is not always necessary but the reference system for the initial-value line must be the same as the one explained in the paper to maintain the validity of the model.

Other methods to resolve the perturbation equation in the throat

A possible question that may arise is if the Sauer method is the best possible choice to describe the flow in the vicinity of the throat or if there are other possibilities.

The proposed model, which has the main advantage of being straightforward and widely used, has been proven to work with enough reliability only if $\rho_t/y_t > 2$ because, for a lower radius of curvature, the hypothesis of one-dimensional flow starts to be no more valid, making the accuracy of the model questionable. For $\rho_t/y_t < 1$ the small perturbation

model breaks down completely for the same reason [19].

To overcome this limit, some methods that allow reasonable results for $\rho_t/y_t < 2$ have been developed in the past years.

An example is the Hall method [28], which employs a power series expansion for the velocity components in inverse powers of the expansion parameter $R = \rho_t/y_t$. The first approximation, obtained from the coefficient 1/R, gives the same results as the Sauer method. Hall's model is obtained through a third approximation, with a coefficient equal to $1/R^3$. Notice that this method works only if R>1 and is in agreement with experimental data obtained by Back et al. [29, 30], near R=2, but not for smaller R.

Kliegel [31] has modified the Hall method by substituting the expression of R in the equations with (R+1), allowing to have a convergent method also for R<1. The results are in agreement with the experimental data also for $\rho_t/y_t < 1$, except for the area near the wall, as demonstrated by Hoffman and Zucrow [19].

From this last analysis, is possible to conclude that all three methods give the same results for high values of ρ_t/y_t, but for small values, the Kliegel method appears to be the most accurate.

However, because it has been supposed that the radii of curvature considered in this dissertation are always $\rho_t/y_t > 2$, the use of the Sauer method is considered acceptable.

2.3.2. Initial-value line expansion

After defining the points along the selected initial line, a network of points has to be built. To do that is important to remember that the points along the initial line, even if they share a common property, such as a vertical flow field velocity equal to zero, are not connected by a characteristic line. For this reason, the initial line must be expanded by computing the C_+ and the C_- characteristics departing from every point, with the exclusion of the points located on the symmetrical axis and right below the wall, where only the left-running and right-running characteristics are respectively computed. To compute the solution points two processing units are employed in this phase: the internal and axis point ones.

Usually, an algorithm for defining this region starts by computing the C_+ passing through the point on the intersection between the axis of symmetry and the initial line (point D in Figure 2.10a), and the C_- that passes through the point above D, called E. Using the internal point processing unit, the intersection point is computed, called 1 (see Figure 2.10b). Then from this point, a C_- that intersects the axis of symmetry is drawn, and

the intersection point, called 4, is computed using the axis point unit. The same process is repeated, but starting from a new point above E along the initial-value line. From E this time a C_+ is drawn.

The final goal is to obtain a C_- that links the intersection between the initial line and the upper wall, point B in Figure 2.10a, with the axis of symmetry.

In this phase point D is the most critical one, because, for definition, the flow is only horizontal and $M = 1$. This implies that two problems may arise: firstly, because $\theta = 0$ and $M = 1$, $\lambda_+ = \infty$ may be true, and so x_1 is forced equal to x_D. The second is that, as explained before, M_D may be slightly below one due to a possible numerical error causing the method to fail. Interestingly, in all the cases analyzed in this work, a value of λ_+ equal to ∞ has never been observed, unlike the presence of $M < 1$ in the intersection point.

To resolve the latter, a variation of the predictor-corrector method has been devised and implemented: when $M < 1$ is detected in point D, the predictor algorithm is modified, by using point E and the point above E along the initial-value line instead of E and D. These last points are then employed in the corrector algorithm with iteration.

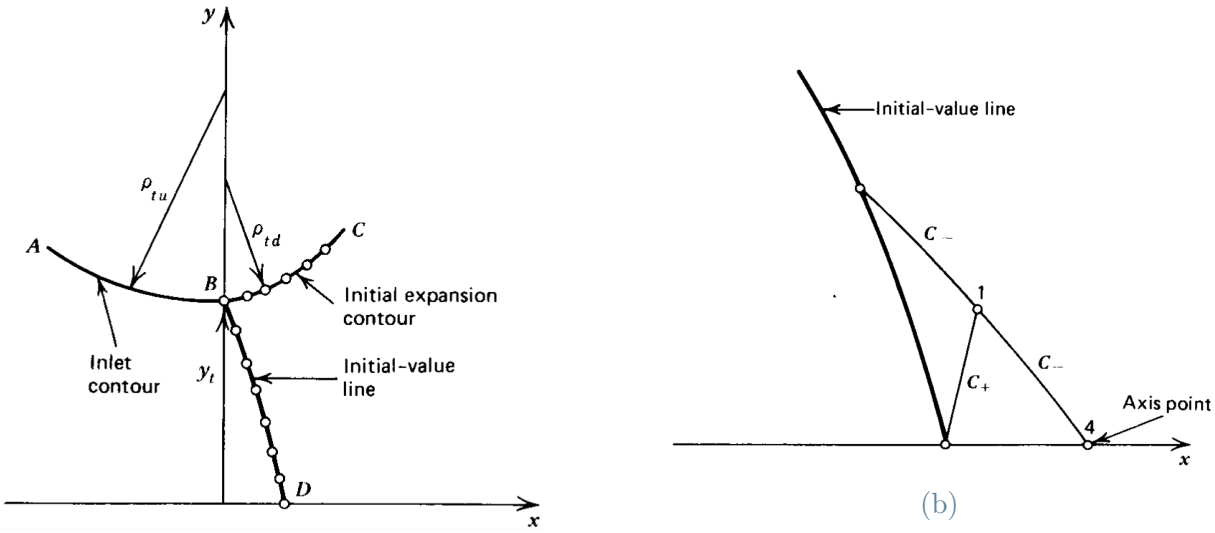

Figure 2.10: (a) initial line positioned in the nozzle, notice the different curvature radius between convergent and divergent part [19]. (b) How the first computation process of the initial line expansion is made [19].

2.3.3. Kernel region

In this region of the network, the flow field between the prescribed upper wall and the axis is expanded up to the design Mach number M_D on the axis of symmetry.

Firstly, a C_+ is drawn starting from the point right below the one called B in Figure 2.10a, as in Figure 2.11a where the point is called 2. The C_- that starts from B and connects the upper wall with the axis of symmetry can be called old C_-. The previously mentioned C_+ intersects the upper wall in 4, whose position and speed are computed using the direct upper wall point unit. After that, using the internal point unit, a solution point is found as the intersection between the C_- draw from 4 and the C_+ starting from the point below 2 along the old C_-. Then, the internal point unit is applied another time using the point computed right before and the next point in the old C_-. In this way, a new C_-, that links point 4 with the axis of symmetry is constructed. The point that intersects the axis of symmetry is computed using the axial point unit.

Now the new C_- becomes the old one and a new C_- is computed starting from a point in the upper wall defined in the same way as point 4.

This procedure creates a series of C_- as in Figure 2.11b and continues until the Mach on a new C_- is equal or greater to M_D in its intersection with the axis of symmetry. Notice that in the example given by Hoffman and Zucrow, this happens between two C_- and so the point K, that is the last kernel point along the axis of symmetry, is positioned exactly. In the code developed this is not done, but the algorithm ends when the Mach number of the intersection between the computed C_- and the axis of symmetry is higher or equal to Md. This is because it is possible to reach a value close to M_D with a limited number of initial points.

It is also essential to note, as explained earlier, that the kernel wall is prescribed as input. This can be viewed as an advantage because it allows us to adapt the geometry to a potential constraint in the footprint. As easy to demonstrate, the higher the radius of curvature, the longer the nozzle becomes.

2.3.4. Reflex region

The main goal of this region is to draw the final part of the nozzle in a way that guarantees a parallel and uniform outlet flow using as input the last C_- of the kernel region and the nozzle mass flow.

Firstly, the endpoint of the nozzle is computed by drawing the last C_+ of the nozzle, which

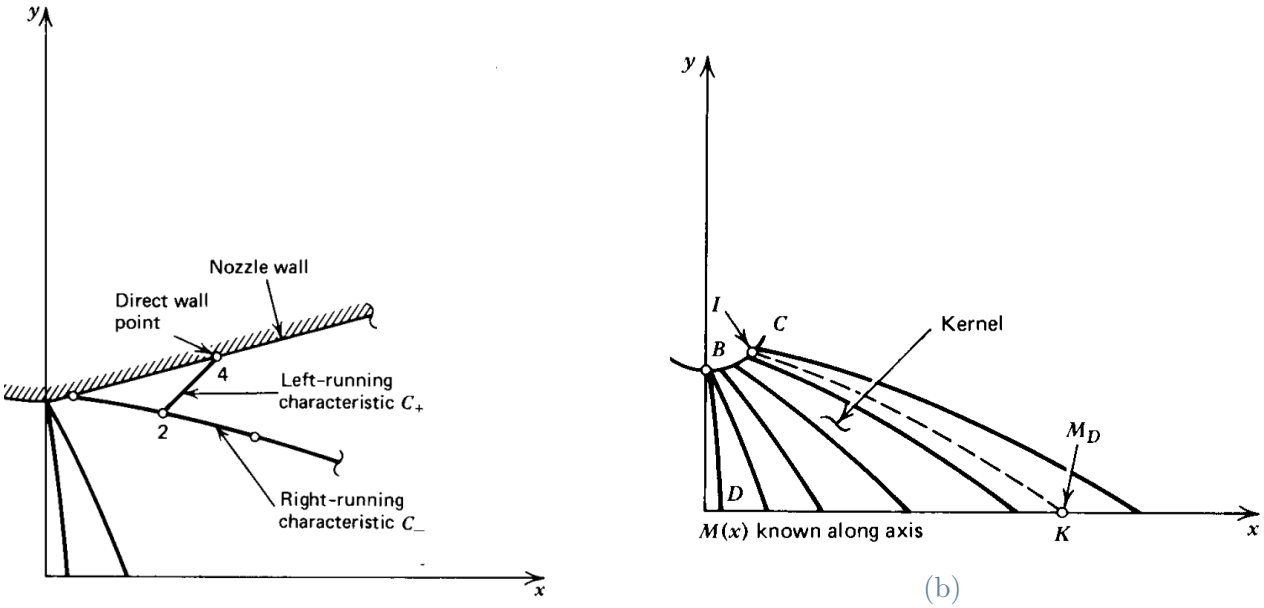

Figure 2.11: (a) Application of the direct wall in the kernel region [19]. (b) C_- that connects the upper wall with the axis of symmetry in the kernel region [19].

links the last point of the kernel region, K in Figure 2.12, with the last point of the upper wall, called F in the same figure. This curve is a straight line with constant properties. Point K, the starting point of this characteristic, belongs to the axis of symmetry, where $v = 0$ for definition. Thus the angle that this last C_+ forms with the positive horizontal direction is equal to the Mach angle $\arcsin\left(\frac{1}{M_d}\right)$, where M_d is the design Mach number at the outlet. The endpoint of the nozzle is positioned at a distance along the C_+ so that the balance of mass is verified.

The problem is now how to define the wall that connects I with F, called the turning contour, and, to do that, how to define the properties of the flow field in the domain between the lines IK, KF, and the turning contour. This problem is an initial-value problem with data specified on two characteristics of opposite families.

The most general algorithm is the following: because all the points along the line KF have the same properties, is possible to divide the line into a series of evenly spaced points. From every of these points, a C_- is drawn by intersecting it with the C_+ departing from the previously computed points along IK. The idea is to start from the point next to K in the KF line to draw the first C_-. The length of these characteristics increases by adding more points obtained as the intersection between the C_- considered and the C_+ that start from the points along KI until the balance of mass is satisfied. The last computed point is the one that defines the turning contour. When this point is found, a new C_-, that

starts from the next point along the KF line is drawn.

In the case of the planar nozzle, a simpler method, that exploits the presence of a simple wave flow region to decrease the computational cost of the algorithm may be implemented. A simple wave flow is a special type of flow that happens when the governing partial differential equation is homogeneous and the coefficients are a function of the dependent variables only. In the case of steady, supersonic two-dimensional irrotational flow, this guarantees the presence of a series of properties, demonstrated in [23], that may be exploited.

These properties are: the two velocity components, u and v, are dependent and so the characteristics of one family are straight lines having constant properties. The presence of this type of flow in the reflex region is guaranteed by the third property. If a nonuniform flow region adjoints a uniform flow region, then the nonuniform region must be a simple wave flow region. Thanks to that, the reflex region of a planar nozzle is always a simple wave region, in contrast with an axisymmetrical nozzle.

More precisely, the characteristics along which the properties are constant, are the C^+ that start from the points along KI. As before, their length is computed so that the balance of mass is respected.

Although the algorithm that exploits the presence of a simple wave region can be employed, in the implemented code the first option is used. Using the simple wave approach, the number and position of the points defining the turning contour are strongly linked to the number of points used to define the initial line. Consequently, there may be zones where their concentration is too low, such as the interface between the kernel and reflex regions or near the end of the nozzle, increasing the risk of an incorrectly defined turning contour. This latter issue is not present in the implemented algorithm, where the points defining the turning contour are nearly evenly spaced. Additionally, the number of these points is independent of the one used to define the initial line, allowing for better discretization. The implemented algorithm also facilitates an easier implementation of the axisymmetric case if needed.

Independently by the solution adopted, is fundamental to have a C^2 nozzle wall, a property that avoids the presence of shocks. To achieve this, a bisection algorithm is implemented: using the interior point unit two endpoints of the studied C_- are identified, one that allows a higher mass flow and one that allows a lower mass flow with respect to the goal. The endpoint is then computed with a bisection algorithm between these two points. This choice has been necessary after some tests, where, even with a very high number of points along the initial line and KF, the turning profile was not enough regular to guarantee the

absence of shocks.

A last critical issue may be found in the zone where the turning contour computed in the reflex region is connected with the prescribed wall of the kernel region. In fact, by checking the mass flow, a difference between the mass flow passing through the throat and along the line IK is present. This error, which is always under 1% and negative, meaning that the mass flow passing through the throat is higher than the one passing through IK, is enough to create a small discontinuity in the first derivative when the two profiles are connected. This problem has been mitigated by using as the mass flow goal of the reflex region the one computed along IK. As demonstrated by the verifications done using CFD, this choice has not caused any problem in the design of the nozzle.

The presence of this error in the mass flow may be explained by two main causes: the first is the presence of a numerical error, and the second is related to the non-even distribution of the characteristics, which may cause the presence of regions where the fluid properties are not computed accurately.

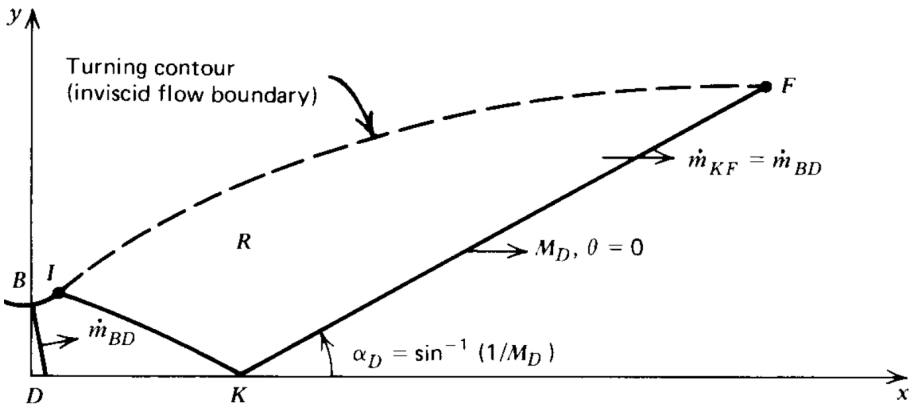

Figure 2.12: Computation of the last C_+ at the outlet of the reflex region [19].

2.3.5. Design of the convergent part of a supersonic nozzle

To simulate the designed nozzle, a convergent part is needed. This part has been designed as a circular arc with a radius of curvature equal to the one used in the initial-value line definition. Its center is positioned horizontally at a distance ϵ before the center of the reference system. The vertical coordinate is computed such that its ending point is positioned at a distance equal to the semi-throat height from the horizontal axis, coinciding with the throat.

A straight section is then added upstream to the convergent arc of the circumference, allowing the flow to be initialized as solely horizontal. The boundary is positioned at a

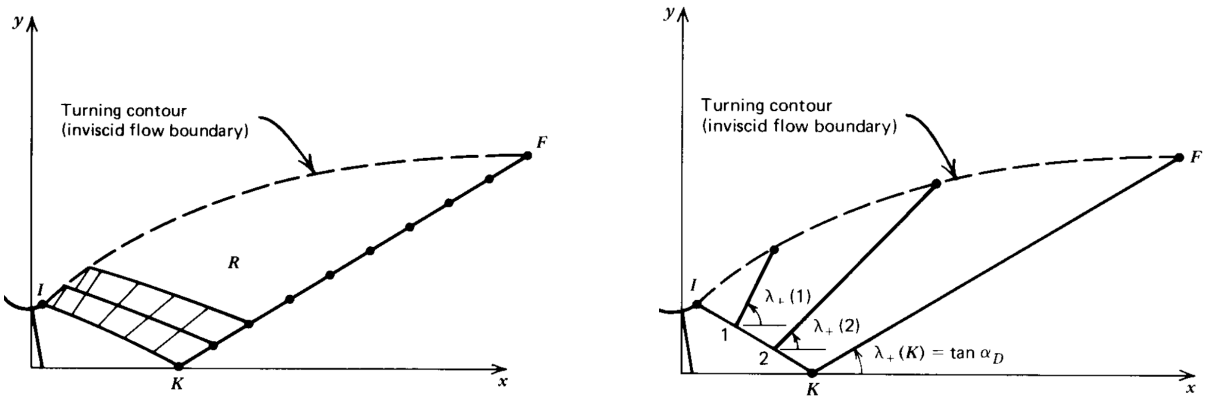

Figure 2.13: (a) Example of how the reflex region is computed in a standard way [19], (b) example of how the reflex region is computed exploiting the simple wave properties [19].

sufficient distance from the convergent part to ensure they do not affect each other.

The height of the inlet is equal to the one necessary to obtain the desired M, which is lower than one.

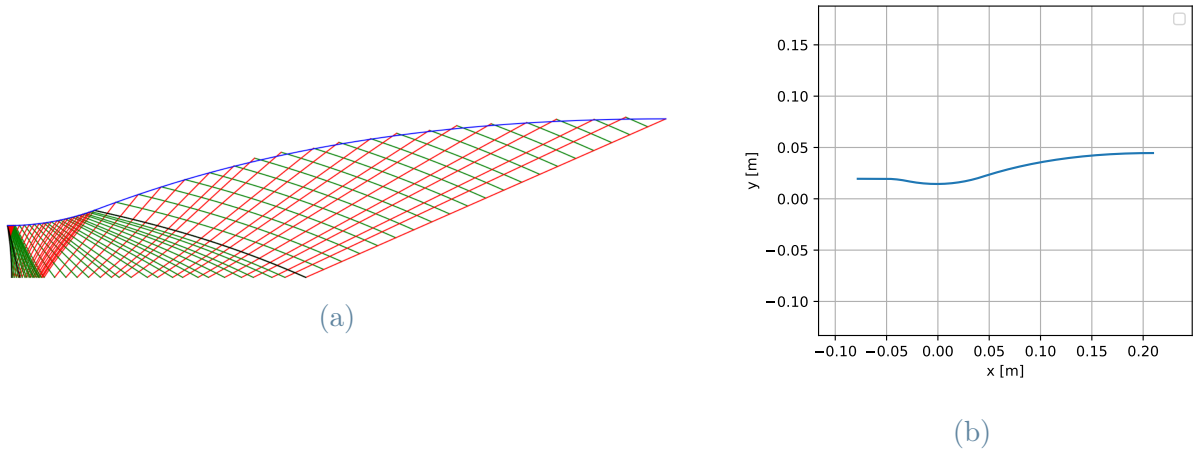

Figure 2.14: (a) Example of characteristics network for ideal CO2, $M_{in} = 0.5$,M_d=2.5. (b) Example of nozzle profile with the same input of the network of the characteristics.

2.4. Planar symmetric MoC verification for perfect gas

Before starting this phase, it is necessary to explain how a thermodynamic model, in this case a perfect gas one, has been implemented in the MoC. By recalling what has been said previously, the only thermodynamic information used by the method is the speed of sound

c, which allows us to compute the Mach number and so the slope of the characteristics.

In the case of a perfect flow, the expanding fluid is identified by its molecular weight and its heat capacity ratio γ. The heat capacity at constant pressure, necessary for the computation, is computed as $C_p = \frac{R_g \gamma}{\gamma - 1}$ where R_g is the specific gas constant of the expanding fluid.

All the thermodynamic quantities, so not only the speed of sound but also, for example, pressure and temperature, are functions of the velocity field inside the nozzle only, because the total quantities, P_t and T_t, are constant due to the hypothesis of homentropic flow made initially.

2.4.1. CFD models and approximations

From now on all the codes implemented will be verified through two-dimensional CFD simulations in case of nozzle and with quasi-three-dimensional simulation for blades. To do that, the commercial program *Ansys*® Fluent Student Version 2023 R1 has been used. All the meshes are created using *Ansys*® ICEM CFD 2023 R1 for the nozzles and *Ansys*® Turbogrid Student Version 2023 R1 for the blades, which design will be illustrated in chapter 4. The post-processing of the results has been done using in-house built Python codes and *Ansys*® CFD-Post Student Version 2023 R1.

In all the discussed examples, a steady simulation has been conducted using a Pressure-Based solver with a coupled scheme. For spatial discretization, a least squares cell-based approach has been employed for the gradient, while second-order accurate methods have been used for pressure and advective terms. Additionally, a pseudo-time method has been used, selecting a global time step.

From a historical perspective, for the simulation of a supersonic flow a Density-Based solver has been preferred, but, in the last years, Pressure-Based solvers are been adapted to this type of flow with good results [32].

For the initialization of the simulations, first-order upwind without the pseudo-time method has been used to increase the convergence speed.

The thermodynamic model, in the case of perfect flow, is the perfect gas model already implemented in Fluent, tailored by inserting the molecular weight of the fluid in use and the specific heat at constant pressure computed in the Python code. In the case of non-ideal gas, which will be discussed afterward, the NIST non-ideal gas model implemented in RefProp [33] has been used. For the computation process, a look-up table has been created, with spacing equal to 0.1 K for the temperature and a pressure spacing equal

to 0.1 bar or 100 pa. The selection of the latter is dependent on the maximum total pressure. To give an example, in the case treated in Section 2.5.6, where the maximum total pressure is equal to 200 bar, a spacing of 0.1 bar has been used

For the turbulence modeling, all the nozzles, except for one case, are simulated under the inviscid hypothesis, in agreement with the hypothesis of the MoC. For the viscous nozzle and the blades simulations, the $k-\omega-SST$ model implemented in $Ansys^{®}$ Fluent has been used, with a y^+ goal equal to 1. In general $y^+ < 2.5$ is guaranteed in all the viscous cases treated.

For the symmetric MoC only half of the passage area is simulated.

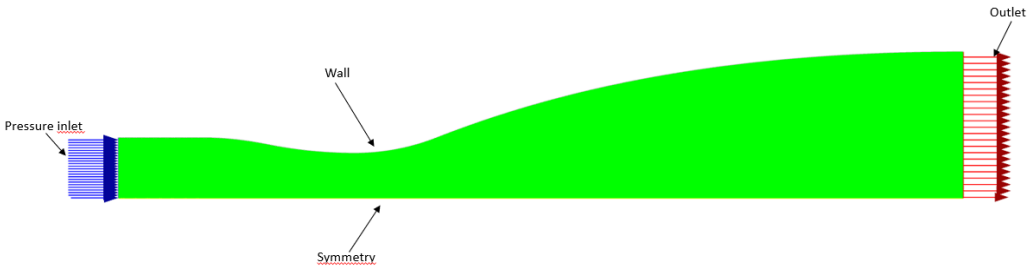

Figure 2.15: Example of mesh used to simulate a planar symmetric nozzle with the type of boundary condition used.

2.4.2. Mesh independence analysis

To study the independence of the results concerning the mesh used, a grid independence analysis has been conducted using the method presented in [34].

The example studied uses CO_2 with a perfect gas model as fluid, stagnation quantities equal to $P_t = 200$ bar and $T_t = 500°$ C, design Mach number equal to 2.5, and inlet Mach number equal to 0.5. The CFD simulation has been done under the hypothesis of inviscid flow. The fluid is identified with a molar mass equal to 44.009 g/mol and $\gamma = 1.27$ [16]. The geometry is fixed with the half-throat height computed so that the mass flow passing through the total nozzle is equal to 1 kg/s. The thickness b is equal to 1 mm, and the radius of curvature is equal to ten times the semi-throat height for the convergent part and five times the semi-throat height for the divergent part.

The number of elements of the three meshes used for the analysis is reported in Table 2.1. These values are computed by doubling the number of cells along the vertical and horizontal directions. Because of that, in the medium mesh, there are four times the cells of the coarse mesh. For the fine case, the number of cells is slightly less than four

times the number of the medium case because the Student version of *Ansys*® Fluent is limited to 512k nodes. This, anyway, guarantees a refinement factor higher than the value suggested in [34], equal to 1.3.

A first check is made by examining the Mach iso-lines of the different meshes. From Figure 2.16, it is possible to notice that the medium and fine meshes give nearly the same results. The only slight difference is present in the area where the kernel and reflex are connected, where a small shock can be detected, created by the noncontinuity of the first derivative between the prescribed wall and the wall designed in the reflex region. However, the presence of this shock does not affect the overall flow field.

Another difference between all three cases can be found near the outlet of the nozzle, where the iso-line with $M = 2.5$ is plotted. This difference is caused by the presence of the outlet and so the presence of a boundary condition that forces a zero-gradient flow, that influences the solution computed by the CFD. A way to resolve this issue may be to lengthen the nozzle by adding a straight line after its endpoint so that the added distance decreases the influence of the boundary condition on the non-uniform flow. This solution has not been implemented to remain in agreement with the cases found in the literature.

For the grid convergence analysis, Mach values along the axis of symmetry are studied. Figure 2.17a and 2.17b are in agreement with the previous observation made on Mach iso-lines. The presence of errors near zero is explained by the presence of the same qualitative and quantitative distribution of M along the axis of symmetry for the three different meshes.

The local order of accuracy p varies between 0.0034 and 13.0166, with an average value of 2.0987, meaning that some irregularities are present. However, because all three solutions tend to converge to a single one, it is possible to establish that the solutions have reached the asymptotic range [35].

Lastly, it is possible to observe an oscillatory convergence in 34% of the total data analyzed.

Based on the results of this analysis, the medium mesh has been chosen for all subsequent verifications. It enables the detection of even minimal unstable phenomena with an acceptable computational cost.

Name	Number of cells
Coarse	33 156
Medium	136 900
Fine	495 574

Table 2.1: Number of elements of the meshes used for the grid independence analysis.

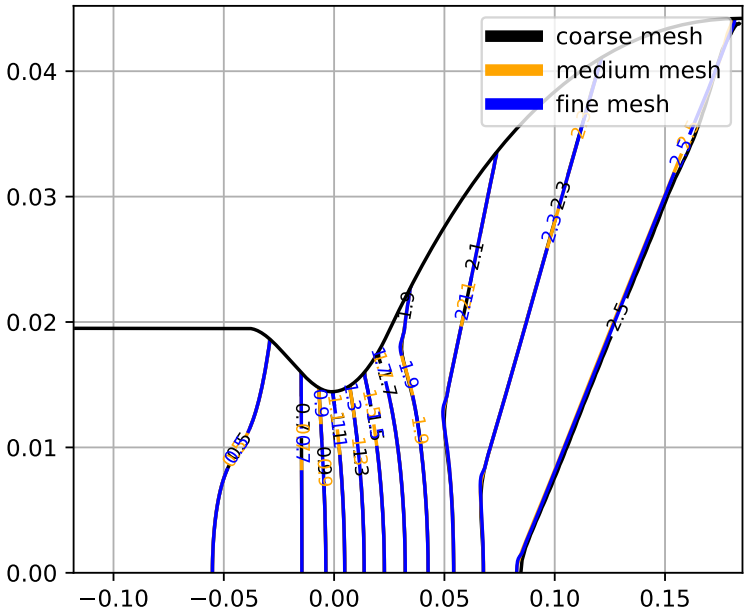

Figure 2.16: Mach iso-lines for different grid refinement.

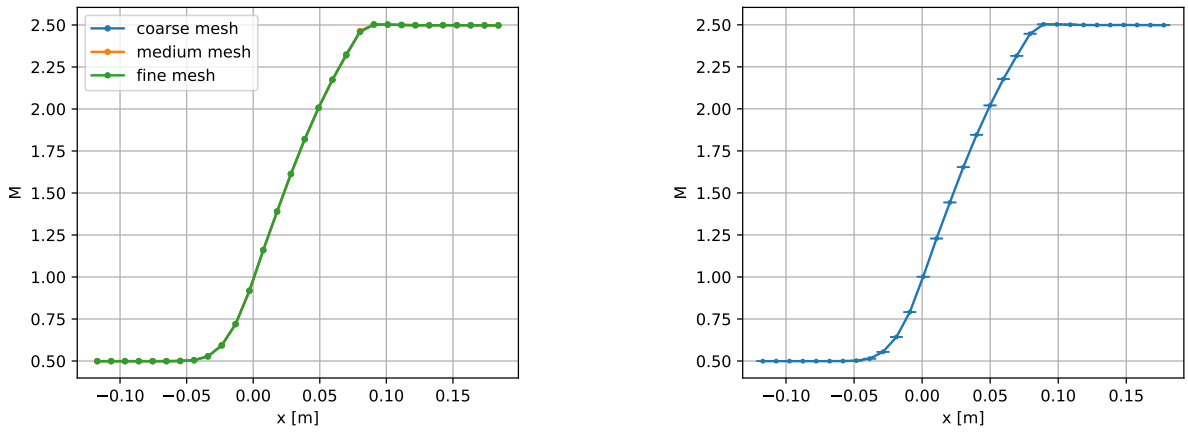

(a) (b)

Figure 2.17: (a) Variation of Mach along the axis of symmetry. The data extracted from the CFD results have been interpolated using a cubic spline to reduce the number of points for clarity. (b) Error bars are computed using the fine-grid convergence index of M along the axis of symmetry with the value of M computed with the fine mesh.

2.4.3. Verification of the planar symmetric MoC for perfect gas

In this section, the MoC code has been verified by comparing the results of the Python code with the ones coming from the simulated CFD nozzle. The case considered is the same as in the grid independence analysis.

The main goals are to verify that the Mach of design is reached, the outlet flow is uniform, no shocks are present, the values of Mach number and pressure computed by the MoC are in agreement with the results of the CFD simulation, and the throat has been modeled correctly. To verify this last point the mass flow and the position of the sonic line with respect to the one computed using Sauer is checked.

Firstly from Figure 2.18a, it is possible to see that the goal Mach is reached, Figure 2.18b shows that the expansion of the fluid happens especially in the convergent and kernel region. It is also possible to notice that the flow is uniform at the outlet.

The Mach iso-lines computed using MoC and CFD overlap each other for low Mach, with some limited differences in the reflex region. It is also possible to notice a small and very limited shock in the interface between the kernel and the reflex. This behavior may be seen also in literature [36] where has limited or no effects on the overall flow as here. If we focus on the throat region, the position of the sonic line is predicted well, even if the CFD one is more curved with respect to the Sauer one. The mass flow from the CFD simulation is G_{CFD}=1.0039 kg/s, with a relative difference equal to 0.39% from the objective one, demonstrating that the mass flow is computed with acceptable accuracy by the MoC.

Along the wall and the axis of symmetry, the Mach number is correctly estimated, in contrast with a pressure that is slightly overestimated. A possible cause for this mismatch (the relative error is about 8%) is the small shock observed before. Along the wall the presence of a pocket with low-speed flow in the subsonic region, where the convergent nozzle starts, is observable. This pocket is quite limited and it is caused by the convergent design, for which established design guidelines are presently not available. Although the effect of the convergent section does not arguably affect the subsequent flow evolution, a smoother change of the wall slope may be advised.

With this analysis, the MoC for a perfect gas is considered verified, as it can predict the flow field inside the convergent-divergent nozzle with acceptable accuracy.

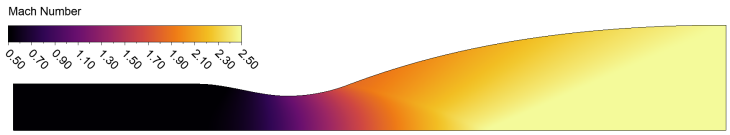

(a)

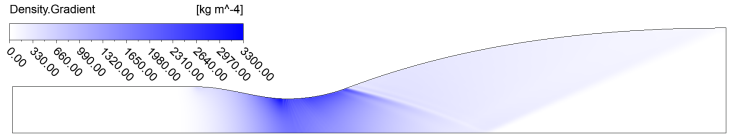

(b)

Figure 2.18: (a) Mach number contour and (b) density gradient for CO_2 perfect case.

2.5. Planar symmetryc MoC with non-ideal gas model

As widely demonstrated in the literature [13, 16, 18, 22, 36], the dense and non-ideal gas effects have a significant influence on the efficiency of a machine that operates with a complex fluid in a thermodynamic state near the saturation curve, as in an ORC expander. From this perspective, the design method must be complemented with the non-ideal-gas model, accepting the higher complexity and computational cost needed.

2.5.1. Short review of non-ideal gas properties

A brief recap of non-ideal gas dynamics is necessary to explain and model the supersonic flow of this type of fluid. More specifically, in this work, three non-dimensional parameters, commonly used to specify the gas dynamic of a non-ideal gas, are introduced.

Compressibility factor

The so-called compressibility factor Z can be used to define the deviation of a gas, at a given thermodynamic state, from its ideal behavior.

This quantity is defined as :

$$Z = \frac{P}{\rho R T} \tag{2.62}$$

By recalling the ideal gas law:

$$P = \rho R T \tag{2.63}$$

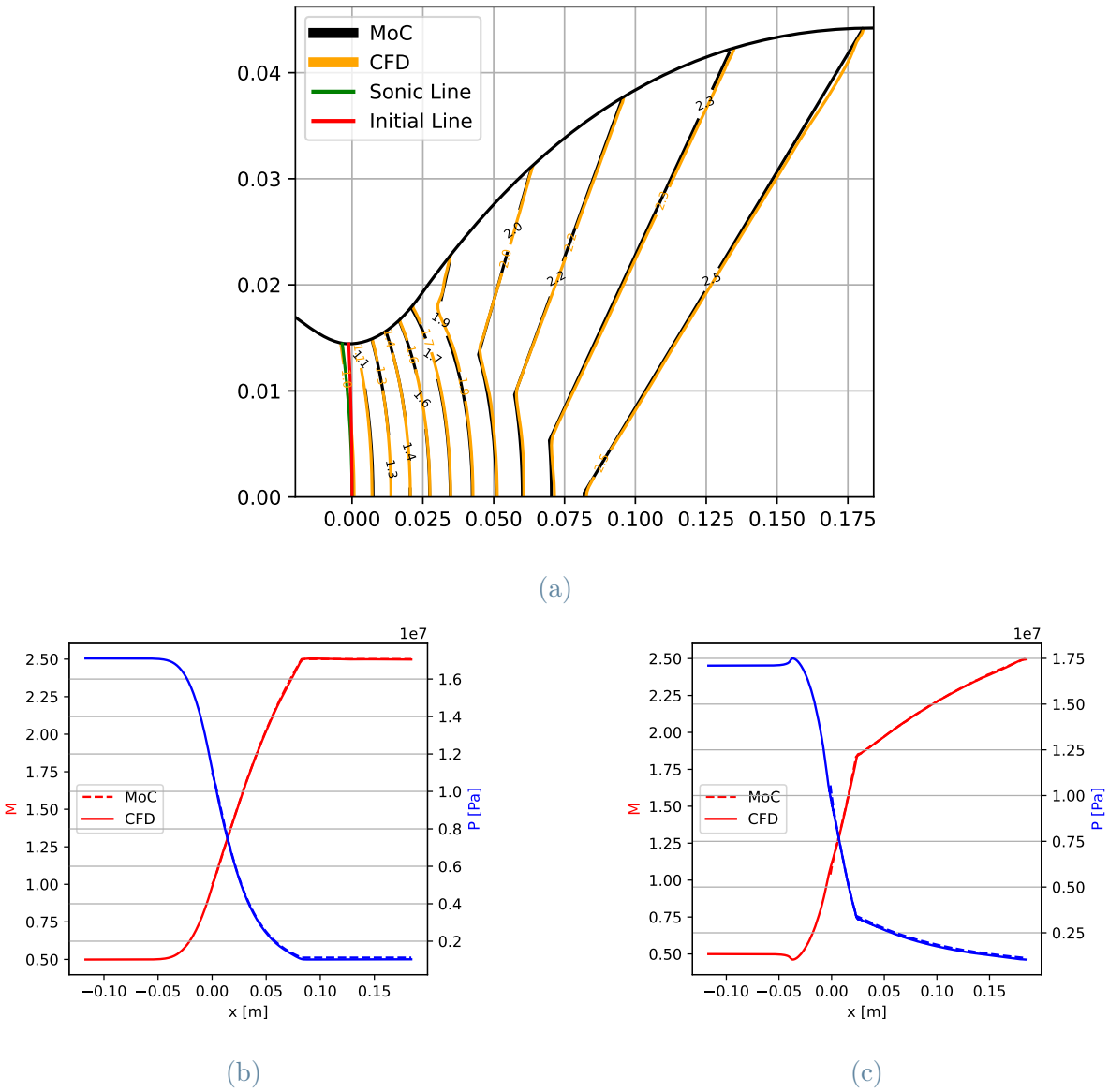

Figure 2.19: MoC-CFD comparison for (a) Mach number iso-lines, Mach and pressure along (b) the axis of symmetry and (c) the wall for CO_2 perfect case.

it is easy to notice that Z is the ratio between the pressure computed using the ideal gas law and the actual one. In the case of ideal gas $Z = 1$ while, for a non-ideal gas, the deviation may be negative ($Z < 1$) or positive ($Z > 1$) [16].

Usually, the closer a gas is to its critical point, the more its behavior deviates from the ideal gas. For example, in Figure 2.20a, which depicts a temperature-entropy (T-s) chart for pentane, Z decreases when increasing temperature and pressure, reaching a minimum of 0.6 at supercritical pressure ($P > P_c$).

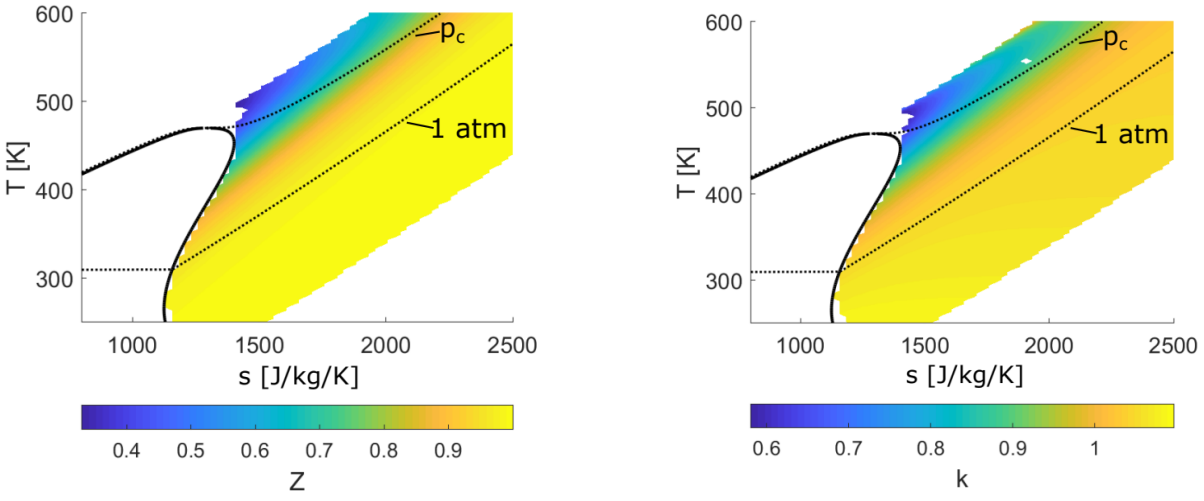

(a) (b)

Figure 2.20: Contours of (a) Z and (b) k for pentane on $T - s$ diagram [16].

Isentropic exponent

It is possible to define an isentropic expansion of a semi-perfect gas from the general polytropic expansion equation:

$$P\nu^n = const \tag{2.64}$$

using as exponent

$$n = \gamma = \frac{c_p(T)}{c_\nu(T)} \tag{2.65}$$

Under the aforementioned assumption $n > 1$ always but, because the heat capacities are functions of temperature, their values depend on the exact thermodynamic state. A further simplification may be made in the case of an ideal gas, where both c_p and c_ν are constant, and so also n.

But, if the gas diverges from its ideal behavior, two important effects appear: firstly the two heat capacities are not only a function of the temperature, but also of the pressure, and, more important, the equation (2.65) is no more valid.

For this reason, γ is substituted by the so-called (generalized) isentropic exponent k, which describes the relative change of density ρ and pressure P over an isentropic expansion. This quantity can be defined as:

$$k = \frac{\rho}{P}\left(\frac{\partial P}{\partial \rho}\right)_s \tag{2.66}$$

It is important to consider that, if for a perfect or semi-perfect gas $\gamma > 1$ is always true, k can take also values lower than one, as happens, for example, in an ORC turbine [16].

As we can observe in Figure 2.20b, k has a behavior similar to Z, meaning that, as expected, k and Z are coupled in a non-ideal gas.

During the definition of isentropic expansion made before, an important hypothesis is made: the fluid is polytropic. This means that, along a given expansion, the exponent n is constant. If this is always true for an ideal gas, this is not always the case for a non-ideal one.

As explained in [16], it is always possible to interpolate an expansion process using a second-order approximation, obtaining:

$$\log\left(\frac{P}{P_t}\right) = \alpha_{poly}\log\left(\frac{\rho}{\rho_t}\right)^2 + \widetilde{k}\log\left(\frac{\rho}{\rho_t}\right) \tag{2.67}$$

If we consider, as before, the pentane as fluid, is possible to observe that for $Z > 0.8$, so for limited deviation from ideal behavior, $\alpha_{poly} \approx 0$, and so it is possible to define a constant k as:

$$\log\left(\frac{P}{P_t}\right) = k\log\left(\frac{\rho}{\rho_t}\right) \tag{2.68}$$

that is the definition of polytropic expansion.

If we consider the opposite case, so $Z < 0.8$, the possible values of α_{poly} can become relatively large and so k is no longer constant.

This fact has an important effect on the Prandtl-Meyer angle and, as it will be explained later, also in the application of a MoC.

Fundamental derivative

The so called fundamental derivative of gasdynamic Γ is defined as [37]:

$$\Gamma = 1 + \frac{\rho}{c}\left(\frac{\partial c}{\partial \rho}\right)_s \tag{2.69}$$

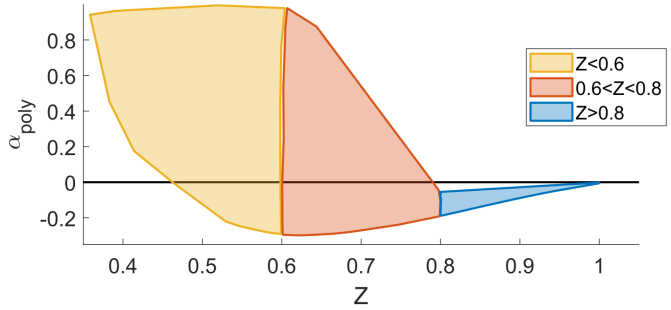

Figure 2.21: Possible value of α_{Poly} for different Z for pentane [16].

This quantity is frequently employed to describe the gas-dynamic behavior of a dense fluid inside an ORC turbine. It is closely related to the isentropic exponent and provides information about how the speed of sound changes along an isentropic expansion.

Γ turns out to be constant for a perfect gas and it is equal to:

$$\Gamma = \frac{\gamma + 1}{2} \tag{2.70}$$

Γ becomes very useful if we want to know whether the expansion occurs into the so-called dense gas region or not. This has an important effect on how the speed of sounds evolves during an expansion.

If $\Gamma > 1$ a gas exhibits the so-called classical behavior, where the speed of sound drops in an isentropic expansion, as the density. Only compression shocks are present, and it is important to note that, in general, this is true for most gases [37].

Instead, if $0 < \Gamma < 1$ the fluid is in the dense gas region and so the speed of sound increase while the density decrease. If a gas is in this state, the Mach number can have two different behaviors. If the expansion occurs in the so-called dilute-gas condition, the qualitatively and quantitatively distribution of the Mach number along an expansion is similar to the one computed from an ideal-gas model [38]. If the gas is outside this region, not only the quantitative but also the qualitative distribution of the Mach number can change dramatically, with its evolution that can become non-monotonic if it is over its critical pressure. This behavior is called non-classical gas flow.

To explain when this can happen, we consider a quasi-one-dimensional flow with uniform entropy and constant total enthalpy. In this type of flow, the Mach number is a function of the density ρ only. The non-dimensional parameter J can be introduced as a measure

of the Mach number derivative with respect to the density [38].

$$J = 1 - \Gamma - \frac{1}{M^2} = \frac{\rho}{M}\frac{dM}{d\rho} \tag{2.71}$$

$J > 0$ is the necessary condition to have a decrease of M along an isentropic expansion. It can be demonstrated that for a perfect gas, as well as flow with $\Gamma > 1$, $J < 0$ is always true.

As before, only compression shock waves may be present but with lower related shock losses [13]. This type of flow can be observed, for example, in ORC turbines [36].

In theory, it is possible to operate in a region where $\Gamma < 0$, and so the classical gas dynamics are inverted, causing the existence of rarefaction shocks and compression waves. A gas that exhibits this behavior is called Bethe-Zeldovich-Thompson (BZT) gas. However, as of today, there is no experimental proof of this abnormal behavior [18].

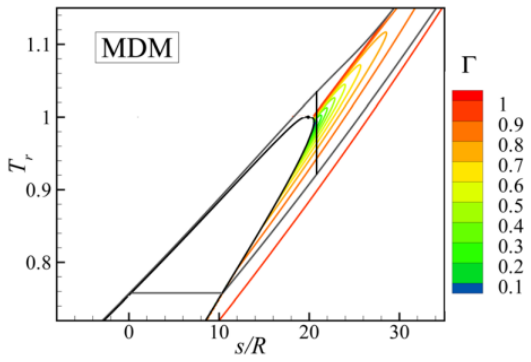

(a)

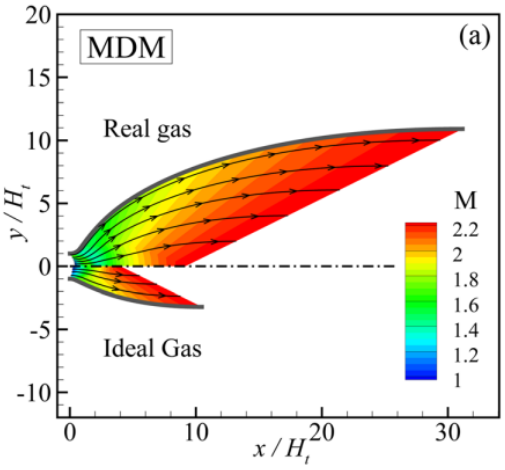

(b)

Figure 2.22: (a) Expansion in the $T - s$ chart with iso-Γ lines superimposed [36]. (b) Difference between a nozzle designed with ideal or non-ideal gas model for MDM [36]. Note that for this case, $\gamma = \frac{C_p}{C_v} = 1.017$ is computed in the dilute gas limit (at the critical temperature and low pressure), and, by applying equation (2.70), is possible to demonstrate that the fluid behaves as a perfect one if $\Gamma = 1$.

2.5.2. Effects of non-ideal and dense gas behavior in MoC application

In this part of the work, only the effects related to the design of a non-ideal gas nozzle are treated.

The first one-dimensional effects of non-ideal gas-dynamic on the design of a supersonic nozzle can be observed by comparing two nozzles, one designed using a perfect gas law and the other with a non-ideal gas one, under the hypothesis of the same thermodynamic state at the inlet and outlet: the nozzle designed with a non-ideal MoC is longer and has a larger outlet passage compared to a nozzle designed with a perfect one.

The different passage areas can be easily explained by the different values of the isentropic exponent, which causes the necessity of a different area ratio to reach the same outlet Mach [16]. This area ratio is lower for higher exponent, explaining also why, using an ideal gas model, a more complex fluid presents a slightly greater exit area concerning a more simple fluid.

The different lengths may be explained by recalling the quasi-one-dimensional-flow relations [36]:

$$\frac{dP}{dx} = \frac{\rho u^2}{P}\frac{1}{1-M^2}\frac{P}{H}\frac{dH}{dx}, \qquad \frac{dM}{dx} = -\frac{1+(\Gamma-1)M^2}{1-M^2}\frac{M}{H}\frac{dH}{dx} \tag{2.72}$$

where $H = H(x)$ is the local value of the nozzle semi-height. Notice that the passage area of a planar symmetric nozzle can be defined as $A = 2Hb$, where b is the nozzle thickness.

These two equations demonstrate that the gradients of P and M along an isentropic expansion are a direct function of Γ, and so a slower evolution of these quantities is expected for strong non-ideal behavior. This implies that also a lower evolution of $\frac{dA}{dX}$ is expected [22].

The isentropic exponent has also another effect, this time two dimensional, connected to its influence in the Prandtl-Meyer function of the fluids, that, recalling equations (2.10) and (2.11) may be used to define the compatibility equation along a characteristic.

As been demonstrated by Wheeler and Ong [18], for a gas that obeys to a politropic law, ν can be expressed as:

$$\nu = \frac{1}{\xi}\tan^{-1}(\xi\beta) - \tan^{-1}(\beta) \qquad \text{if k>1} \tag{2.73}$$

$$\nu = \cot^{-1}(\beta) + \beta - \frac{\pi}{2} \qquad \text{if k=1} \tag{2.74}$$

$$\nu = \frac{1}{z}\tanh^{-1}(z\beta) - \tan^{-1}(\beta) \qquad \text{if k<1} \tag{2.75}$$

where

$$\xi = \sqrt{\left(\frac{k-1}{k+1}\right)} \tag{2.76}$$

$$\beta = \sqrt{M^2 - 1} \tag{2.77}$$

$$z = i\xi \tag{2.78}$$

These equations demonstrate that, to reach the same M, a higher Prandtl-Meyer turning angle is needed. An experimental visualization of this phenomenon may be found in the trailing edge of a blade: at the same M, fluids with lower k will have higher turning around the trailing edge. The equations from (2.73) to (2.75) show also that for lower k the maximum turning angle increases and, for $\kappa < 1$, is equal to infinite. In this last case, the maximum Mach number reached is $M_{max} = \sqrt{-2/(k-1)}$.

Notice that equations (2.73), (2.74) and (2.75) are true only if the working fluid is polytropic and, as demonstrated in [16], this is not always the case, meaning that for flow with high non-ideal gas effects the Prandtl-Meyer angle computed in this way may be not precise. This is the main reason why in this work the MoC developed by Zucrow and Hoffman [19] is preferred concerning the method present in Anderson [24], adapted by Wheeler and Ong [18] to a non-ideal flow. In reality, as mentioned before, some examples where the Prandtl-Meyer angle has been used to resolve non-polytropic flows may be found in literature [25]. In this last case, the Prandtl-Meyer angle has to be computed using an iterative process.

Another important consideration is the potential presence of a region where dense gas effects can occur. In conditions of dilute gas, the Mach number evolution closely aligns with predictions from a perfect gas law. However, beyond this region, especially if the flow surpasses its critical pressure, the Mach number evolution during expansion can significantly deviate from the behavior anticipated by a perfect gas law. This deviation may lead to non-monotonic variations of the Mach number. With the exception of a flow in the dilute gas region, a non-ideal gas model is imperative to accurately adjust the nozzle shape and attain the desired outlet Mach number. It is essential to note that the

presence of non-classical gas dynamics is typically confined to localized regions in most practical applications, as highlighted by Wheeler and Ong [18].

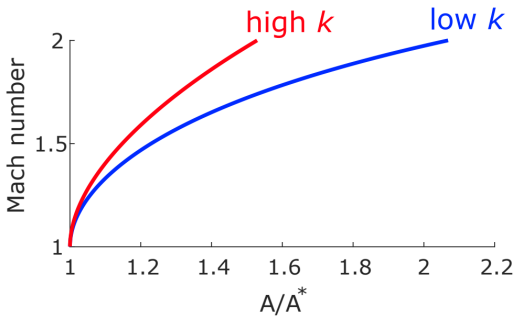

Figure 2.23: M as function of area ratio for different k [16].

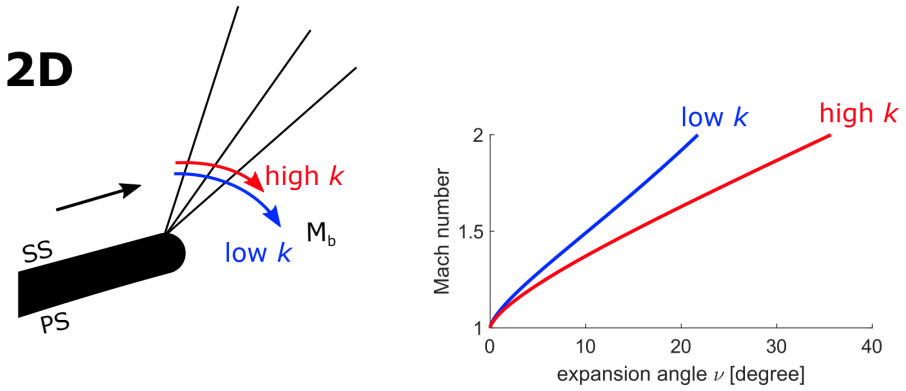

Figure 2.24: Effects of k on the Prandtl-Meyer angle [16].

2.5.3. Perfect nozzle applied to a non-ideal flow

To study how a nozzle designed with the perfect MoC presented previously behaves in the case of the presence of non-ideal gas effects, a CFD simulation with a non-ideal gas model has been made. The idea, in this case, is to try to mimic what happens if a nozzle is designed with a perfect gas law but is operated in a thermodynamic region with strong non-ideal gas effects (eg. $Z_t = 0.65$).

This simulation used the same input, both thermodynamic and geometric, of the case SH1.5 explained in Section 2.5.6

The fluid has been defined in the MoC algorithm with $R_g = 236.53$ g/mol [39] and $\gamma = 0.857$. This last value has been computed using the so-called Equivalent-γ gas model proposed by Wheeler and Ong [18].

The expansion inside the nozzle is modeled as a polytropic relationship of the type:

$$\frac{P}{\rho^k} = \frac{P_t}{\rho_t^k} \tag{2.79}$$

where

$$k = \gamma_{eq} = \frac{\sum xy - \frac{\sum x \sum y}{n}}{\sum x^2 - \frac{(\sum x)^2}{n}} \tag{2.80}$$

with $x = \log\left(\frac{\rho}{\rho_t}\right)$, $y = \log\left(\frac{P}{P_t}\right)$ and n=1000.

Notice that to apply this model the pressure and density field have to be known at least along one streamline. For example, Bufi [13] uses this method but in his version of MoC the distribution of $P(x)/P_t$ along the axis of symmetry is fixed instead of the prescribed kernel wall.

In this work, the data necessary to compute γ_{eq} have been extracted along the axis of symmetry from a previously done non-ideal CFD simulation. This has been done only to have a reasonable value of γ, avoiding the complete variation of the MoC algorithm suggested by Wheeler and Ong. In accordance with Bufi [13], the method of Wheeler and Ong gives results comparable to the one presented by Zucrow and Hoffman [19], that has been implemented in this work.

The first difference between CFD and MoC is the mass flow rate: in the first case is equal to 1.387 kg/s whereas in the second is 1.199 kg/s, meaning that a relative difference is present and equal to $\frac{G_{MoC}-G_{CFD}}{G_{MoC}} = -15.7\%$. This difference in the mass flow is related to the completely different thermodynamic conditions computed in the throat using perfect and non-ideal equations of state.

If we observe the Mach contour and the Mach and pressure field along the wall and the axis of symmetry it is possible to notice how the MoC is not able to catch the real expansion of the fluid. From Figure 2.25b and 2.25c is clear that the Mach goal of 1.50 is not reached with the maximum value of the CFD equal to 1.46. The difference is quite limited because the value of γ is based on the precise expansion studied, and the difference between the area ratio for different k increases as Mach increases, starting from the same value at M=1, as shown in Figure 2.23.

This observation is further supported by the Mach iso-lines shown in Figure 2.25a: the throat computed using Sauer is nearly equal to the one from CFD, especially near the axis of symmetry. As indicated in the literature, it is noted that an initial-value line can be computed using Sauer with an ideal gas without substantial modification in the case of

non-ideal flow [26, 36]. The difference between CFD and MoC increases with the increase of M, reaching its maximum at the outlet

The conclusion of this analysis can be summarized as follows: a MoC with a perfect gas model is unable to predict the expansion of a supersonic flow where strong non-ideal behavior is present, particularly at high M. This motivates the investigation of a MoC implemented with a non-ideal gas model. While the necessity of adapting the initial-value line may be more questionable, the fact that a slight error in the initialization can cause appreciable differences in the MoC results justifies it.

2.5.4. Implementation of the processing units with non-ideal gas model

As explained before, the adaptation of the implemented method is quite simple and the only change needed is on the external function used to compute the speed of sound.

To do that, the equation of state implemented in RefProp [33], available in Python through the CoolProp library [40], is used. More precisely, starting from the total pressure and temperature at the inlet, the entropy s and the total enthalpy h_t are computed and kept constant in all the nozzles because of the hypothesis of irrotational flow made initially.

Every necessary thermodynamic quantity can be computed using the Coolprop libraries. The thermodynamic state is defined using s and h as inputs. This latter quantity can be computed using the definition of total enthalpy [22]:

$$h + |V|^2/2 = h_t \tag{2.81}$$

where $|V|$ is the magnitude of the flow field velocity, that is known.

2.5.5. Implementation of the initial line with non-ideal gas model

Despite the observation that the definition of an initial-value line with a non-ideal gas model is deemed less critical than adapting the MoC algorithm, as discussed in Section 2.5.3, two adaptations of the Sauer model [19, 27], have been proposed. Both are based on the resolution of the velocity potential equation (2.82) in the transonic for a non-ideal flow. The first, called Γ-model, proposed by Guardone [41], is based on the use of the fundamental derivative of the gas dynamic to link the equation of the velocity potential, equation (2.82), with the value of the speed of sound. In the second model, proposed in this dissertation and called k-model, the function of Γ is substituted by the isentropic

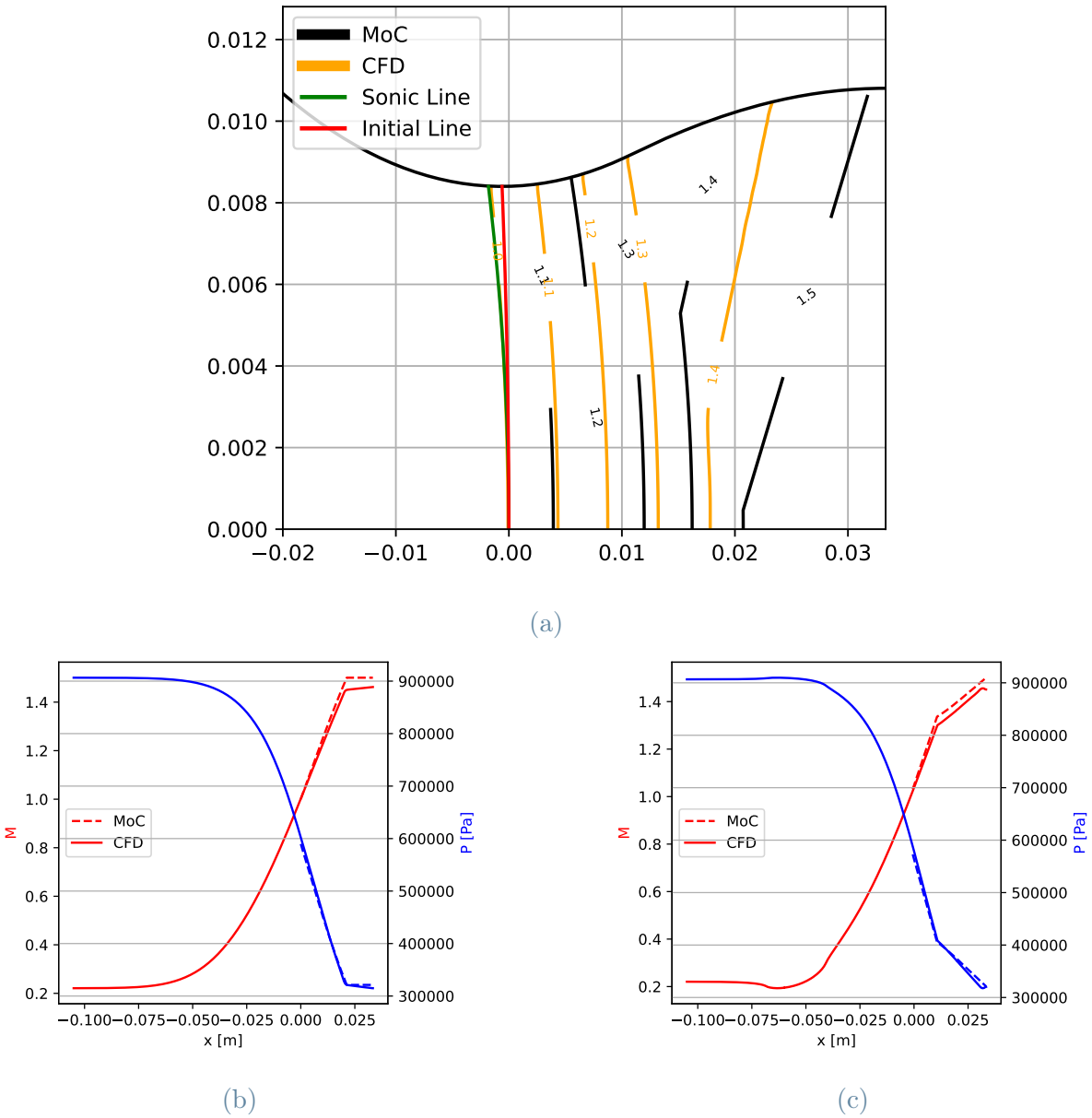

(a)

(b)

(c)

Figure 2.25: MoC-CFD comparison for (a) Mach number iso-lines, Mach and pressure (b) along the axis of symmetry and (c) the wall for the case SH1.5 designed with perfect gas model.

exponent.

Γ-model

The equation of the velocity potential (2.44) is obtained under the hypothesis of perfect flow. The general equation can be written as [41]:

$$(\phi_x^2 - c^2)\phi_{xx} + 2\phi_x\phi_y\phi_{xy} + (\phi_y^2 - c^2)\phi_{yy} = 0 \tag{2.82}$$

where the scalar velocity potential ϕ is defined as $(u, v)^T = \nabla\phi$, $\phi_i = \frac{\partial\phi}{\partial i}$ and $\phi_{ij} = \frac{\partial^2\phi}{\partial i \partial j}$.

The only link between equation (2.82) and the thermodynamic description of the fluid is the speed of sound

$$c^2(\nu, s) = -\nu^2 \left(\frac{\partial P}{\partial \nu}\right)_s \tag{2.83}$$

where ν is the specific volume.

All the thermodynamic quantities in the vicinity of the nozzle, such as P, ν, and c, are functions of the independent thermodynamic quantities s and h. The value of h can be computed using the definition of total enthalpy, equation (2.81). Therefore it is a function of the total enthalpy, which is constant and assigned by the total inlet quantities, and of the flow field velocity module $|V|$. Because s is constant and assigned at the inlet, the speed of sound, as well as all the other thermodynamic quantities in the throat, is a function of $|V|$ only.

If the flow is supposed ideal, $c(V)^2 = (\gamma - 1)(h_t - \frac{1}{2}V^2)$, thus an equation equivalent to equation (2.44) is obtained from equation (2.82).

By indicating with $\bar{}$ and $\tilde{}$ all the quantities evaluated at the constant reference state and perturbation quantities respectively, is possible to define $\bar{\Gamma}$ as the value of the fundamental derivative of gas dynamic at the sonic conditions. $\bar{\Gamma}$ is supposed constant and a $O(1)$, allowing to derive the equation of the perturbation velocity potential for a nonideal gas as [41]:

$$\left[\bar{M}^2 - 1 + 2\bar{\Gamma}\bar{M}^2\tilde{\phi}_x\right]\tilde{\phi}_{xx} - \tilde{\phi}_{yy} = 0 \tag{2.84}$$

This equation is not valid for flow with $\Gamma < 0$ because $\bar{\Gamma}$ is supposed as a $O(1)$.

Because $\bar{\Gamma}$ and γ are of the same order, equation (2.84) can be resolved with the same procedure of Sauer [27], obtaining the description of the flow field in the vicinity of the flow as [22]:

$$\tilde{u}(x, y) = c^*(1 + u') = c^*\left(1 + \alpha x + \frac{\bar{\Gamma}\alpha^2 y^2}{\delta + 1}\right) \tag{2.85}$$

$$\tilde{v}(x,y) = c^* v' = c^* \left(\frac{2\bar{\Gamma}\alpha^2 xy}{1+\delta} + \frac{2\bar{\Gamma}^2\alpha^3 y^3}{(1+\delta)(3+\delta)} \right) \tag{2.86}$$

with

$$\alpha = \left[\frac{(1+\delta)}{2\bar{\Gamma}\rho_t y_t} \right]^{1/2} \tag{2.87}$$

$$\epsilon = -\frac{\bar{\Gamma}\alpha y_t^2}{3+\delta} \tag{2.88}$$

Notice that, in the case of a perfect gas, $\bar{\Gamma} = \frac{\gamma+1}{2}$ and so these equations are equivalent to the ones obtained by Sauer.

The initial-value line may be computed in the same way as the ideal gas case, but this time using the equations (2.85) and (2.86). Thus, if the initial-value line is supposed to be the locus of the points where $\tilde{v} = 0$ a parabola of equation:

$$x = -\frac{\bar{\Gamma}\alpha y^2}{3+\delta} \tag{2.89}$$

is defined, with y that varies from 0 to Y_t.

This method has been verified by Zocca et al. [22] for a symmetric supersonic nozzle that expands MDM.

k-model

As briefly explained in section 2.5.1, the isentropic exponent k has the same meaning as γ for a non-ideal gas. In the vicinity of the throat, the thermodynamic properties can be considered constant, thus also k can be assumed constant as well and equal to its value computed at the sonic state $\bar{k}$. This is also in agreement with the previously mentioned method: Γ and k are closely connected, so if one of the two is constant, the other will be.

If k has the same meaning, from a conceptual point of view, of γ and it is constant, the perturbation equation for a non-ideal flow can be derived from equation (2.44), without substantial modification, by substituting γ with $\bar{k}$:

$$\left(1 - M_\infty^2\right) \frac{\partial u}{\partial x} + \frac{\partial v}{\partial y} + \delta \frac{v}{y} = M_\infty^2 \left(\bar{k} + 1\right) \left(\frac{u}{U_\infty} \right) \frac{\partial u}{\partial x} \tag{2.90}$$

The equation (2.90) can be resolved with the procedure used by Sauer because k and γ are of the same order, obtaining:

$$\tilde{u}(x,y) = c^*(1+u') = c^*\left(1+\alpha x + \frac{(\bar{k}+1)\alpha^2 y^2}{2(\delta+1)}\right) \tag{2.91}$$

$$\tilde{v}(x,y) = c^* v' = c^*\left(\frac{(\bar{k}+1)\alpha^2 xy}{1+\delta} + \frac{(\bar{k}+1)^2\alpha^3 y^3}{2(1+\delta)(3+\delta)}\right) \tag{2.92}$$

$$\alpha = \left[\frac{1+\delta}{(\bar{k}+1)\rho_t y_t}\right]^{1/2} \tag{2.93}$$

$$\epsilon = -\frac{(\bar{k}+1)\alpha y_t^2}{2(3+\delta)} \tag{2.94}$$

The equation of the initial line is computed as the locus of point where $\tilde{v} = 0$ and so

$$x = -\frac{(\bar{k}+1)\alpha y^2}{2(3+\delta)} \tag{2.95}$$

with y that varies from 0 to Y_t.

With respect to the Γ-model, the primary advantage lies in the ability to utilize the same model developed for an ideal gas without the need for new equations.

Differences and similarities between the two models

In this section, two nozzles, with the same thermodynamic input of the case SH2 (see Table 2.3 for the complete characterization) and the same geometry of the cases in Section 2.5.6 are compared. The only difference between the two is the model applied for the initial-value line: one, the benchmark, uses the Γ-model, and the other uses the k-model. The purpose of this comparison is to verify, based on the known efficacy of the model proposed by Guardone [22], whether the results are comparable.

It is noticeable that both models yield the same mass flow at the throat, equal to 1.351 kg/s in the MoC calculation, as the two initial-value lines computed by the two methods collapse into a single curve, as shown in Figure 2.27a. It is worth noting that the thermodynamic libraries used to compute the density value are the same. From the same figure, a complete overlapping of the two sonic lines, as well as the iso-lines at various Mach numbers, is observable.

The only difference between equation (2.84), the perturbation equation for a non-ideal flow using the Γ-model, and its counterpart obtained using the k-model, equation (2.90), is the substitution of $2\bar{\Gamma}$ with $\bar{k}+1$. This implies that if the equality (2.96) is satisfied, equations (2.84) and (2.90) are equivalent.

$$\bar{\Gamma} = \frac{\bar{\kappa}+1}{2} \tag{2.96}$$

To understand if this is true, the equation (2.69) is rewritten as:

$$\Gamma = \frac{1}{2}\left(k+1-\frac{\nu}{k}\left(\frac{\partial k}{\partial \nu}\right)_s\right) \tag{2.97}$$

Meaning that if $\left(\frac{\partial k}{\partial \nu}\right)_s = 0$, equation (2.96) holds true. This occurs, for example, in the case of an ideal gas, where $k = \gamma$ =const and equation (2.97) is reduced to $\Gamma = \frac{\gamma+1}{2}$.

Since, in the k-model, k is assumed to be constant in the vicinity of the throat, it is reasonable to suppose that its value is also constant with respect to ν, thus yielding equation (2.96).

To verify if the assumption of $\left(\frac{\partial k}{\partial \nu}\right) s = 0$ is true, the values of k, Γ, Γ$comp = \frac{k+1}{2}$, and the absolute value of $\frac{\nu}{2k}\left(\frac{\partial k}{\partial \nu}\right)_s$ are extracted from the CFD simulation results along the axis of symmetry and plotted in Figure 2.26. From this figure, it is evident that k and Γ can be considered nearly constant in the vicinity of the throat. On the contrary, the equality Γ = Γ$comp$ is not true because k is not constant with respect to ν. However, because k, Γ, and Γ_{comp} are of the same order, the equivalence between the two methods is reasonable.

Based on these findings, the k-model has been used in the next cases analyzed in this work.

2.5.6. Inviscid case verification

The verification of the non-ideal MoC can be divided into three phases.

In the first phase, the non-ideal MoC is verified against the perfect one. To do that, three nozzles are designed for every MoC version. The thermodynamic conditions are indicated in Table 2.2 and the main geometry parameters are the same as indicated in Section 2.4.3.

Because, as shown in Figure 2.28a, all three expansions happen in a region with Z near one, no or very limited differences are expected between ideal and non-ideal nozzles.

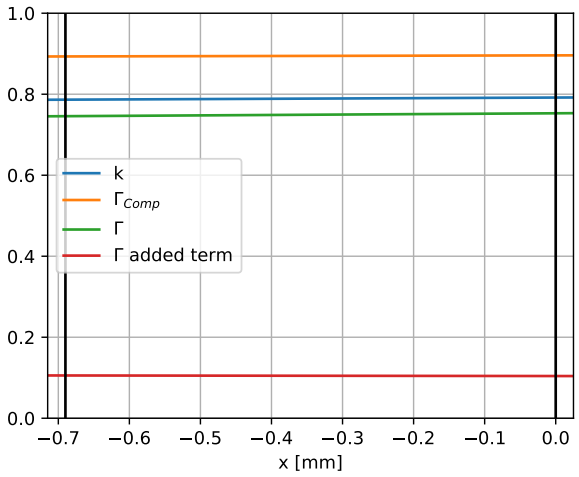

Figure 2.26: value of k, Γ, $\Gamma_{comp} = \frac{k+1}{2}$ and Γ added term, that is the absolute value of $-\frac{\nu}{2k}\left(\frac{\partial k}{\partial \nu}\right)_s$, along the axis of symmetry in the vicinity of the throat.

In the second phase, the same nozzle treated in Section 2.4.3 is redesigned using the non-ideal MoC and then verified through a CFD simulation to check if the algorithm can model the supersonic flow in its non-ideal version.

In the third part, six cases are studied, allowing the verification of the MoC for different levels of flow non-ideality. In all these cases the inlet Mach number is equal to 0.2 and the geometrical data of the nozzle designed by Spinelli et al. [42] are used. This means that all six have a fixed semi-throat height equal to $Y_t = 8.4$ mm, and a nozzle thickness equal to 18.7 mm. For the cases with $M_d = 1.5$ both the convergent and divergent radius of curvature are equal to ten times Y_t, whereas in the cases with $M_d = 2$, the radius of curvature is near 7.4 times Y_t for the convergent and ten times for the divergent one. The thermodynamic data are reported in Table 2.3.

CO_2 verification

As shown in Figure 2.30, the difference between two nozzles, one designed with perfect MoC and the other with non-ideal MoC, at the same thermodynamic inputs, increases if the outlet Mach increases, even if all the expansion takes place in a region with Z near one. This can be explainable by considering that k computed during the expansion is slightly different from the value of γ supposed for the design of the perfect nozzle and is not constant. This is confirmed by Figure 2.29, where k is near 1.23 in the reflex region, slightly lower than the supposed γ, equal to 1.27.

The case studied to verify the non-ideal MoC is the one indicated as NP in Table 2.3.

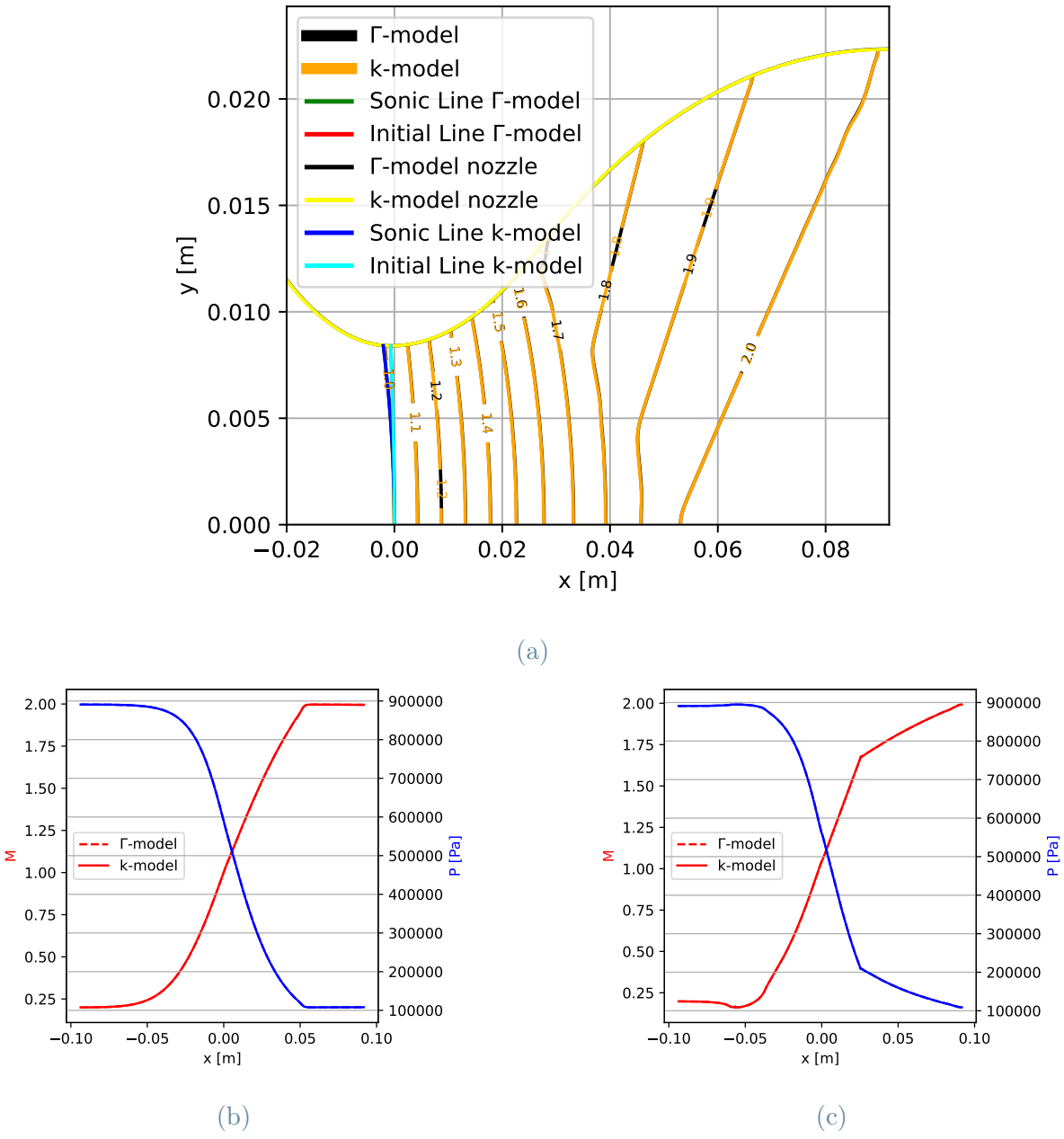

(a)

(b)

(c)

Figure 2.27: (a) Comparison between Mach number iso-lines, Mach and pressure along (b) the axis of symmetry and (c) the wall for the case SH2 with Γ and k model.

To compare the ideal and non-ideal cases the main geometry parameters are maintained equal, thus $b = 1$ mm, $R_{conv} = 10Y_t$ and $R_{div} = 5Y_t$ with semi-throat height $Y_t = 14.44$ mm.

From the analysis of the CFD results, another difference between perfect and non-ideal cases is the mass flow, with a value of 1 kg/s for the first and 0.9886 for the latter, with a relative difference equal to 1.14%. The presence of a higher mass flow for the ideal case,

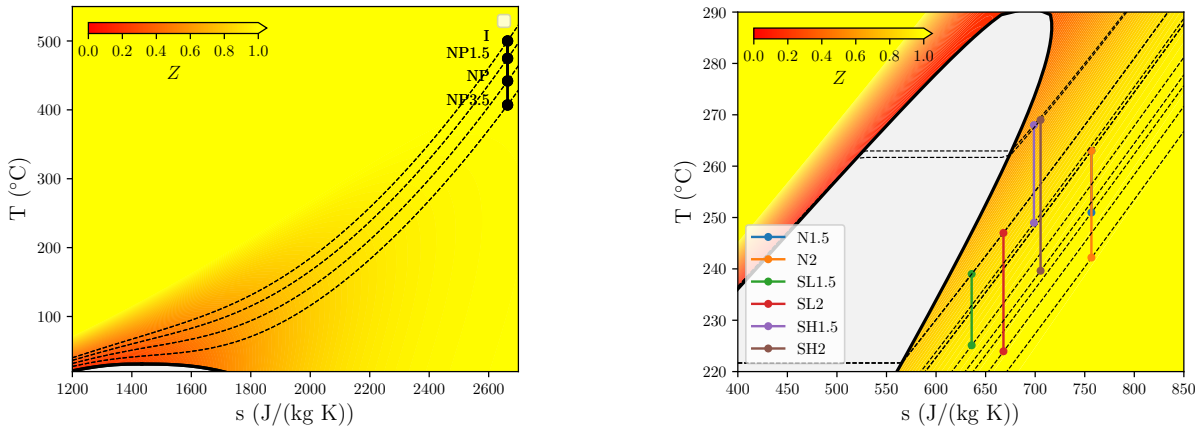

(a) (b)

Figure 2.28: (a) Plane T-s for CO_2, I is the inlet. (b) Plane T-s for MDM, cases N1.5 and N2 are overlapped because they have the same inlet.

Name	fluid	T_t[°C]	P_t [bar]	M_d
NP1.5	CO_2	500	200	1.5
NP	CO_2	500	200	2.5
NP3.5	CO_2	500	200	3.5

Table 2.2: Thermodynamic conditions used for the comparison between nozzles designed with ideal and non-ideal MoC.

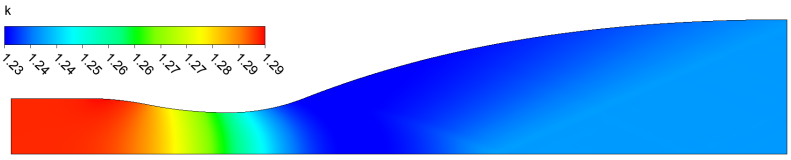

Figure 2.29: Isentropic exponent for the NP case computed with non-ideal MoC

at constant throat height and total inlet condition, is in agreement with the results of Section 2.5.3, meaning that the use of a perfect gas law, even in a situation with Z near to 1, tends to overestimate the actual mass flow.

Lastly, it is possible to notice that the non-ideal MoC can predict the actual supersonic flow in the divergent nozzle. A slight mismatch between the Mach iso-lines at high M (Figure 2.32a) is observable. However, because the difference is limited, the accuracy of the prediction remains acceptable. Notice that this happens also in the ideal case (see Figure 2.19a) and for both cases, it can be caused by error propagation.

In the same figure, a very limited shock at the kernel-reflex interface is observable, caused

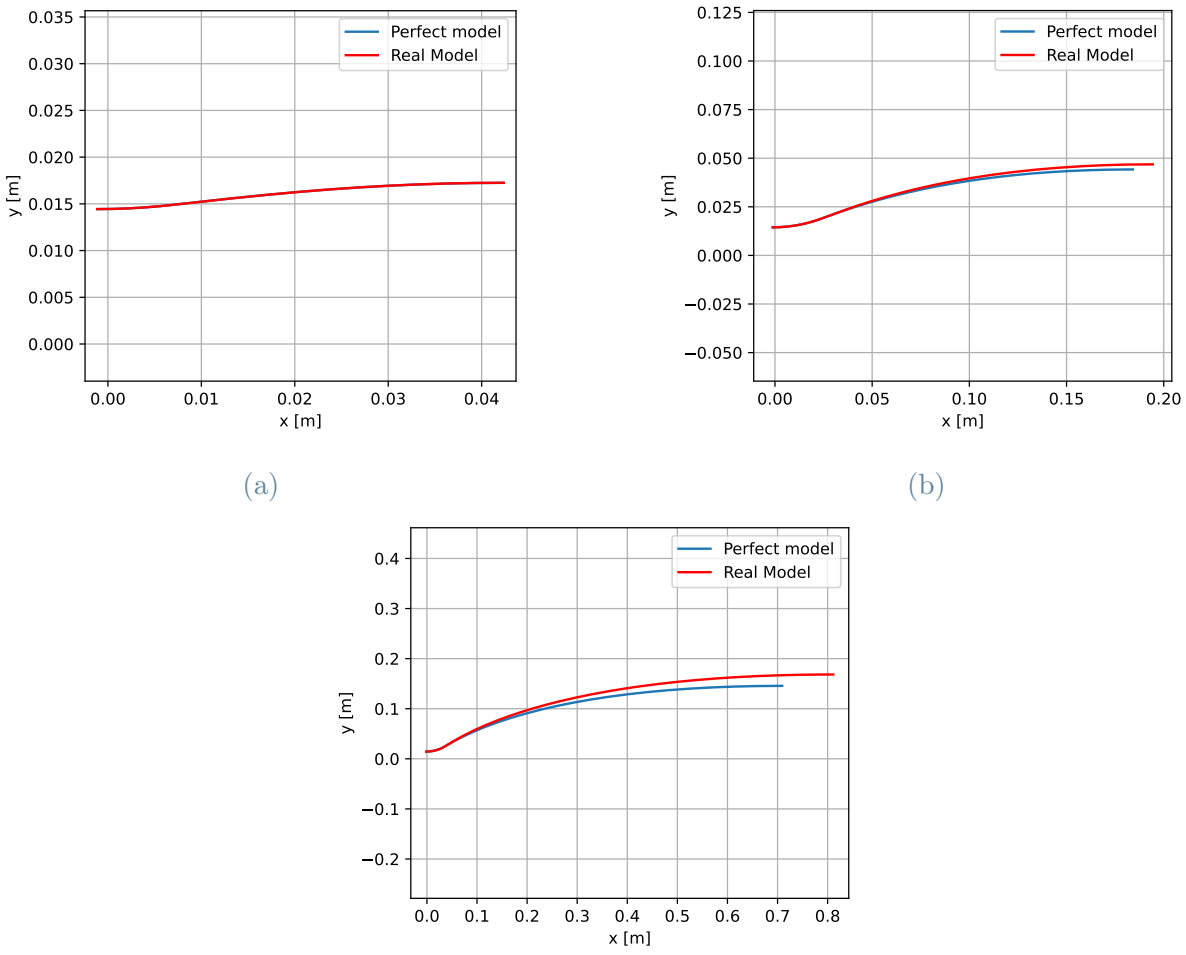

Figure 2.30: Comparison between the perfect and non-ideal nozzles designed with NP inlet total quantities and outlet Mach equal to (a) 1.5 (b) 2.5 (c) 3.5.

by the change of slope between the kernel and reflex walls. This problem is more pronounced in cases with long kernel regions, where the slope in correspondence with the circular arc endpoint tends to be pronounced

The verification can be considered passed in the case of gas with near-perfect behavior

Verification with MDM

The third phase of the verification has been conducted using MDM, an organic fluid used in ORC applications that exhibits strong non-ideal gas behavior under thermodynamic conditions applicable to real-world scenarios. This allows us to check if the code developed gives reasonable results also where the non-ideal gas effects are predominant.

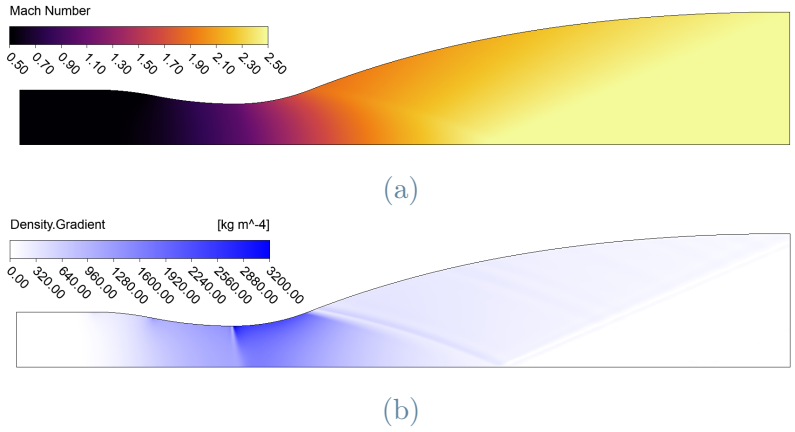

Figure 2.31: (a) Mach contour and (b) density gradient for NP non-ideal case.

Name	Fluid	T_t [°C]	P_t [bar]	Md	Z_t	source
NP	CO_2	500	200	2.5	1.03	
N1.5	MDM	263	2.69	1.5	0.92	[22]
N2	MDM	263	2.69	2	0.92	
SL1.5	MDM	239	4.59	1.5	0.82	[42]
SL2	MDM	247	4.58	2	0.81	[42]
SH1.5	MDM	268	9.2	1.5	0.65	[42]
SH2	MDM	269	9.02	2	0.63	[42]

Table 2.3: Recapitulary table of the cases used for the verification of the non-ideal MoC, with their name, total temperature (T_t), total pressure (P_t), design Mach (M_d), compressibility factor in the total state at the inlet Z_t computed using RefProp [33], and literature source. Notice that NP is the same condition used for the ideal gas case and N2 is a variation of the case presented in [22].

A first indication may be obtained by comparing the mass flow computed with the MoC with the one computed with CFD results: MoC tends to underestimate the mass flow with a greater error for cases where non-ideal gas effects are stronger, but, as reported in Table 2.4 the maximum error is equal to -0.31%, which is acceptable.

The other analysis (see Figures 2.33 and 2.34) confirms that MoC can design a shock-free nozzle while providing the design Mach number. The sonic line overlaps the one computed with CFD except for the region near the wall, but the difference is very limited. The iso-lines coincide for low Mach and tend to present a small difference near M=2. It is worth noting that this difference increases as non-ideal gas effects increase.

In summary, the planar symmetric MoC with a non-ideal gas model has been successfully verified. It has demonstrated its capability to design a shock-free divergent nozzle while

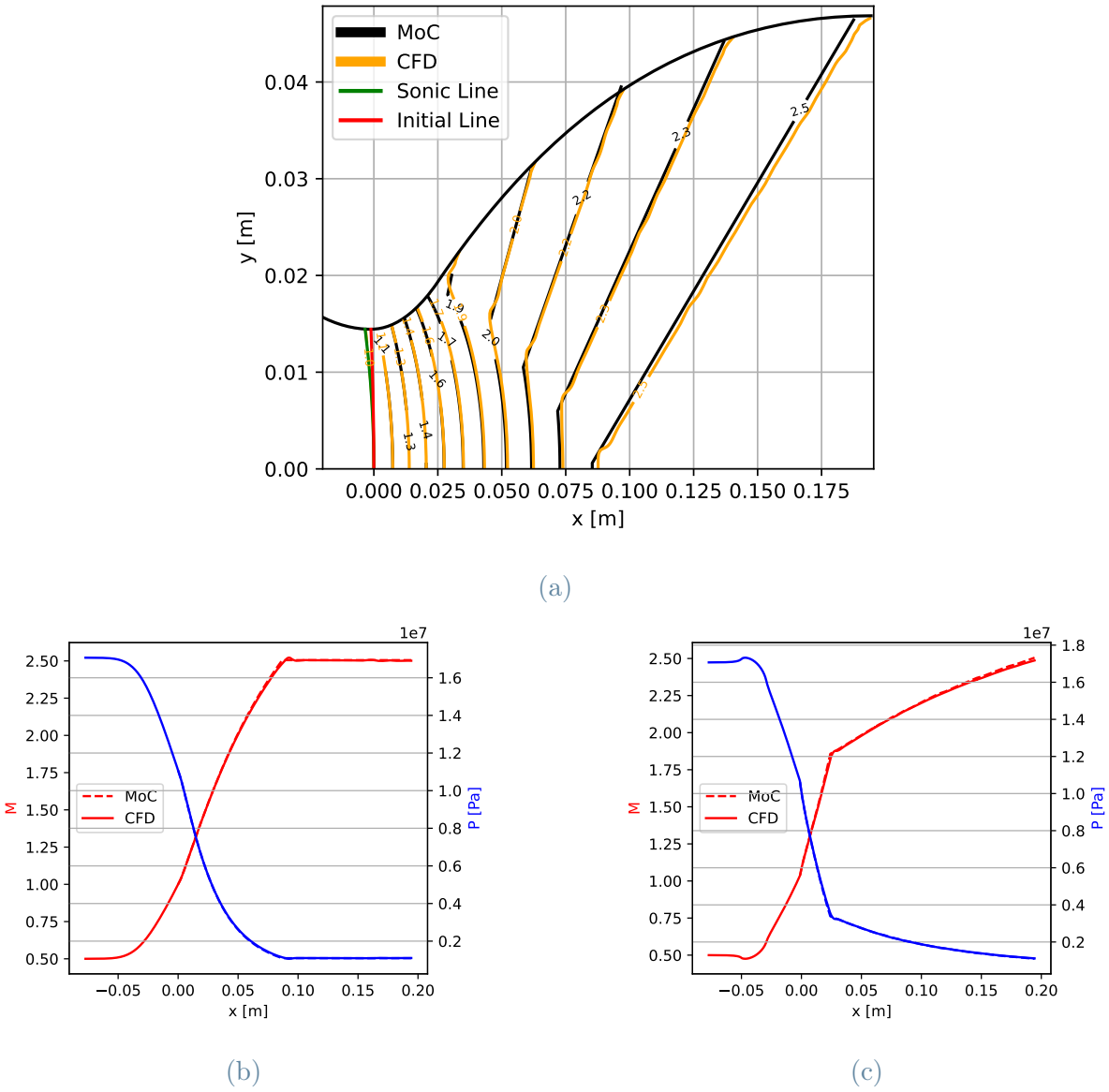

Figure 2.32: MoC-CFD comparison for (a) Mach iso-lines (b), Mach and pressure along the axis of symmetry and (c) along the wall for the NP non-ideal case.

providing the desired outlet Mach number. At the same time, the capability of the non-ideal MoC to predict with acceptable accuracy the supersonic flow inside a nozzle has been proven.

case	G_{MoC} [kg/s]	G_{Fluent} [kg/s]	err=$\frac{G_{MoC}-G_{Fluent}}{G_{MoC}}$[%]
N1.5	0.3832	0.3835	-0.1
N2	0.3832	0.3834	-0.08
SL1.5	0.6848	0.6857	-0.11
SL2	0.6759	0.6768	-0.15
SH1.5	1.3829	1.3872	-0.31
SH2	1.3506	1.3548	-0.31

Table 2.4: Mass flow computed by MoC, CFD, and the difference between the two.

2.5.7. Viscous case verification

This last part needs to answer a question that may arise: what are the effects of the presence of a boundary layer, and how does relaxing the isentropic hypothesis initially impact the results?

To answer this doubt, the nozzle of the NP case presented previously has been simulated assuming a viscous flow.

The $k-\omega-SST$ model has been initialized using a turbulence intensity equal to 3% and the hydraulic diameter of the nozzle. The presence of a $Y^+ < 5$ along the nozzle wall is proved in Figure 2.39c.

The results indicate that the design Mach is reached also in this case, see Figure 2.39a, and the iso-lines are predicted accurately. It is possible to notice also the development of the boundary layer that increases with the increase of the Mach number as expected.

If we consider Mach and pressure along the axis of symmetry, see Figure 2.39b, the region that is further from the boundary layer in a given area, the viscous nature of the fluid does not change their qualitative evolution predicted under the inviscid hypothesis. A small change in the quantitative evolution is present when the boundary layer thickness begins to increase, but with a maximum decrease of the Mach number equal to 0.4% at the nozzle outlet this effect can be considered negligible.

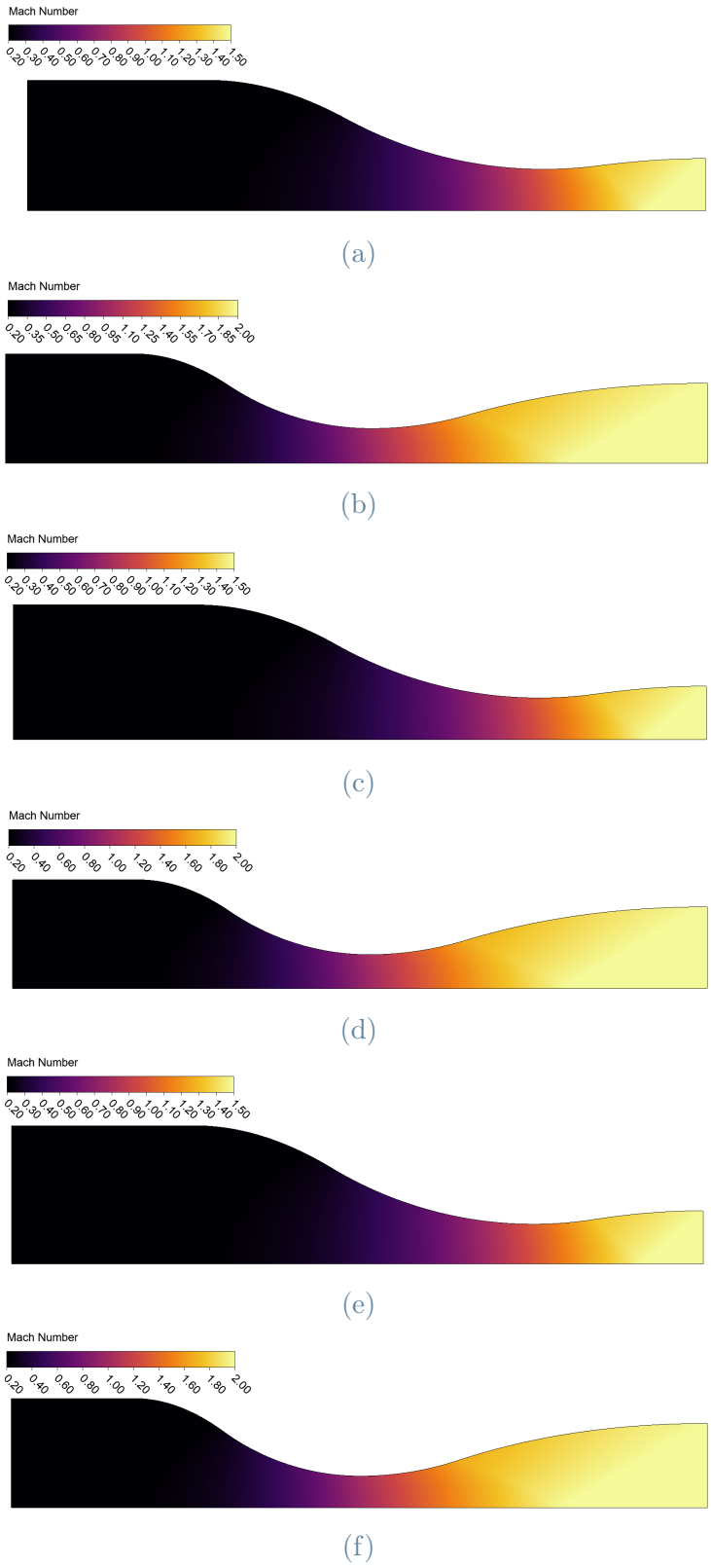

Figure 2.33: Mach contour for (a) N1.5 (b) N2 (c) SL1.5 (d) SL2 (e) SH1.5 (f) SH2 cases.

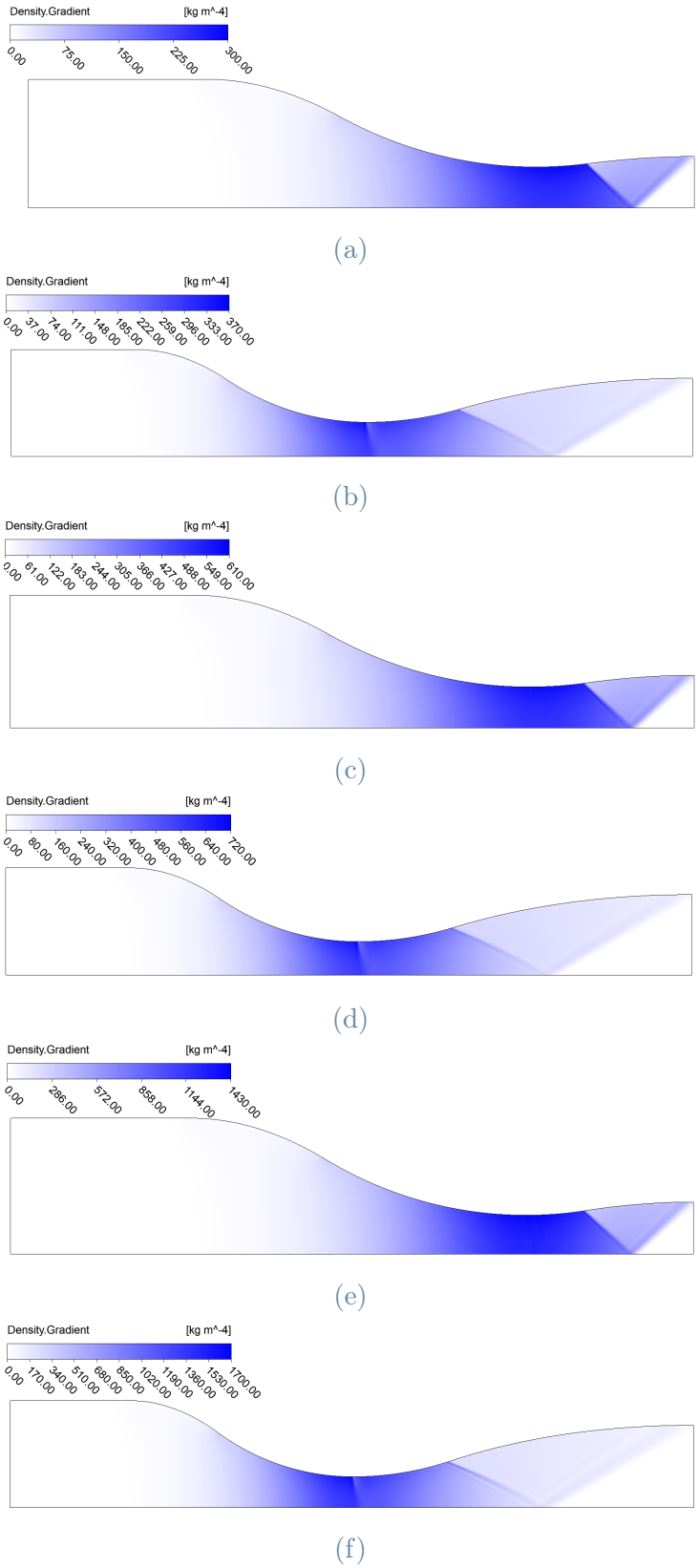

Figure 2.34: Density gradient contour for (a) N1.5 (b) N2 (c) SL1.5 (d) SL2 (e) SH1.5 (f) SH2 cases.

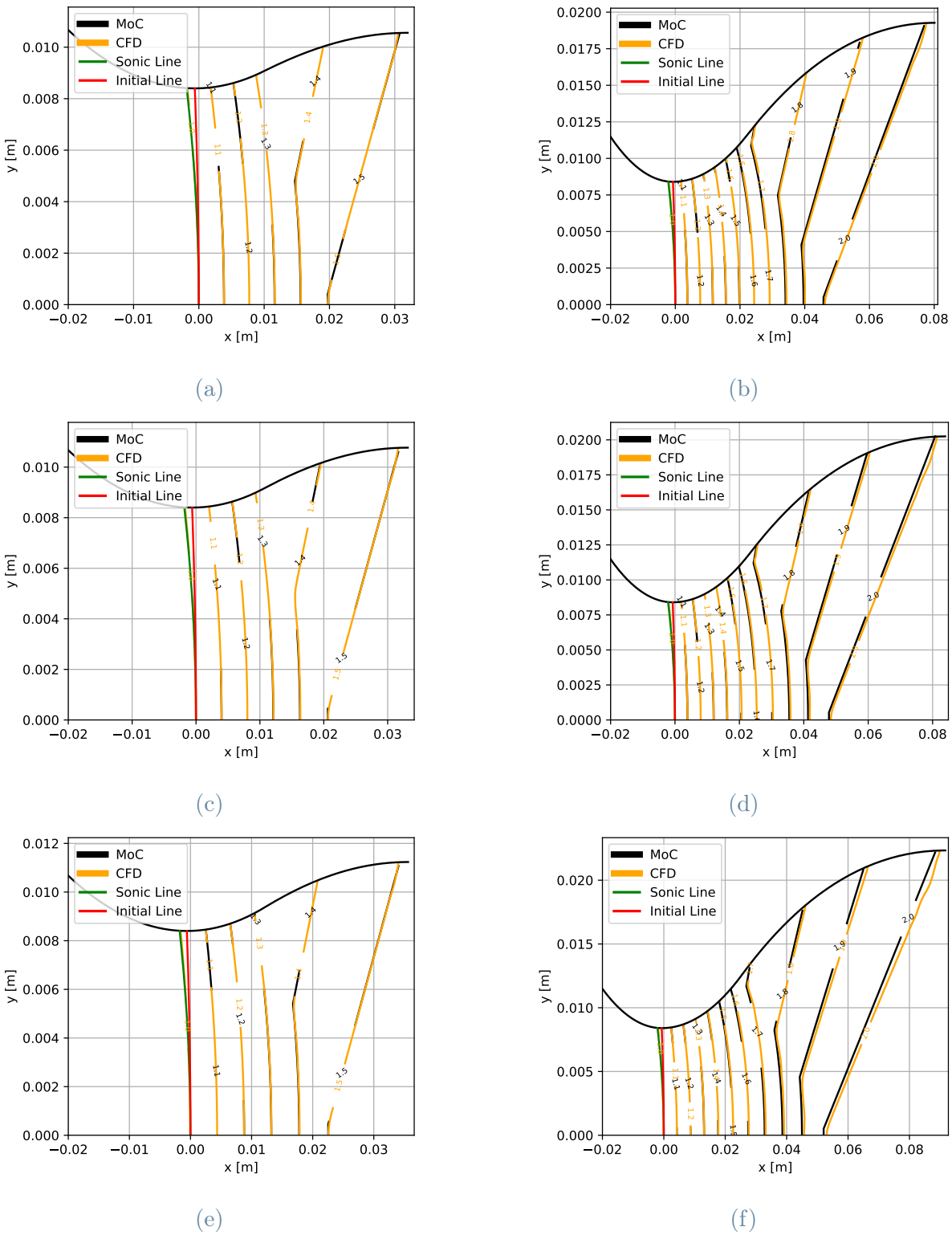

Figure 2.35: MoC-CFD comparison of Mach iso-lines for (a) N1.5 (b) N2 (c) SL1.5 (d) SL2 (e) SH1.5 (f) SH2 cases.

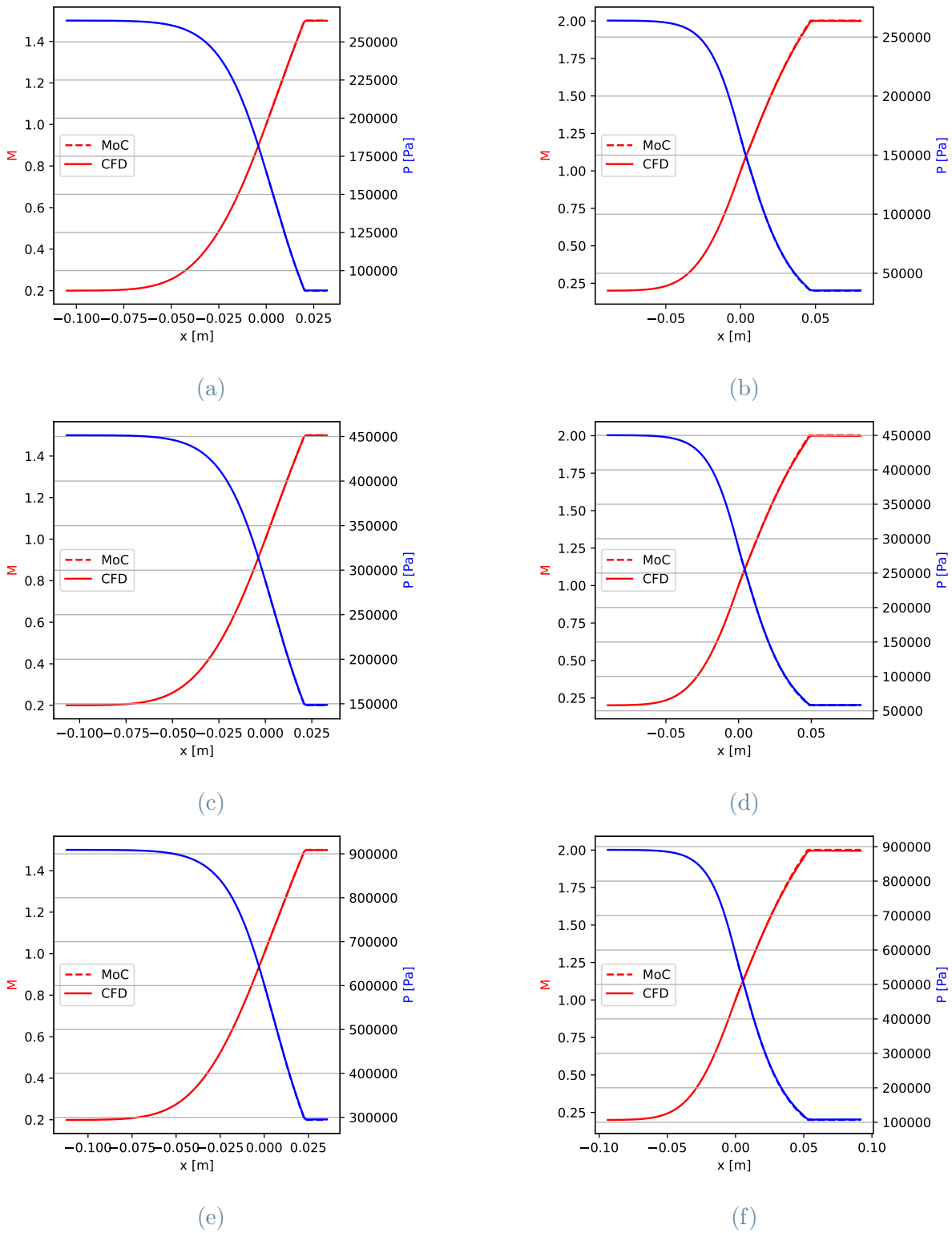

Figure 2.36: MoC-CFD comparison of Mach and pressure along axis of symmetry for (a) N1.5 (b) N2 (c) SL1.5 (d) SL2 (e) SH1.5 (f) SH2 cases.

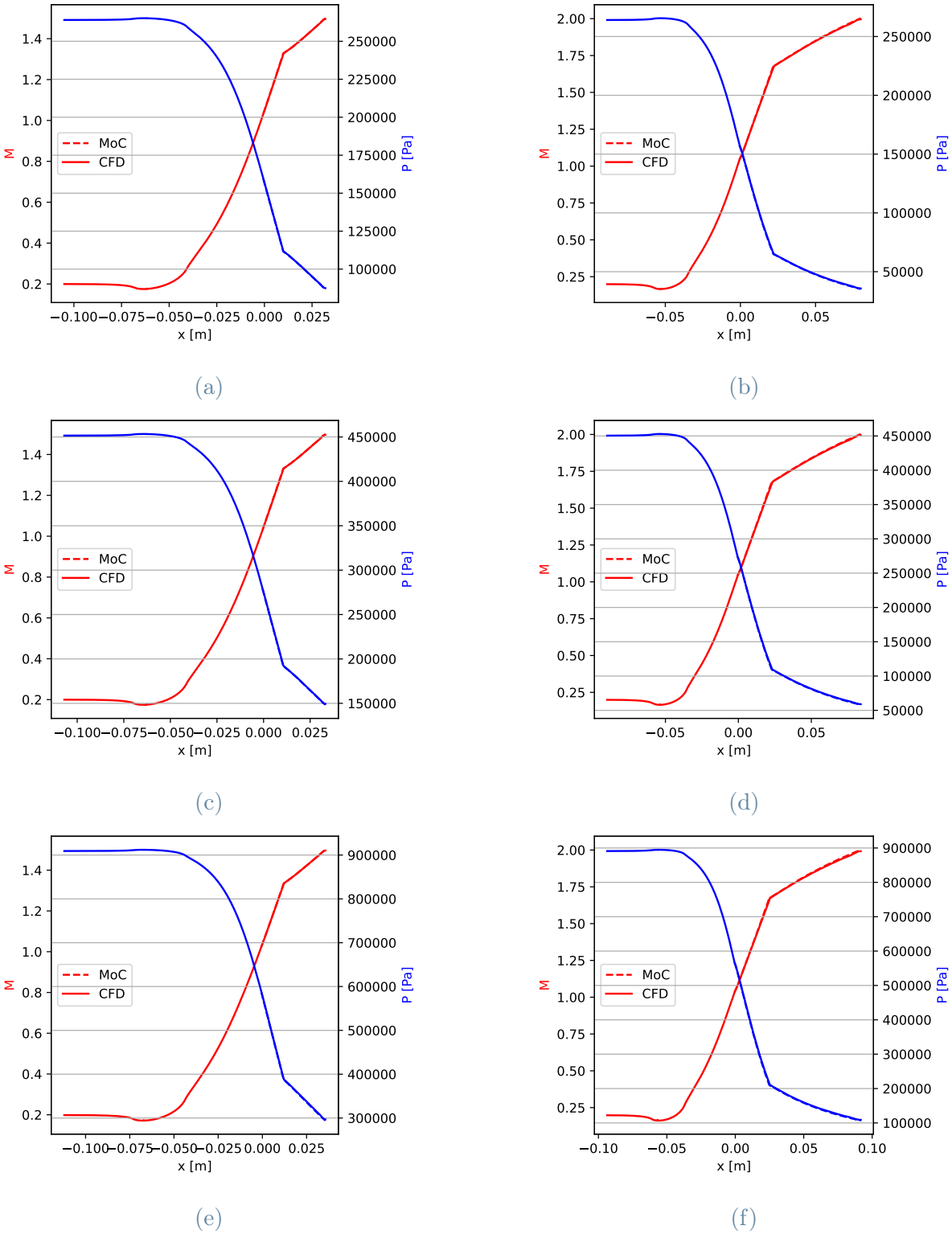

Figure 2.37: MoC-CFD comparison of Mach and pressure along nozzle wall for (a) N1.5 (b) N2 (c) SL1.5 (d) SL2 (e) SH1.5 (f) SH2 cases.

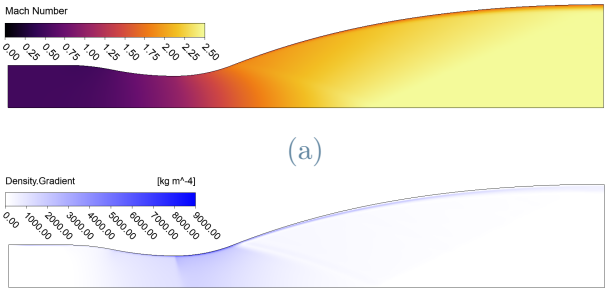

(a)

(b)

Figure 2.38: (a) Mach and (b) density gradient contour for the NP viscous case.

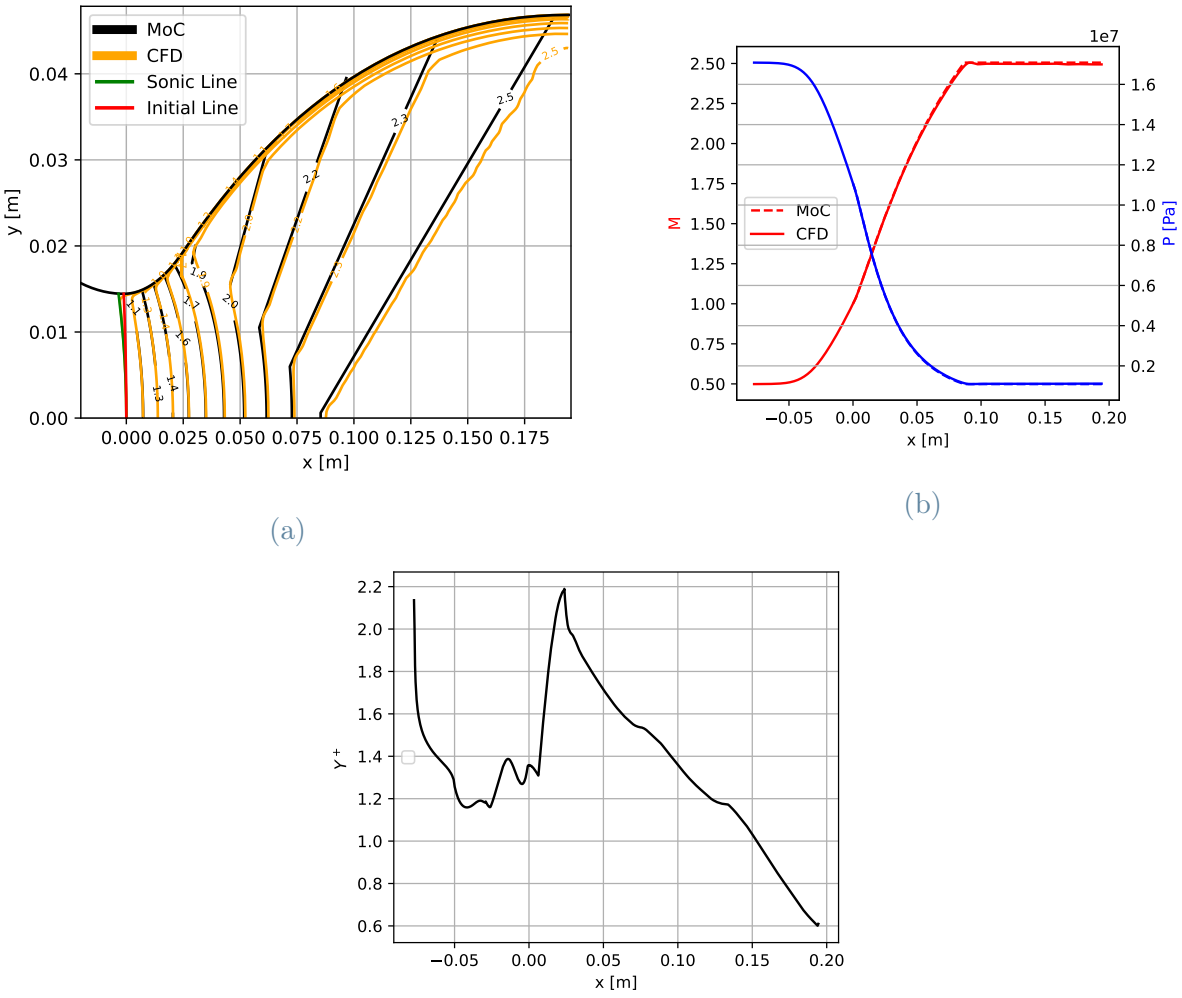

(a)

(b)

(c)

Figure 2.39: Comparison between CFD and MoC for (a) Mach iso-lines, (b) Mach and pressure along the axis of symmetry and (c) Y^+ along the wall for the NP viscous case.

3 | Asymmetric planar MoC with opposite curvature

As explained in greater detail in Chapter 4, one component of a converging-diverging turbine blade is the so-called semibladed region. This is the part of the suction side where the flow is bounded on only one side [43]. Historically, this part has been designed to connect the nozzle outlet on the suction side to the trailing edge and maintain the flow direction. Consequently, this part has been drawn as a straight line in the case of an axial turbine and a logarithmic spiral for the radial one. A new concept, developed in the last years, is to find a way to design this part in an informed manner, aiming to reduce losses.

A possible solution is to replace the traditional symmetric MoC with an asymmetric MoC, which can be employed for designing both the divergent bladed and semibladed parts. This type of MoC has been described by Savin and Syvertson [44], where it was utilized to design a wind-tunnel nozzle capable of producing two different outlet Mach numbers by translating one of the two walls. This MoC type was obtained by a symmetric MoC substituting the axis of symmetry with a prescribed curve, forming the so-called lower wall. In recent years, this MoC variant has been applied to design stator blades for both radial turbines by Zocca et al. [21] and axial turbines by Anand [2]. To be more precise, In the version of Zocca et al., the lower wall is an arc of circumference, while in the version developed by Anand, the lower wall is a straight line. Because the tests reported in both papers are only partial, further investigations could be useful

Focusing on an asymmetric nozzle with both curved walls, it can be classified into two different categories, based on the radius of curvature used to design the kernel region: concordant and opposite curvature.

In both cases, it is possible to divide the network of points into the same four regions of the symmetric nozzle: initial-value line, expansion of the initial-value line, kernel region, and reflex region. The previously mentioned classification takes into account the presence of two curves that define the domain of interest, rather than a curve and a straight line. These two curves may have the same curvature in sign, forming a concordant type nozzle

(see Figure 3.1a), or opposite curvature sign, forming an opposite curvature type nozzle (see Figure 3.1b)[22]. Notice that, for geometrical reasons, only a planar nozzle can be designed with this method.

In this work, only the planar asymmetric MoC with opposite curvature has been designed by modifying the previously verified planar symmetric MoC.

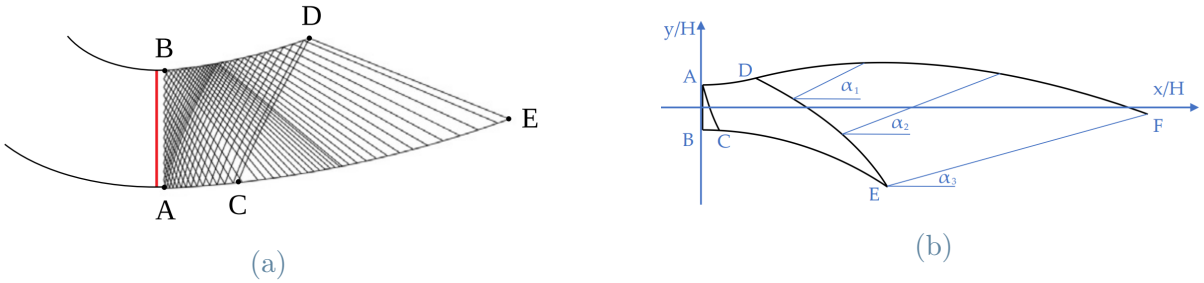

Figure 3.1: Example of planar asymmetric divergent nozzle in case of (a) concordant curvature [22] and (b) opposite curvature [21].

3.1. Main differences with the symmetric case

Compared to the planar symmetric MoC developed in the previous chapter, the new method is quite similar. The axis of symmetry has been replaced with an arc of circumference of radius R_{tL} with its center along the vertical line that passes through the throat and at a distance from the horizontal axis that guarantees a throat height equal to Y_t. The upper wall, that is the curved one in the case of symmetric MoC, is an arc of circumference of radius R_{tU}. This arc is centered with the throat along the horizontal direction and positioned vertically according to the initial choice of the reference system.

As for the symmetric case, the initial-value line has been expanded along the lower wall, and the reflex region has been attached to the upper wall, as shown in figures 3.2a and 3.1b. This implies that, as in the symmetric case, the kernel wall is much longer on the lower side compared to the upper side, where the reflex forms the majority of the total wall.

From this point on, a brief explanation of the main modifications of the code with respect to the symmetric one is provided.

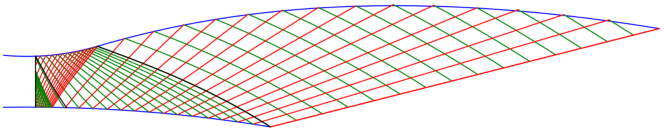

(a)

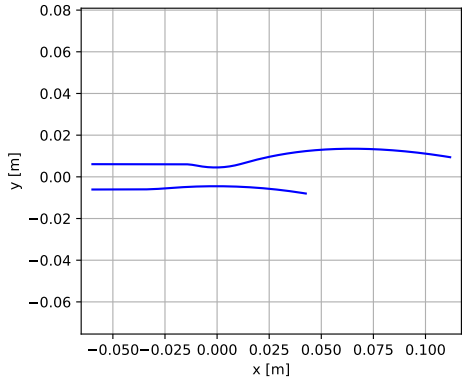

(b)

Figure 3.2: Example of (a) network of characteristics and (b) designed convergent-divergent nozzle for the planar asymmetric MoC with opposite curvature for the NP perfect case.

3.1.1. Initial line for asymmetric planar nozzle with opposite curvature

The first challenge is determining how to describe the transonic flow in the throat to define an initial-value line. To achieve this, the method presented by Zocca et al. [21], which is based on the Γ-model, has been adapted to the k-model.

Taking a step back, this method is derived from the one presented by Savin and Syvertson [44], which is a modification of the Sauer method [27] for a flow around an airfoil. The method adopts the same hypothesis and solution approach for an asymmetric nozzle with concordant curvature, as this situation can be modeled as a flow bounded by the profile itself and a streamline adjacent to it [27].

The Sauer method is modified accordingly by considering the negative half of a symmetric nozzle, where y ranges from 0 (axis of symmetry) to $-Y_t$. Then the axis of symmetry is replaced by a circular arc of radius R_{tU}, defining the total throat between these two walls.

By including a fourth power of y in the power series solution of the velocity potential equation (2.45), the velocity of the flow field in the vicinity of the throat is defined as [44]:

$$\tilde{u} = c^*(1 + u') = c^* \left(1 + \alpha x - \beta y + y^2 \left[\frac{\gamma + 1}{2} + \alpha^2 + \beta^2\right]\right) \tag{3.1}$$

$$\tilde{v} = c^* v' = c^* \left(-\beta x + xy\left[2\beta^2 + (\gamma+1)\alpha^2\right] - \left[\alpha\beta\frac{\gamma+1}{2} + 4\beta x\left(\frac{\gamma+1}{2}\alpha^2 + \beta^2\right)\right] y^2 + y^3\frac{(\gamma+1)^2}{6}\alpha^3\right) \tag{3.2}$$

where

$$\beta = \frac{1}{R_{tU}} \tag{3.3}$$

$$\alpha^2 = \frac{1}{\gamma+1}\left[\frac{1}{Y_t}\left(\frac{1}{R_{tU}} - \frac{1}{R_{tL}}\right) - \frac{1}{R_{tU}^2}\right] \tag{3.4}$$

Note that if the nozzle is symmetric ($\beta = 0$), equations from (3.1) to (3.4) are equal to those computed by Sauer and that this method only applies if $y < 0$ and $R_{tL} > R_{tU}$, ensuring the geometric production of a convergent-divergent nozzle.

The sonic line is an arc of a parabola that starts from the former axis of symmetry. In this case, the parabola goes backward with respect to the flow direction moving from the upper to the lower wall. The influence of the radius of curvature on the shape of the parabola is consistent with the Sauer method.

The method used to describe the flow in the vicinity of the throat for an asymmetric nozzle with opposite curvature and non-ideal gas model is obtained by solving, as before, the perturbation equation on the vicinity of the throat (2.84).

The flow in the vicinity of the throat is described by the equations [21]:

$$\tilde{u} = c^*(1+u') = c^*\left(1 + \lambda x + \sigma + \mu y + \bar{\Gamma}\lambda^2 y^2\right) \tag{3.5}$$

$$\tilde{v} = c^* v' = c^*\left(\mu x + \nu + 2\bar{\Gamma}\lambda(\lambda x + \sigma)y + \bar{\Gamma}\mu\lambda y^2 + \frac{2}{3}\bar{\Gamma}\lambda^3 y^3\right) \tag{3.6}$$

where the coefficients λ,σ,μ, and ν are constant and depend on the geometrical configuration of the throat region. If the throat is defined by two arcs of the circumference with radii R_{tU} and R_{tL}, where $R_{tU} < R_{tL}$, the coefficients are as follows:

$$\lambda = \sqrt{\frac{1}{2\bar{\Gamma}(y_{tU} - y_{tL})}\left(\frac{1}{R_{tU}} - \frac{1}{R_{tL}}\right)} \tag{3.7}$$

$$\mu = \frac{1}{R_{tU}} - \frac{y_{tU}}{y_{tU} - y_{tL}} \left(\frac{1}{R_{tU}} - \frac{1}{R_{tL}} \right) \tag{3.8}$$

$$\sigma = \frac{\mu^2}{4\bar{\Gamma}\lambda^2} \tag{3.9}$$

$$\xi = -\frac{2\sigma + \mu(y_{tU} + y_{tL}) + \frac{2}{3}\bar{\Gamma}\lambda^2(y_{tU}^2 + y_{tL}^2 + y_{tU}y_{tL})}{2\lambda} \tag{3.10}$$

$$\nu = -\left(\mu\xi + 2\bar{\Gamma}\lambda(\lambda\xi + \sigma)y_{tU} + \bar{\Gamma}\mu\lambda y_{tU}^2 + \frac{2}{3}\bar{\Gamma}^2\lambda^3 y_{tU}^3 \right) \tag{3.11}$$

The values of y_{tU}, y_{tL} mentioned in the previous equations are the throat height from the horizontal axis of the system of reference, as illustrated in Figure 3.3b. It is worth noting that in the original paper, σ is denominated as κ. This change of nomenclature is necessary to avoid confusion between the aforementioned coefficient and the isentropic exponent.

By comparing equations (3.5), (3.6) with equations (3.1) and (3.2), two observations can be made. Firstly, y in the model of Zocca et al. can be set more freely compared to the model of Savin et al. Secondly, the equations that describe the flow field velocity for the two different models have the same shape but different coefficients. This difference is caused by both different geometrical shapes -opposite and concordant curvature- and by the wall that has substituted the axis of symmetry to create an asymmetric nozzle. In fact, in the solution presented by Zocca et al., the former axis of symmetry is along the lower wall, while in the model of Savin et al., it is the upper wall.

As explained earlier, to create the asymmetric nozzle, the axis of symmetry has been substituted by the lower wall instead of the upper one. If we applied this method on a symmetric nozzle, where $y_{tL} = 0$, $y_{tU} = Y_t$ and $R_{tL} = \infty$, $\lambda = \alpha$, $\mu = 0$, $\sigma = 0$, $\xi = \epsilon$ and $\nu = -\left(2\bar{\Gamma}\lambda^2\xi Y_t + \frac{2}{3}\bar{\Gamma}^2\lambda^3 Y_t^3\right)$, with α and ϵ computed using (2.87) and (2.88), equations (3.5) and (3.6) are reduced to (2.85) and (2.86) respectively, under the hypothesis of planar nozzle ($\delta = 0$).

The sonic line, computed in the same way as Sauer, is an arc of parabola. In the case of $R_{tU} = R_{tL}$, as in a symmetric nozzle, its vertex is at half of the total throat height. However, if the nozzle is asymmetric, the parabola vertex is closer to the wall with a higher radius of curvature. From a geometrical point of view, this can be explained by considering that, as for a symmetric nozzle, a higher radius of curvature results in the

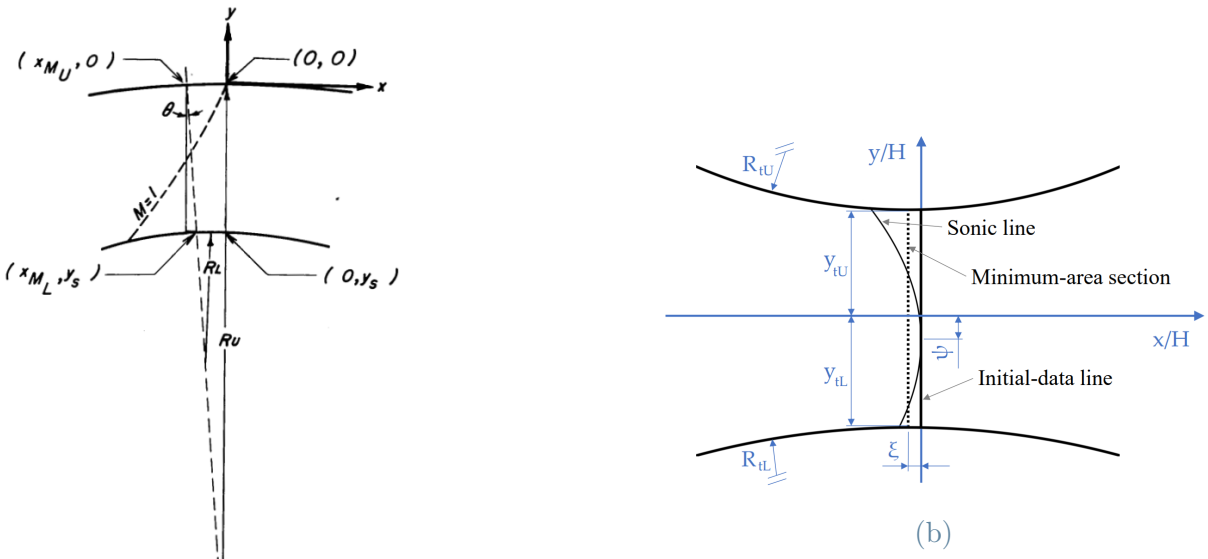

Figure 3.3: Initial-value line definition for (a) concordant [44] and (b) opposite curvature [21].

presence of a sonic curve that tends to be more similar to a straight line. Thus, the axis of symmetry of the parabola has to adjust accordingly. Consequently, the most aft axial location of the sonic line is not positioned at a constant value in the vertical direction but changes as a function of the radius of curvature of the throat walls.

The k-model is incorporated into equations from (3.5) to (3.11) by considering that $\bar{\Gamma} = \frac{\bar{\kappa}+1}{2}$, where $\bar{\kappa}$ is the isentropic exponent computed at the sonic state. This equality can be demonstrated by resolving the equation 2.90 with the method employed by Zocca et al. This is possible because $\bar{\Gamma}$ and $\bar{\kappa}$ are of the same order.

In terms of the MoC, the throat along the vertical direction has been positioned so that $y_{tU} = -y_{tL} = Y_t/2$. For the horizontal one, the zero has been positioned where the most aft axial location of the sonic line is positioned, as depicted in Figure 3.3b. The initial-value line is now a straight vertical line passing through the most aft axial location of the sonic line, ensuring that $M \geq 1$. Specifically, M=1 is true only where the sonic and initial-value lines intersect, as for the symmetric case.

The selection of this initial-value line, in agreement with [21] and [22], provides a more straightforward definition of it, paying a less precise solution of the transonic flow compared to the initial-value line selected as $\tilde{v} = 0$ in the symmetric case. This is because the straight line is further from the sonic line.

The convergent and kernel walls, as mentioned earlier, are defined as an arc of circumference, centered at a distance ξ upwind from the center of the frame of reference where the throat is positioned. They are at different vertical distances, so that $y_{tU} = -y_{tL} = Y_t/2$. It is worth noting that, for simplicity, the convergent and divergent arcs have equal radii of curvature, which differ between upper and lower walls.

3.1.2. Direct lower wall point unit

As evident, replacing the axis of symmetry with a lower wall of known equation implies that the symmetric point unit becomes obsolete and needs to be replaced with the so-called direct lower wall point unit.

This processing unit is in reality quite similar to the axis point unit. It is initialized with the information from a single point, from which a C_- is drawn. The solution point is determined where this line intersects the lower wall. To find its position and the velocity of the flow field at that point, a system of four equations with four unknowns formed by the equations (2.24) and (2.28), describing the characteristic departing from the input point and its compatibility equation, and equations (2.42) and (2.43), describing the wall function and slope, must be solved. The computation of the intersection point and local wall slope is performed in an external function separate from the processing unit, ensuring its independence from the chosen prescribed wall.

The only modification in the initial-value expansion and kernel region is the substitution of the axis point unit with the direct lower wall point unit wherever the former is employed in these two regions.

3.1.3. Reflex region modification

The modification of this computational region is quite limited and involves only how the last C_+, and thus the last point of the reflex region, is computed. In the symmetric case, since the outlet flow direction is always horizontal, the last C_+ angle with respect to the positive horizontal direction is equal to the Mach angle $\arcsin\left(\frac{1}{M_d}\right)$, where M_d is the design Mach number at the outlet.

The presence of $\theta = 0$ at the outlet may be explained by recalling that the flow must be uniform and tangential to the axis of symmetry, which is constructed horizontally. In the asymmetric case, the two wall ends indeed have the same direction to ensure a uniform outlet flow, but not necessarily a horizontal one. Therefore, the angle that the last C_+ forms with the positive horizontal direction is equal to $\theta + \arcsin\left(\frac{1}{M_d}\right)$, where θ is the

angle between the flow direction and the horizontal positive one.

The computation of the turning region follows the same algorithm used in the symmetric nozzle. It is worth noting that in Figure 3.1b the simple wave method has been used, in contrast with the method employed in this work.

Interestingly, the mass flow difference between the throat and the last C_- region is less than in the symmetric case, with a value around 0.1%. To ensure that the reflex region is computed correctly, the mass flow at the outlet of the kernel region is used as input as in the symmetric case.

3.1.4. Guarantee a reflex region made by a C^2 curve

As explained in 2.3.4, ensuring the presence of a C^2 curve as wall is fundamental to avoid the presence of shocks. While this is always true in the kernel region due to the prescribed wall, it is not guaranteed in all cases for the reflex region.

The primary issue lies not at the interface between the prescribed and computed wall but within the computed wall itself, where zones with a significantly lower number of C_+ may exist. This region with lower accuracy can lead to the presence of discontinuities in the first derivative of the computed turning contour.

To understand why this occurs we need to focus on the region where the initial-value line intersects the lower wall, called A in Figure 3.2b. If we consider the C_+ departing from this point, the presence of a Mach number near 1 causes the formation of a very steep characteristic, in contrast to the one departing from the next point on the lower wall, which has a slightly higher Mach number, resulting in a less steep characteristic. This divergence behavior is worsened by the presence of a curved wall, which introduces a larger gradient compared to the symmetric case, where the wall is straight. The distance between these two diverging characteristics increases with the number of reflections, again due to the gradients introduced by the curved walls. This phenomenon is also observed in the intersection between the initial-value line and the upper wall, near point B in Figure 3.2b. In this case, the characteristics are C_-.

To address this issue, two solutions have been developed, with the second one used if the effects of the first are not sufficient to resolve the problem.

The primary solution is to translate the initial-value line so that the Mach number of the intersection between this line and the lower wall is equal to a given value higher than 1, called $M_{initial}$. This has two effects: the increase in Mach number reduces the slope for the C_+ starting from the intersection point, mitigating the divergence, and decreases the

number of reflections for a given characteristic in the kernel region. Consequently, this reduction in reflections diminishes the dimension of the low-accuracy region.

This method has a big drawback related to how the initial-value line is defined: because it is a straight line, only one of the two Mach numbers at the line ends can be controlled. In the implemented solution presented here, the lower end (point A in 3.2b) is the one controlled because it has a lower Mach number, making it theoretically the most critical one. The information on the Mach number value is given by the radius of curvature: the lower the radius, the higher the Mach number. Thus, the sonic line tends to be more straight, bringing the initial-value line nearer to the sonic one. Another limitation is associated with the selection of the value: a trial-and-error process is necessary, although it can be done with a low number of points on the initial line, thereby limiting the added computational cost.

This solution may fail if the zone with low accuracy remains extensive, which can occur for two reasons: if the extension of the kernel region is large, the number of reflections may remain high, and if the cause of this zone is related to the characteristics departing from the upper wall.

Notice that the maximum effective value of the minimum Mach number at the lower wall is M = 1.05, which is quite close to the unitary value. This choice has been made to avoid being too far from the sonic line, where perturbation theory does not apply, and also to prevent having a Mach number that is too high near point B in Figure 3.2b.

The second implemented solution is to replace the original turning contour in the vicinity of the discontinuity, computed with the bisection algorithm, with one computed using a cubic spline interpolation of the points that composed the original curve. This approach works effectively because the computed wall follows the bisection-computed turning contour, eliminating zones where the first derivative is discontinuous. The activation of this solution is determined by a check on the second derivative: if one or more overshoots and/or undershoots are detected, the algorithm is activated.

The simultaneous use of these two corrections guarantees acceptable nozzles.

Another potential solution is to use the so-called indirect wall unit [19]. Originally developed for zones where the presence of excessively high gradients led to overly spaced points along a prescribed wall, this processing unit can be employed to reduce the dimension of these low-accuracy zones. Although this solution has not been implemented, as the previously mentioned methods provide satisfactory results with lower computational cost and in a more straightforward manner, it may be a viable option for a nozzle with a large

kernel region and/or when the trial-and-error method becomes too time-consuming.

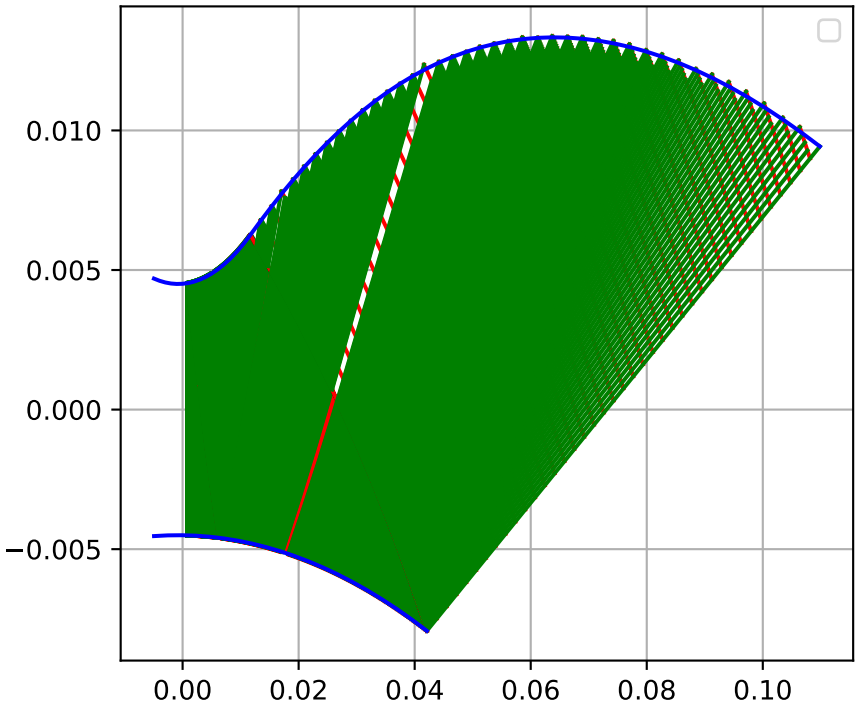

Figure 3.4: Characteristics network for the NP ideal case with all the characteristics plotted, the low accuracy zone is visible.

3.2. Verification of the asymmetric planar MoC

In this second part, the previously explained Python code has been verified through CFD simulations using the models explained in 2.4.1.

The only difference in the simulation from the symmetric case is how the mesh is constructed. Firstly, because the domain is no longer symmetric, its entire extension has been modeled. Secondly, to obtain a mesh with acceptable quality, it is necessary to have an outlet section perpendicular to the direction of the flow motion. To achieve this, a wall has been added as a straight line tangent to the end of the lower one, connecting it with the perpendicular of the end of the upper one. It is important to note that the added wall is also perpendicular to the outlet because the ends of the two walls are parallel, as explained before. This arrangement is acceptable only because the flow is inviscid. In the case of a viscous flow, the formation of a boundary layer would change the passage area distribution and thus the gas dynamics of the flow.

The order of verifications is the same as that used for the symmetric case: firstly, the

perfect case has been verified, then the non-ideal one, and lastly, if the code can model flow with increasing levels of non-ideal gas behavior.

In all the presented cases the geometry inputs are the same: the total throat height (Y_t) is 9 mm, the nozzle thickness (b) is equal to 1 mm and the radius of curvature is ten times $Y_t/2$ for the upper wall, and sixty times $Y_t/2$ for the lower one, both convergent and divergent parts are equal. The thermodynamic properties at the inlet and outlet are identical to those in Table 2.3 and the Mach number at the inlet of the nozzle is always equal to 0.5.

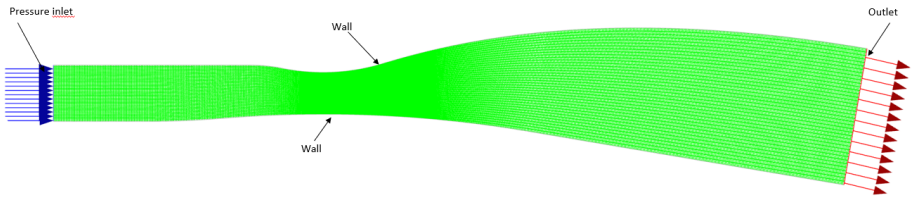

Figure 3.5:) Example of mesh used to simulate the asymmetric cases.

3.2.1. Perfect case verification

Firstly, the case called NP in table 2.3 with perfect gas is treated, assuming a molecular mass equal to 44.009 g/mol and $\gamma = 1.27$.

The mass flow value computed by the MoC is 0.3117 kg/s, with a relative difference of 0.06% compared to the value computed by CFD, which is 0.3115 kg/s.

Figures 3.6a and 3.6b demonstrate the absence of shocks and the reaching of the design Mach number at the outlet. In reality, very limited shocks may be observed at the interface between kernel and reflex region, but no effects are observed in the flow, as is possible to see in Figure 3.7a.

In this last figure it is also proven that the model presented by Zocca et al. [21] for the transonic flow in the throat agrees with the CFD simulation. Notice that in reality this model has been adapted for an ideal flow supposing that $\bar{\Gamma} = \frac{\gamma+1}{2}$, as indicated in the paper. In reality, small differences between CFD and MoC results are present near the upper wall at high Mach, especially for the last iso-line. The difference between MoC and CFD for the $M_d = 2.5$ iso-line can be attributed to the presence of the boundary condition right at the nozzle outlet.

Lastly, by observing the Mach and pressure profiles at the upper wall, it is confirmed that the small differences between CFD and MoC observed in Figure 3.7a do not affect the

Mach and pressure trends along the upper wall. Additionally, in Figure 3.7b, the zone with a constant Mach and pressure describes their values along the added wall. In reality, this zone is not part of the actual lower wall but can provide us some information about the pressure and Mach profiles at the nozzle outlet.

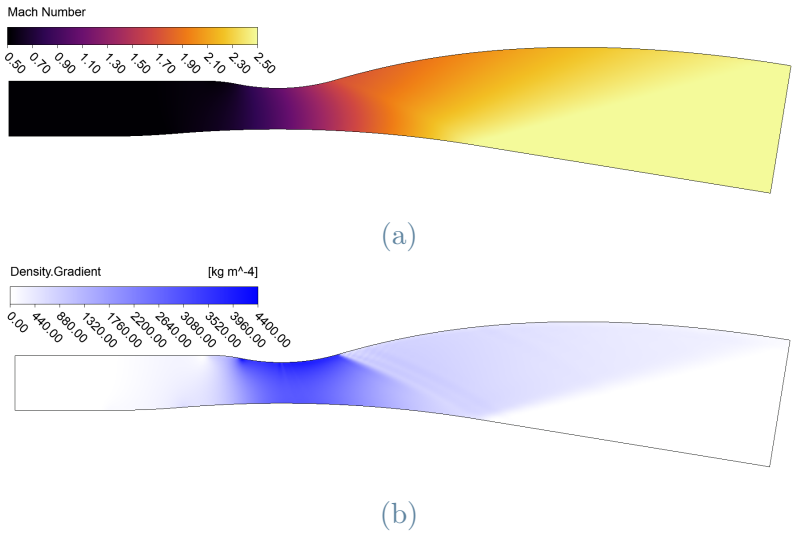

Figure 3.6: (a) Mach number contour and (b) density gradient for the asymmetric perfect NP case.

3.2.2. Non-ideal vs perfect case verification

As before, firstly, the differences between the nozzles computed with perfect and non-ideal gas models are studied for the three cases: NP1.5, NP, and NP3.5, which only differ in the outlet Mach numbers, equal to 1.5, 2.5, and 3.5, respectively.

Differently from the symmetric case, here it is possible to observe the effects of different thermodynamic models for only the kernel region (in the lower wall) and in both the kernel and reflex region (in the upper wall). The differences between the two models, summarized in Figure 3.9, and Table 3.1, are in agreement with the behavior observed in the symmetric case and are consistent with theoretical expectations.

As anticipated, the difference between the two cases increases with the outlet Mach, as the value of γ assumed initially is slightly different with the k computed in the CFD, especially in the reflex and second part of the kernel region (see Figure 3.8 for an example of that for $M_d = 2.5$). The difference at the lower wall is lower with respect to the upper wall because the effects related to a different k involve only the kernel region.

It is worth noting that the lower wall is always an arc of circumference but with higher

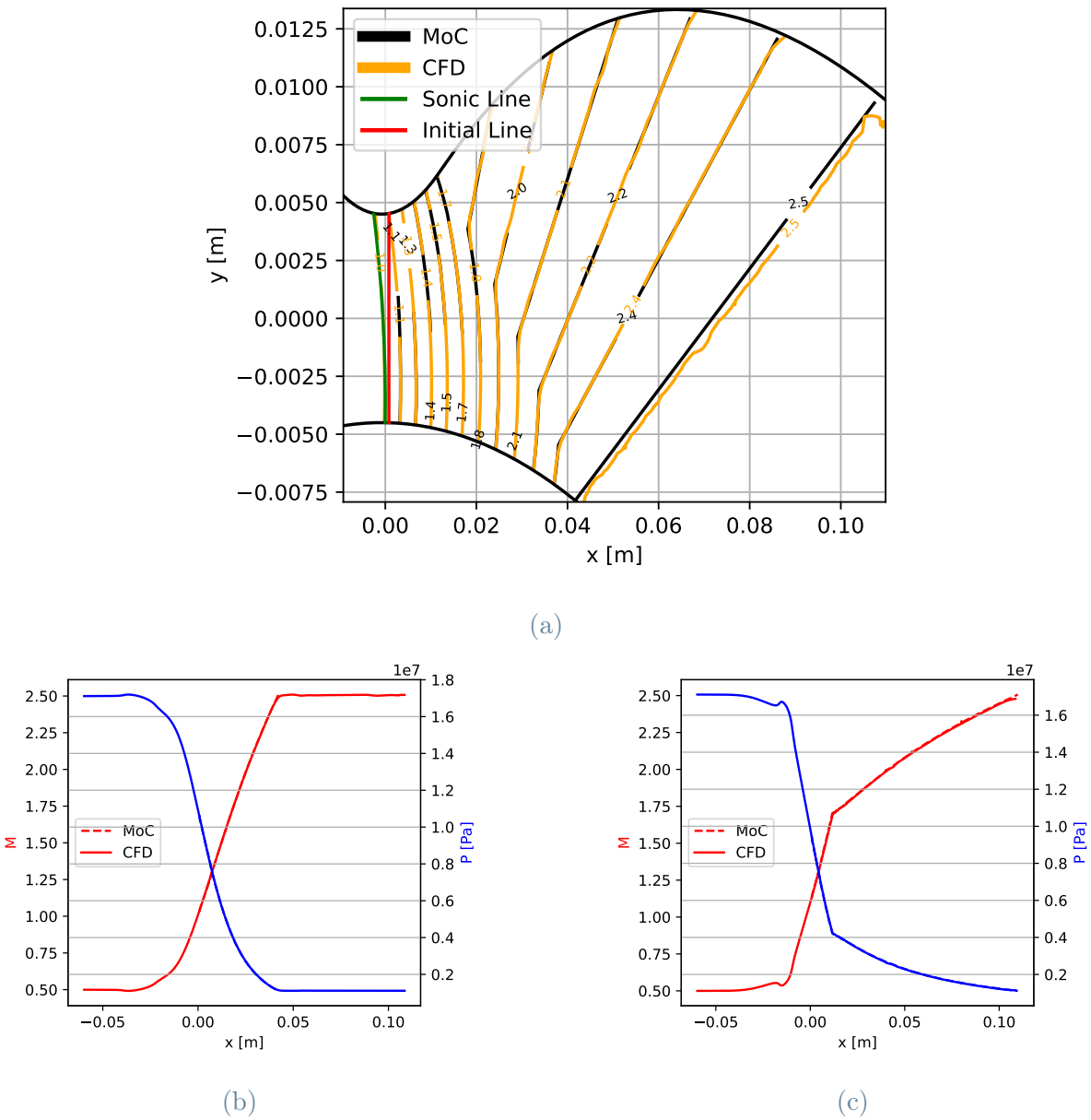

Figure 3.7: MoC-CFD comparison for (a) Mach number iso-lines, Mach and pressure along (b) the axis of symmetry and (c) the wall for the asymmetric perfect NP case.

angular extension for the non-ideal case, whereas the upper wall is a completely different curve, despite having the same shape. The difference is normalized through the axial extension of the divergent upper wall, resulting in a decrease between NP and NP3.5 for the lower wall.

Now, focusing on the comparison between CFD and MoC results for the NP case, it is evident that for the mass flow, the normalized difference between the values computed by the MoC and CFD is 0.03%. Specifically, the former is 0.3081 kg/s, while the latter is

0.308 kg/s. Similar to the symmetric case, the value computed using the non-ideal model is lower than the one calculated with the ideal one, with a relative difference of 0.9% due to the application of different thermodynamic models.

The designed nozzle is shock-free and reaches the desired Mach number at the outlet (see Figures 3.10b and 3.10a). The MoC can predict with enough accuracy the supersonic flow inside the nozzle (see Figure 3.11) with the exception of the outlet, where the effect of the boundary condition is visible.

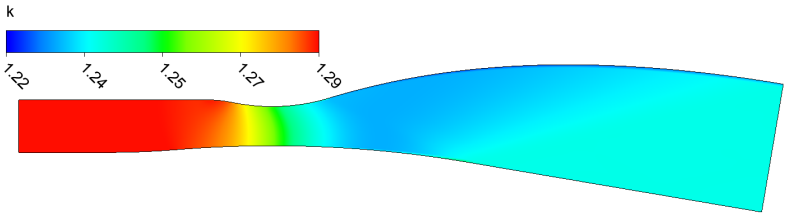

Figure 3.8: Isentropic exponent for the asymmetric non-ideal NP.

case	D_n upper wall [%]	D_n lower wall [%]
NP1.5	0.35	0.18
NP	4.41	1.41
NP3.5	8.67	0.6

Table 3.1: Differences between the end of the upper and lower wall with perfect and non-ideal gas law, computed as $\frac{l(P_{\text{end non-ideal}}, P_{\text{end perfect}})}{x_{\text{Div up}}}$, where $l(P_{end\ non-ideal}, P_{end\ perfect})$ is the distance between the non-ideal and ideal ends of one wall and $x_{Div\ up}$ is the horizontal extension of the divergent upper wall.

3.2.3. Non-ideal case verification

Testing the MoC with an increasing presence of non-ideal gas effects at the inlet demonstrates that the implemented MoC can predict supersonic flow with acceptable accuracy, without the presence of shocks. Additionally, the method used to compute the sonic line gives an acceptable description of the flow in the throat.

Regarding the mass flow, two observations may be made: the differences between CFD and MoC are consistently minimal, with the MoC tending to underestimate the mass flow. The different absolute values between symmetric and asymmetric MoC can be easily explained by the different thicknesses and throat heights. For example, in the SH2 case, the symmetric nozzle has a thickness of 18.7 mm and a total throat height of 16.8 mm, while the asymmetric one has values equal to 1 mm and 9 mm respectively.

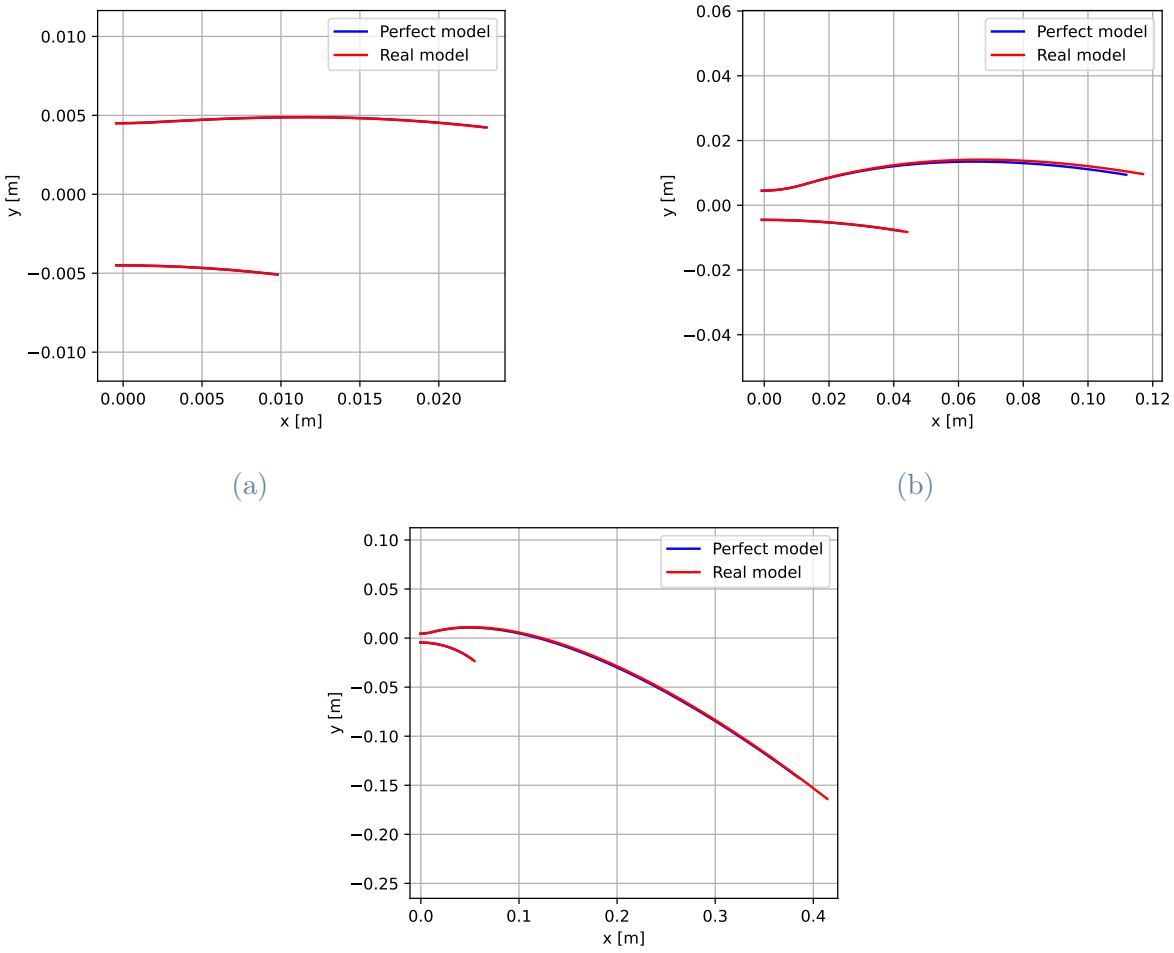

Figure 3.9: Comparison between the ideal and non-ideal asymmetric nozzles designed with NP inlet total quantities and outlet Mach equal to (a) 1.5 (b) 2.5 (c) 3.5.

Also, note that the change in the initial-value line definition has limited effects on the mass flow computation. For instance, considering the same case as before and computing the mass flow using the geometrical quantities of the symmetric nozzle, we have $G_{symm} = 1.3506$ kg/s and $G_{asymm} = 1.3508$ kg/s, with the second having $R_{tU} = R_{tL} = R_{\text{conv symm}}$. If we consider $R_{tU} = 10Y_t/2$ and $R_{tL} = -60Y_t/2$, G_{asyymm} becomes equal to 1.3513 kg/s. This is slightly higher because the change in the radius of curvature causes the change in the relative distance between the straight initial-value line and the parabolic sonic line, thus affecting the flow velocity. The same effect is also present if the $M_{initial}$ is increased beyond the Mach number in A of Figure 3.1b.

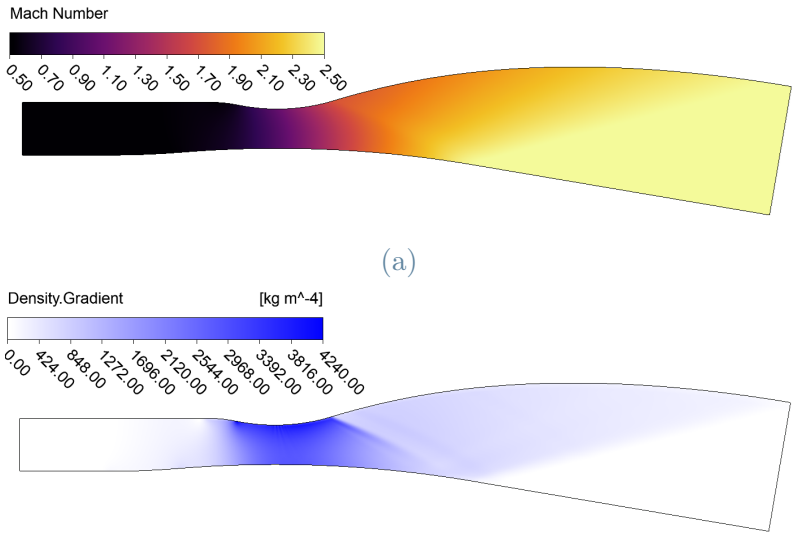

Figure 3.10: (a) Mach contour and (b) density gradient for asymmetric non-ideal NP case.

case	G_{MoC} [kg/s]	G_{Fluent} [kg/s]	err=$\frac{G_{MoC}-G_{Fluent}}{G_{MoC}}$[%]
N1.5	0.010977	0.010982	-0.05
N2	0.010977	0.01098	-0.05
SL1.5	0.01963	0.01964	-0.05
SL2	0.01936	0.01939	-0.15
SH1.5	0.03971	0.03972	-0.03
SH2	0.03873	0.03881	-0.21

Table 3.2: Mass flow computed by MoC, CFD, and the difference between the two for asymmetric nozzles.

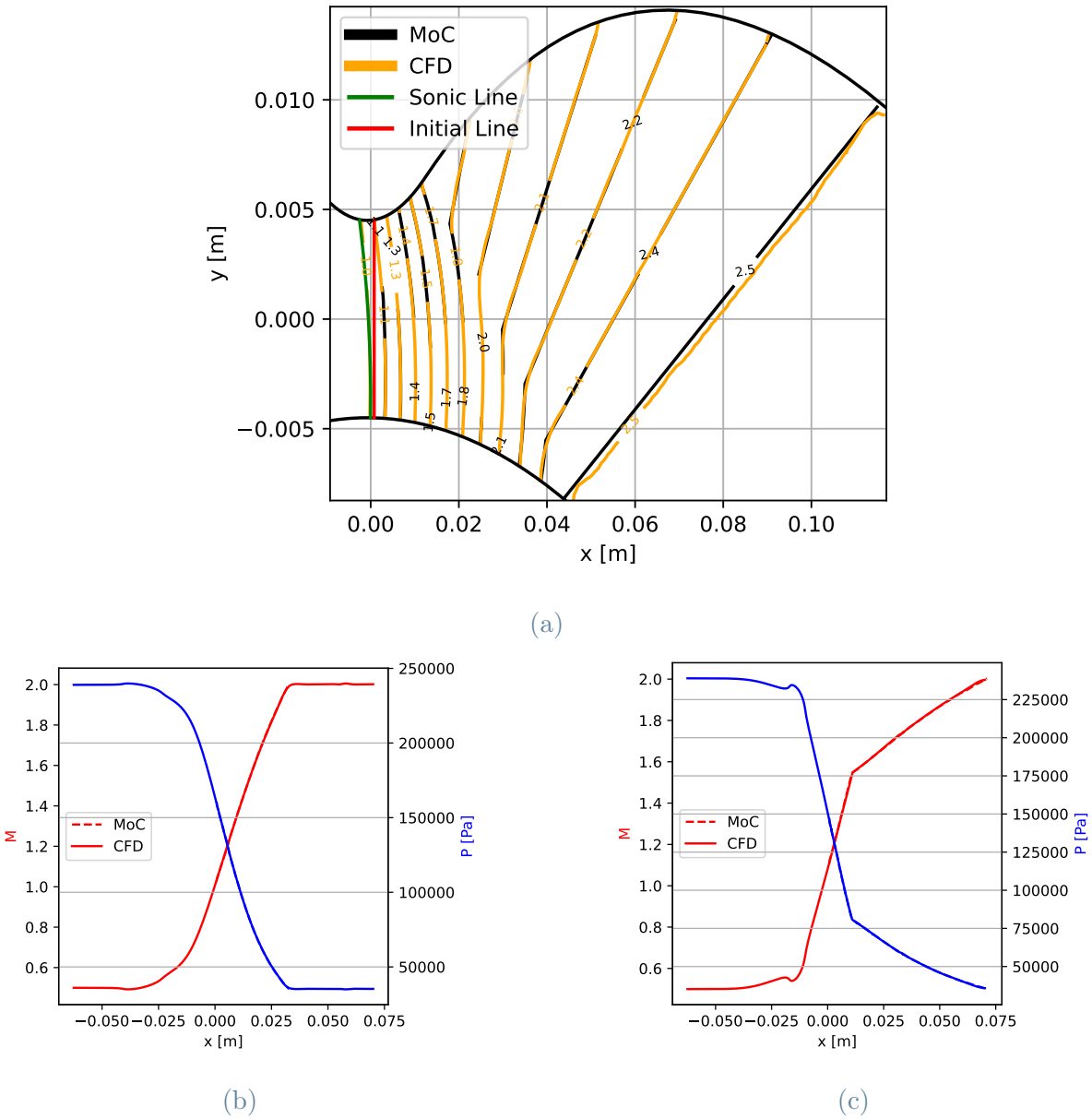

(a)

(b)

(c)

Figure 3.11: MoC-CFD comparison of (a) Mach iso-lines, (b) Mach and pressure along the axis of symmetry and (c) along the wall for the asymmetric non-ideal NP case.

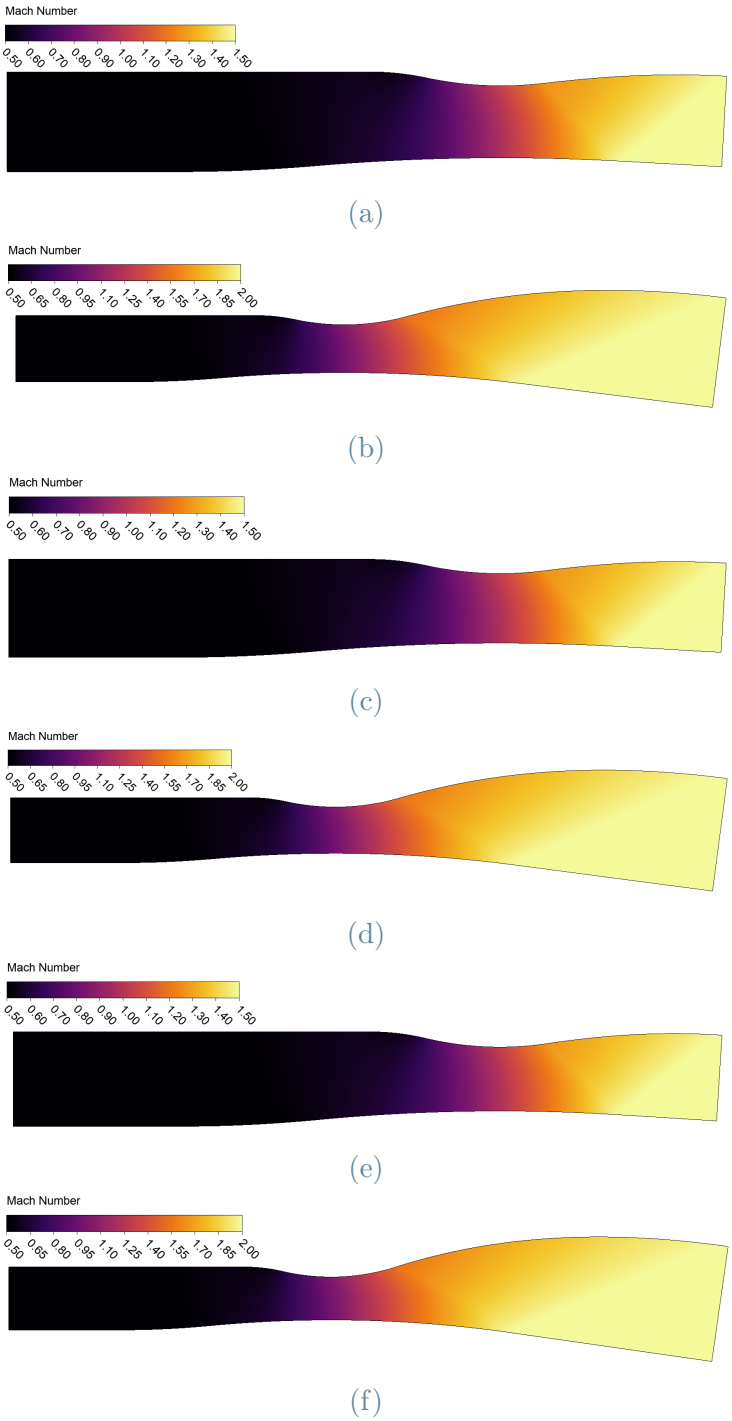

Figure 3.12: Mach contour for (a) N1.5 (b) N2 (c) SL1.5 (d) SL2 (e) SH1.5 (f) SH2 asymmetric cases.

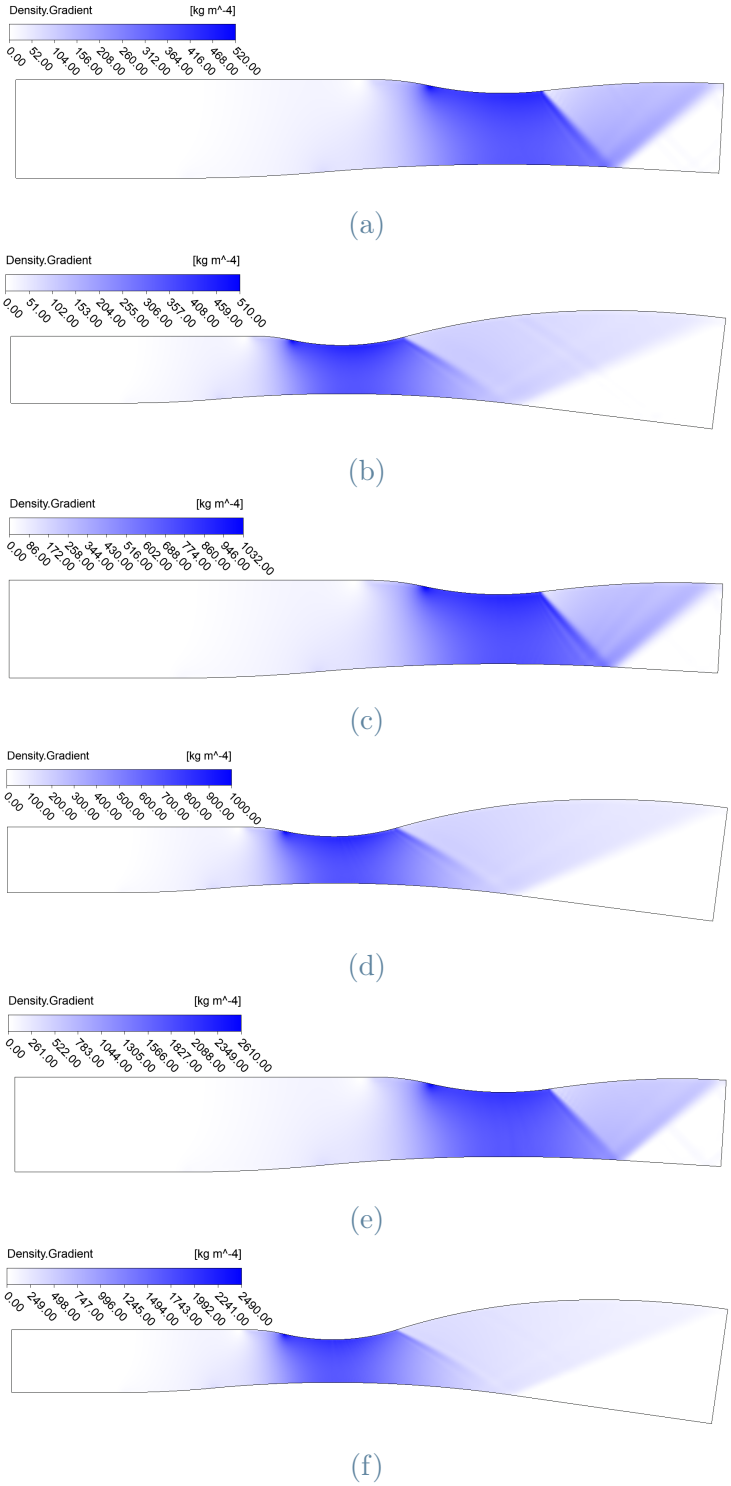

Figure 3.13: Density gradient contour for (a) N1.5 (b) N2 (c) SL1.5 (d) SL2 (e) SH1.5 (f) SH2 asymmetric cases.

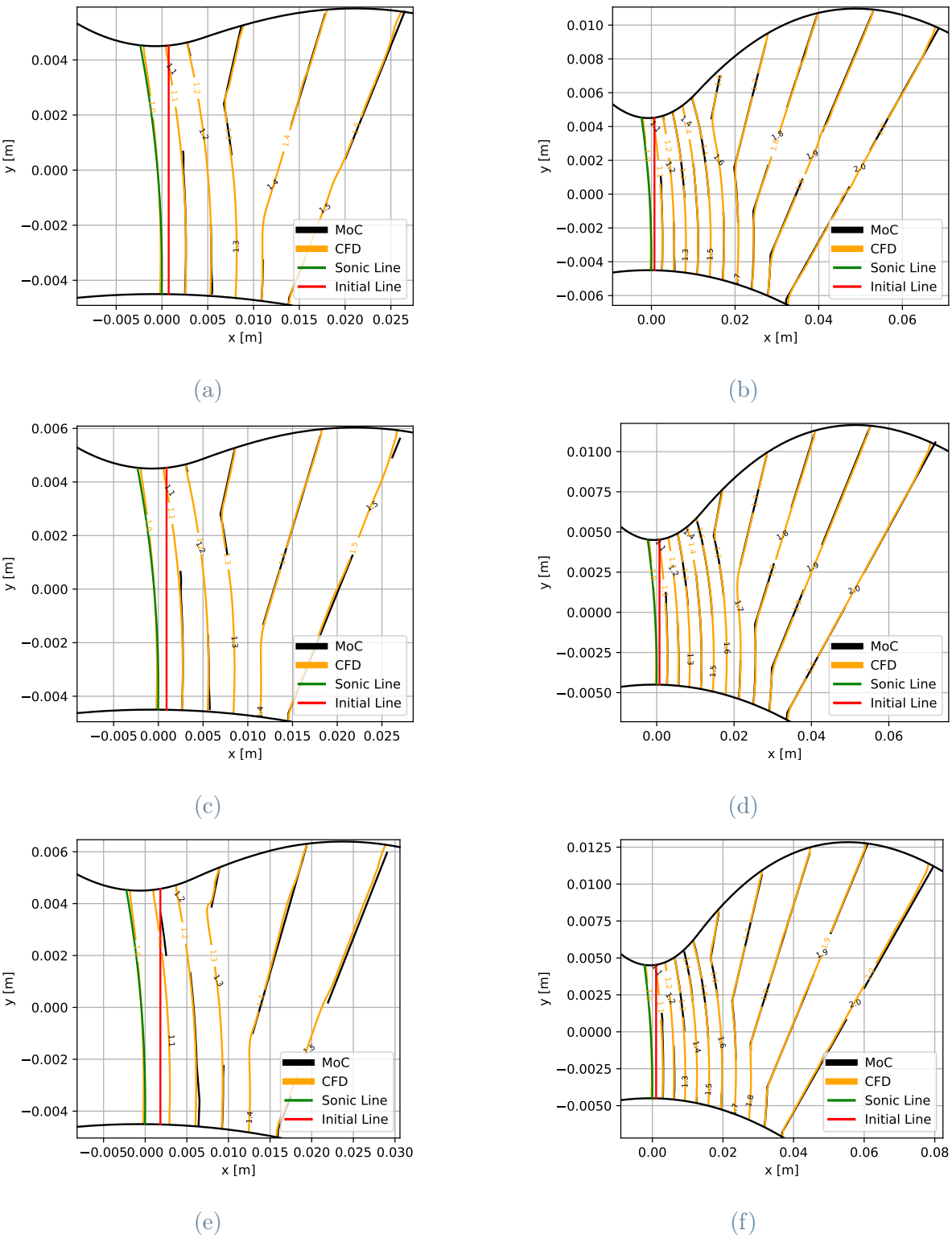

Figure 3.14: MoC vs CFD comparison of Mach iso-lines for (a) N1.5 (b) N2 (c) SL1.5 (d) SL2 (e) SH1.5 (f) SH2 asymmetric cases.

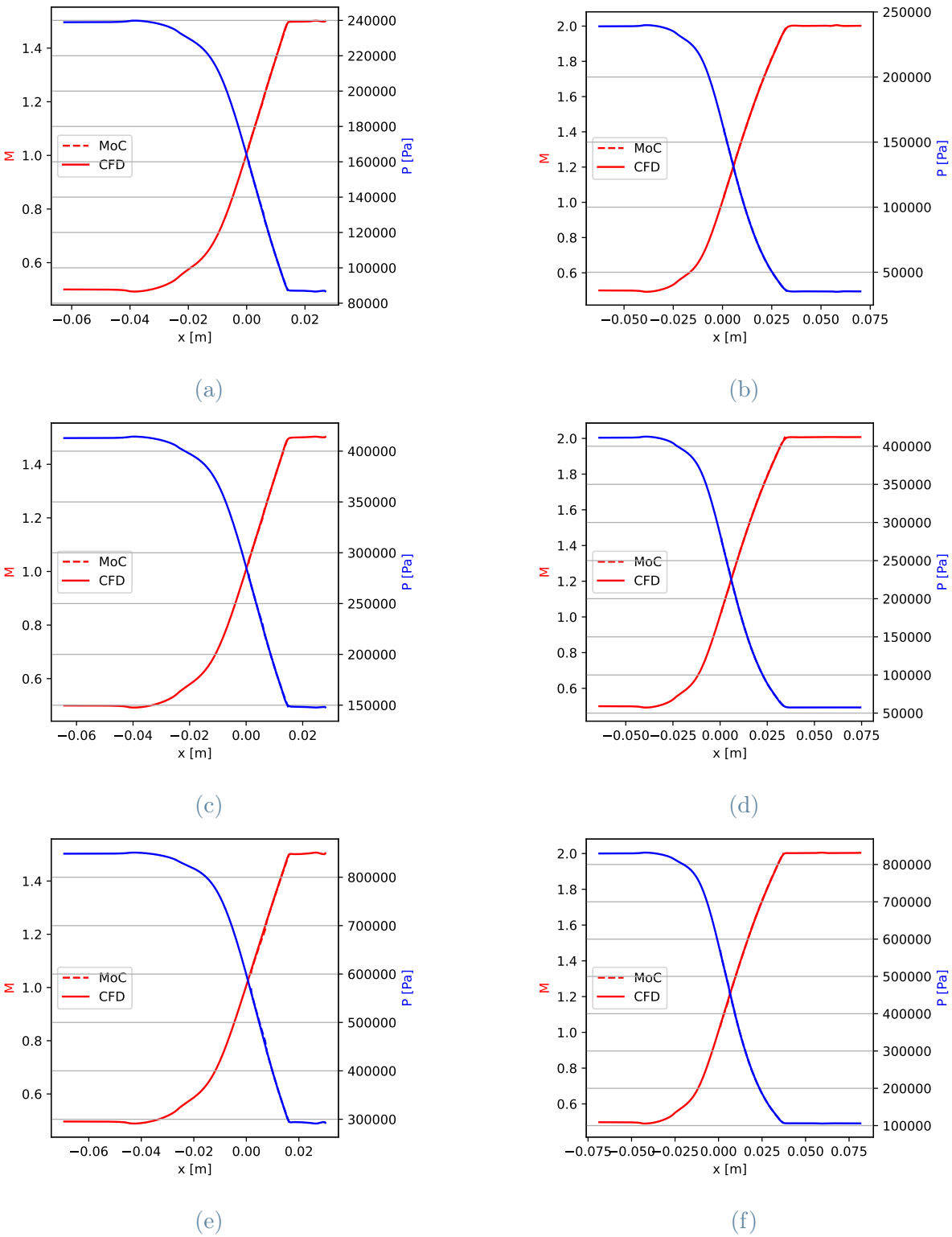

Figure 3.15: MoC vs CFD comparison of Mach and pressure along the axis of symmetry for (a) N1.5 (b) N2 (c) SL1.5 (d) SL2 (e) SH1.5 (f) SH2 asymmetric cases.

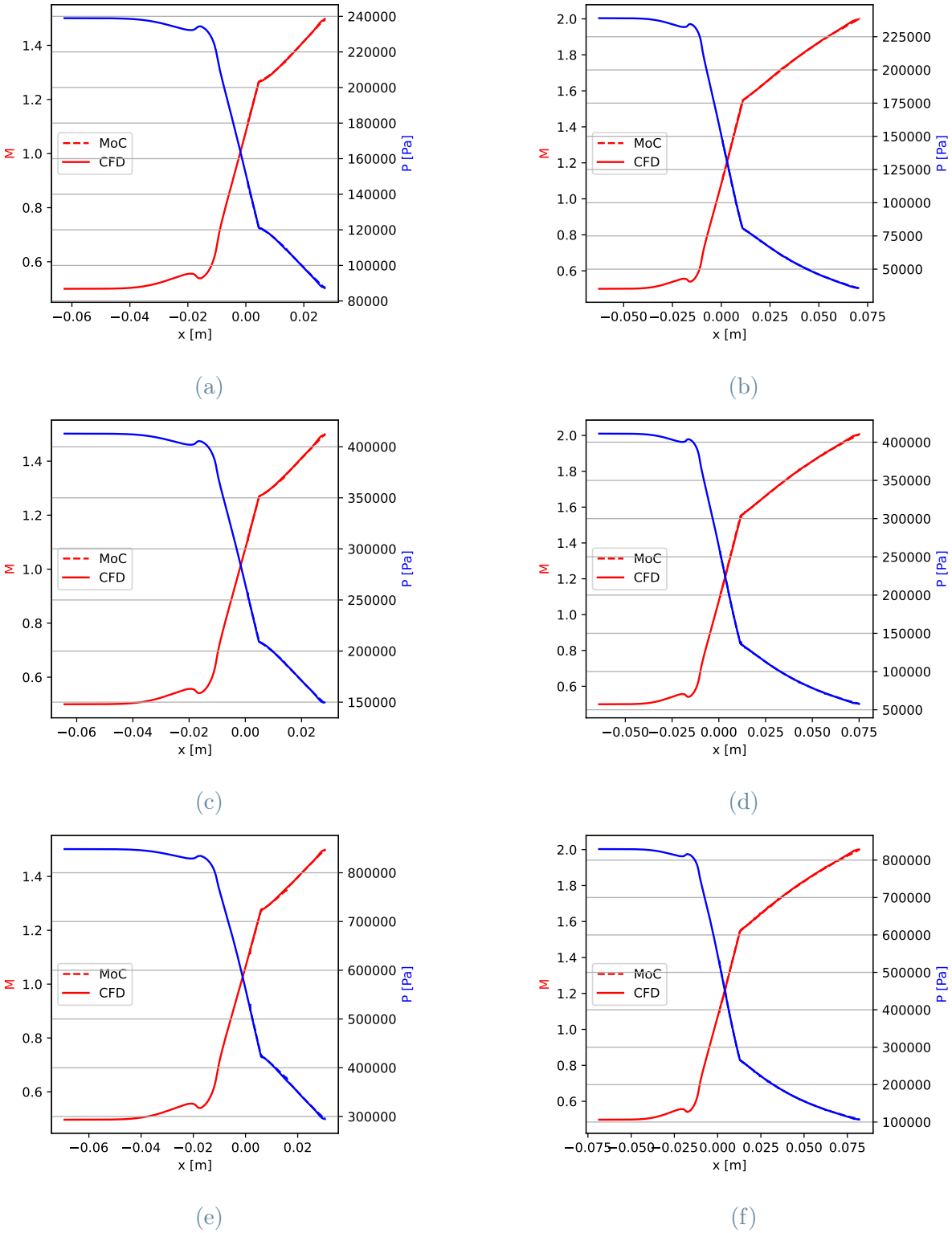

Figure 3.16: MoC vs CFD comparison of Mach and pressure along the nozzle wall for (a) N1.5 (b) N2 (c) SL1.5 (d) SL2 (e) SH1.5 (f) SH2 asymmetric cases.

4 | Example of MoC application: design of a convergent-divergent stator blade

One of the main examples of the MoC application, aside from the straightforward design of a supersonic nozzle, is the design of a converging-diverging turbine vane that accelerates the flow from subsonic to supersonic conditions. This example can be seen as a benchmark for the implemented MoCs.

4.1. Design of a convergent-divergent stator for axial turbine with a symmetric MoC

Generally speaking, in the case of subsonic flow, the design of a turbine stator blade is not as critical. This is because the expansion, and consequently a flow from a high-pressure region to a low-pressure one, tends to ensure the stability of the boundary layer, assuming a continuous and gradual decrease in the passage area [45]. In contrast, when dealing with supersonic flow, the possibility of shocks—something that needs to be avoided for acceptable efficiency—makes the design of a profile critical. Therefore, a precise procedure must be implemented.

To describe this procedure is important to introduce the three main parts into which a converging-diverging vane [13, 26, 43, 46]:

- **Converging section**. This first part is responsible for the shaping of the leading edge and suction and pressure side of the blade before the throat. The main goal is to accelerate the flow to transonic conditions and deflect it until the exit metal angle is achieved. Because the flow is subsonic, this section is not highly critical in the initial design, allowing for the utilization of various drawing methods, such as

C^2 continuous NURBs curve [2], spline curves [13] and profiles employed in subsonic turbines [16]. In all cases, it is important to keep the curvature under control to avoid flow detachment, especially near the throat. Another thing to avoid is overspeed that, if present, can cause the formation of a supersonic flow, possible shocks, and severe pressure gradients that have negative effects on the boundary layer at the suction side [20].

- **Diverging section**. This section starts from the throat and is designed using a MoC. The resultant nozzle has to be adapted through a series of geometrical transformations, like scaling, translation, and rotation, before being connected to the rest of the blade. It is important to notice that the MoC is only able to design nozzles, and so cannot draw a profile able to deflect a flow. For this reason, the necessary deflection must be done in the converging section.
- **Semibladed or semivaned section**. Due to the geometry of a cascade, after the diverging part, there exists a region where the solid wall is present only on one side. This part is present only on the suction side and has the goal of connecting, through a solid wall, the end of the divergent section of the suction side with the trailing edge. This wall is usually designed as a straight line tangent to the divergent section end so that the metal angle is conserved. It is important to remember that in this section the flow is supersonic so possible shocks may be present.

4.1.1. MoC hypothesis validity in a turbine stator cascade

A topic of interest could be whether the hypothesis under which the MoC is resolved is true or not for a real cascade. To briefly recall them, the MoC is valid under the hypothesis of a steady, two-dimensional, irrotational, supersonic flow.

The assumption under which the flow is supersonic is always true and, if the transient phase is already passed, also steady.

Attaining a flow characterized by constant total enthalpy and entropy is virtually impossible. In practice, the former can be considered true because, for definition, a stator does not exchange work and a cascade can be considered as adiabatic. However, the presence of an isentropic flow is unattainable. Even when considering a shock-free flow inside the divergent blade channel, which is the part designed by the MoC, a boundary layer is still present.

This problem has already been analyzed in the case of a nozzle, as discussed in Section 2.5.7. The analysis demonstrates that the development of a boundary layer is not a

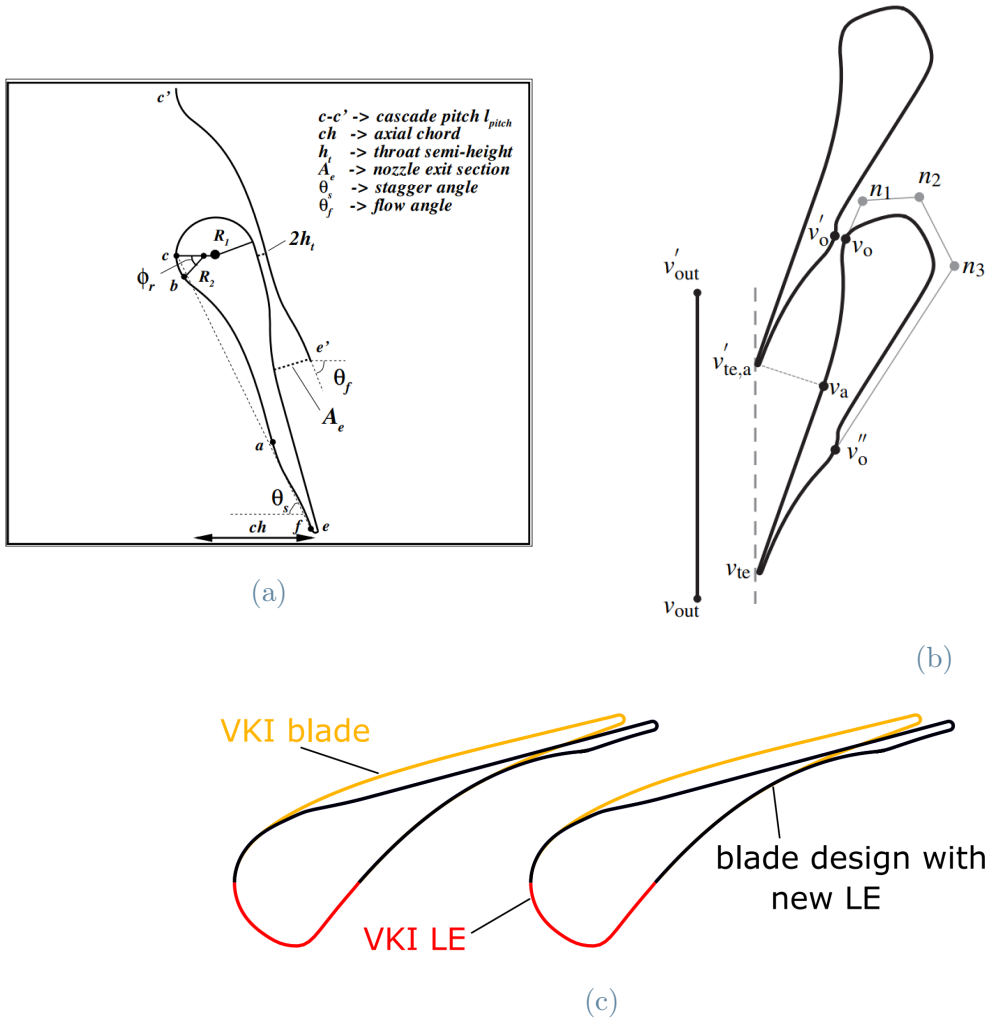

Figure 4.1: Symmetric axial turbine blade constructed with different methods. By considering how the convergent part is draw: (a) spline curves [13], (b) C^2 continuous NURBs curve [2] and (c) profiles already used in subsonic turbines [16].

critical problem. However, the situation may change for a stator blade: the reduction of the passage areas may cause a lower outlet Mach number compared to the design value, resulting in a lower pressure ratio, and a slightly reduced mass flow [13]. Both these factors, together with the increase in entropy production, contribute to a decrease in the power output of a turbine.

To resolve this problem, one approach could be to predict the development of the boundary layer as a function of the pressure distribution, and then correct the wall designed by the MoC to account for its presence. An example of such a study has been carried out by Bufi [13], who developed a model for boundary layer development under a pressure distribution based on the approximate model of Reshotko and Tucker [47].

The presence of irrotational flow, where $\nabla \times V = 0$, is always true for a nozzle with inlet flow parallel to the main direction of it and, at least in theory, inside the blade passage of a stator [45]. However, this hypothesis is not valid if vorticity is formed inside the channel, for example, due to flow separation, or the inlet flow is already not irrotational, as may occur after a combustor where vortical structure may be induced to guarantee an efficient combustion, or after a rotor. In a single-stage ORC turbine, where no combustor is present, this hypothesis may be considered satisfied.

Lastly, the flow in turbomachinery is indeed strongly three-dimensional [45]. However, because the goal of this work is to design a two-dimensional profile, and not a three-dimensional blade, it is acceptable to study the flow in a blade-to-blade plane, where the flow is two-dimensional.

This approach does not take into consideration the fact that the flow along a blade-to-blade surface is not independent from the other planes, due to radial equilibrium and other possible three-dimensional effects.

4.1.2. Construction of the blade

Here is a description of the main steps of the method used to design an axial turbine vane with symmetric MoC. This method is based on the approach presented by Anand et al. [43] with limited modifications.

The main inputs are:

- A nozzle designed by a symmetric MoC, that may be computed in the same algorithm or imported.
- Geometrical information: metal outlet angle φ_a, pitch p and thickness of the trailing edge t_{TE}.

The procedure starting from the nozzle obtained with the MoC is as follows:

1. If not already done, the nozzle is translated along the horizontal axis so that the throat is at $x = 0$ and is normalized with the throat height Y_t. Thus, the throat is at $y = 0.5$ for the upper wall and $y = -0.5$ for the lower one, and the exit area A_{is} is only a function of M_d;
2. **Construction of the semi-bladed section**.
    - With reference to Figure 4.2a, points ss^*_{te} and ss_{te} are positioned so that ss^*_{te} is on the center of the frame of reference at (0,0), and ss_{te} at vertical distance p from the former.

- The point ss_a is obtained by the intersection of two straight lines: one departing from ss^*_{te} with angle $90 - \varphi_a$ and the second originating from ss_{te} with angle φ_a. The line ss_{te}-ss_a, representing the semi-bladed section, is drawn.

3. **Trailing edge construction**.

   - The point ps^*_a is drawn at distance t_{TE} from ss^*_{te} along the ss^*_{te}-ss_a straight line.
   - The point ps_a is then positioned at a distance p from ps^*_a along the vertical direction.
   - The trailing edge is drawn as a circumferential arc of radius $t_{TE}/2$ that connects ss_{te} and ps_a. Its center is in the midpoint of the ss_{te}-ps_a straight line;

4. **Scaling and transformation of the nozzle geometry**.

   - The nozzle obtained by the MoC is scaled by a factor

   $$L = \frac{l(ss_a, ps^*_a)}{A_{is}(M_d)} \tag{4.1}$$

   ensuring that the exit area of the diverging nozzle is equal to the distance between ss_a and ps^*_a.
   - After scaling, the nozzle is rotated by an angle φ_a about the center of the throat. The obtained geometry forms the diverging section of the vane by shifting it so that the ends of the walls are coincident to ss_a and ps^*_a.

5. **Translation of the pressure side**.

   - The pressure side obtained previously is now shifted by a quantity p along the vertical direction thus its end is coincident with ps_a and a continuous line is drawn connecting the pressure and suction side.

6. **Converging section**.

   - Unlike the method of Anand et al., the converging section is formed by two arcs of circumference and a continuous NURBs curve, implemented in Python using the package presented in [48].
   - Starting from the throat of the pressure side and defining k the radius of curvature of the kernel region, an arc of the circumference is drawn connecting the points C_1 with ps_o and another connecting C_7 with ss_o, see Figure 4.2d. The NURBs curve is then computed using the control points from C_1 to C_7 in

Figure 4.3a. Notice that the points C^* and C^{**} are along the tangent of C_1 and C_7 respectively at a distance$k/3$.

- The distance between C_2 and ss_a and the distance of $C_3 - C_6$ from O_c are not equal to $2k$ and $1.25k$, but at $CoeffSS * k$ and $CoeffConv * k$ that are changed to adapt the shape of the convergent part.

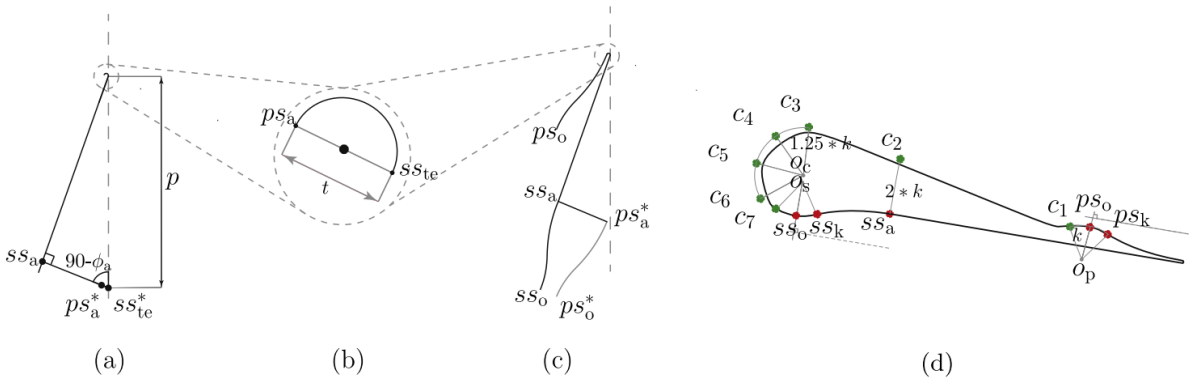

Figure 4.2: Schematic representation of the procedure used to design the blade of an axial supersonic vane, (a) semi-bladed section, (b) trailing edge (c) diverging-nozzle section, and (d) converging section.

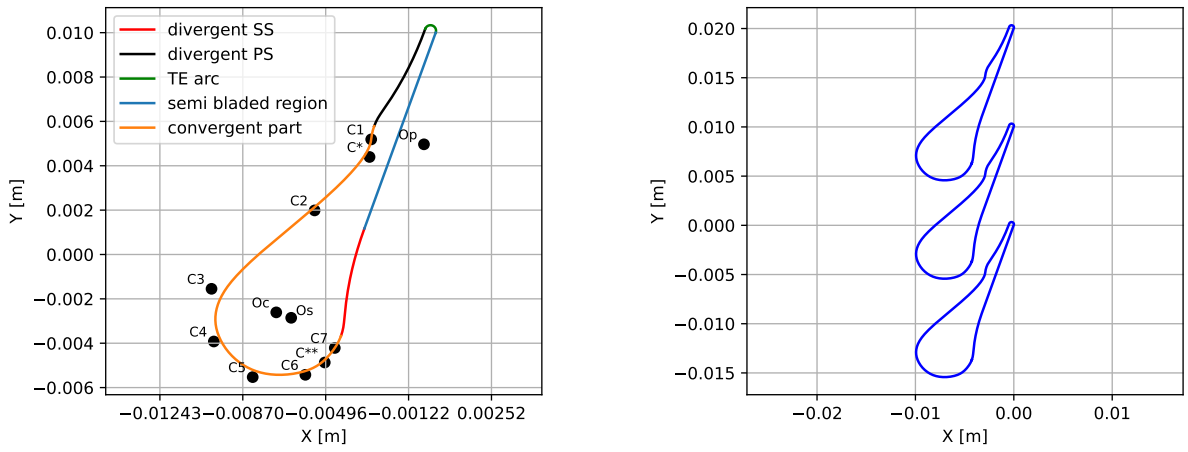

(a) (b)

Figure 4.3: (a) Control points used for the NURBs computation and (b) final blade for the CO2-70 case, see Section 4.3 for more information.

4.2. Design of a convergent-divergent stator of an axial turbine using an asymmetric MoC

A vane designed using an asymmetric MoC is quite similar, at least in its structure, to its symmetric counterpart. It is possible to identify a convergent and a divergent section, with the second designed using a MoC and the first with a continuous spline or, as here, a continuous NURBs curve. The main difference between the two is, at least in theory, the absence of the semi-bladed section in the asymmetric type, which is designed together with the divergent one using a MoC.

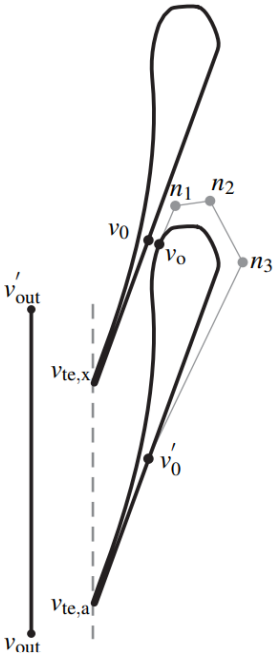

(a)

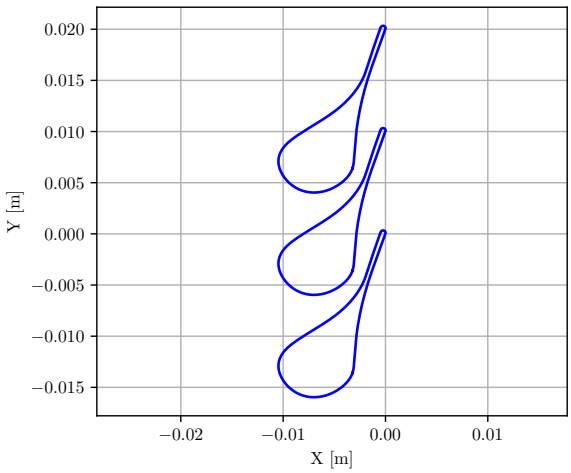

(b)

Figure 4.4: Example of (a) asymmetric blade constructed using the Anand's method [2] and (b) asymmetric blade constructed using the presented method for CO2-70, see Section 4.3 for more information.

4.2.1. Construction of the blade

The method used, as shown by Anand [2], is a variation of the one used to construct a symmetric blade, with some small changes due to the absence of the semi-bladed region. It may be summarized as follows, with the same inputs as the symmetric counterpart:

1. If not already done, the nozzle is translated along the horizontal axis so that the

throat is at $x = 0$ and is normalized with the throat height Y_t. Thus the throat is at $y = 0.5$ for the upper wall and $y = -0.5$ for the lower one and the exit area is only a function of M_d;

2. **Adaptation of the final C_+.**

   - To achieve a periodic profile, one of the main conditions is to align all the trailing edges along a given direction, such as the vertical one in the case considered here, at a pitch-wise distance from each other.
   - Because in the case of a symmetric profile, the end of the divergent part is inside the blade passage, this is not a concern. However, it becomes an issue for an asymmetric one, where the nozzle outlet is also the outlet of the blade, forcing the last C_+ to be vertical after the rotation.
   - Mathematically, this means that

$$90 = \alpha + \varphi_a \tag{4.2}$$

     where $\alpha = \sin(1/M_d)$ and φ_a is the outlet metal angle. This relation forces to have only one M_d, which may be nonacceptable, for every value of φ_a. For example, if we consider a $\varphi_a = 70$, that is an acceptable exit angle for this type of vanes [2], $\alpha = 20$ and as a consequence M_d=2.92.

   - To resolve this problem, a new angle:

$$\alpha_g = 90 - \varphi_a \tag{4.3}$$

     is found, as a function of the outlet metal angle only. This angle is used to compute the slope of the straight line that links the ends of the upper and lower walls so that they are aligned along the vertical direction after the rotation. To achieve this, one of the walls is stretched, causing the presence of a semibladed section, although shorter compared to a symmetric counterpart. This solution has also been implemented by Anand [2].

3. **Scaling and transformation of the nozzle geometry**.

   - The modified nozzle is now scaled by a factor

$$L = \frac{p}{l(end\ upper\ wall, end\ lower\ wall)} \tag{4.4}$$

where the nondimensional exit area, equal to the distance between the ends of the two nozzle walls, is equal to the pitch.

- After scaling, the nozzle is rotated by an angle $\varphi_a + |\theta|$ about the center of the throat, where θ is the direction of the velocity at the nozzle outlet.

4. **Nozzle translation**.
   - With the point ss^*_{te} positioned at (0,0), the point ps^*_{te} is placed at a distance t_{TE} from ss^*_{te} along the orthogonal to the endpoint of the nozzle.
   - Then, the points ss_{te} and ps_{te} are placed to a vertical distance p from ss^*_{te} and ps^*_{te} respectively.
   - The nozzle walls are now translated so that the end of the upper and lower ones are coincident with ss_{te} and ps^*_{te} respectively.
   - The pressure side is then translated vertically of a vertical distance equal to p so that its end is coincident with ps_{te}.
5. **Trailing edge construction**.
   - The trailing edge is drawn as a circumferential arc of radius $t_{TE}/2$ that connects ss_{te} with ps_{te}. Its center is in the midpoint of the ss_{te}-ps_{te} straight line.
6. **Converging section**.
   - The converging section is formed by a continuous NURBs curve, implemented in the Python code using the package presented in [48] that connects PSo with SSo passing through the control points $C1 - C7$.
   - These control points are computed as a function of the radius of curvature of the upper wall k. $C1$ is positioned at a distance of $0.5k$ from PSo along the tangent to this last point, $C7$ is computed in the same way but with respect to SSo and positioned at a distance of $0.3k$.
   - $C2$ is along the orthogonal of the divergent suction side at a distance $Coeff2{*}k$, where $Coeff2$ is a function of the desired shape. The position where the orthogonal line is computed is at a distance $CoeffL2 * l_{ps}$ from ss_{te}, where l_{ps} is the length of the pressure side divergent part.
   - Points $C3 - C6$ are computed in the same way as the symmetric case.

Even before the start of the CFD simulations, a problem can be observed: the zone of minimum thickness is not at the trailing edge as usual, but at point PSo, due to how the

divergent walls are constructed by the MoC. Specifically, considering that at the trailing edge, the two sides are parallel, the curvature of the pressure side tends to approach the suction one. This problem can be limited by employing a high radius of curvature for the lower wall, limiting the length of the divergent pressure side, or potentially resolved using a concordant asymmetric MoC. However, it is important to note that the effectiveness of the concordant asymmetric MoC solution has not been tested in this work. This issue does not occur in the version developed by Anand because the lower wall is a straight line.

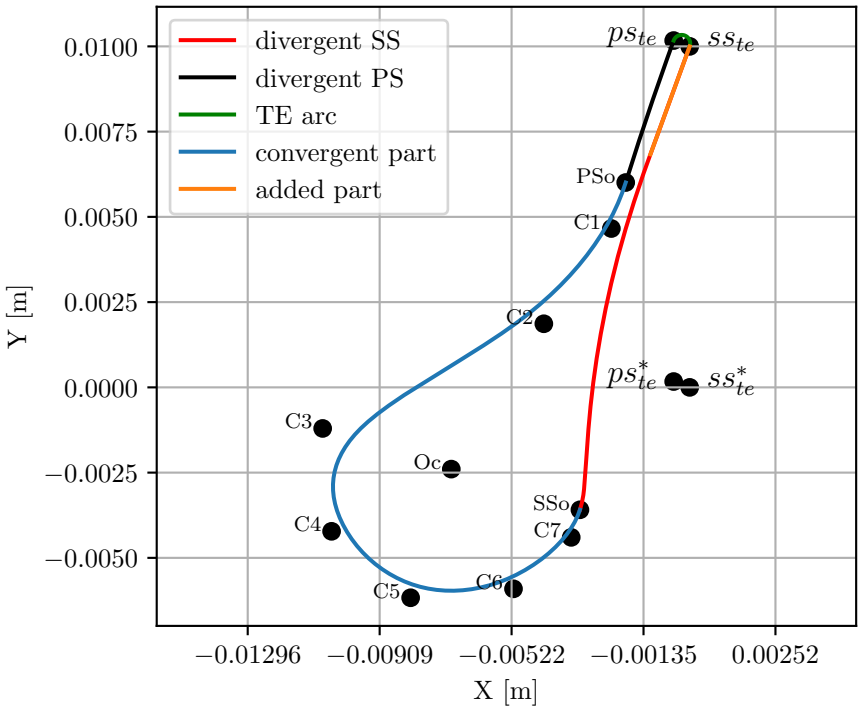

Figure 4.5: Representation of the parts in which an asymmetric blade is divided and the points used to construct the converging section.

4.2.2. Shape of the convergent part and its effects on the flow in a divergent nozzle

A potential observation that may arise when examining the proposed asymmetric blade is that the converging section near the throat is different significantly from the one used to initialize the MoC. This deviation is quite uncommon, as can be observed in blades from the literature presented here, as well as the symmetric one developed, where the convergent section typically attempts to mimic the geometry used for the initial-value line computation. This is true also for the asymmetric vane presented by Anand, see Figure

4.4a, where the throat section is quite similar to the geometry of half of a symmetric nozzle.

To determine whether it is possible to deviate from the prescribed convergent geometry provided by the initialization method, a test has been carried out for both symmetric and asymmetric MoC. The approach involves considering the previously studied SH2 case and designing two different versions: one with a higher slope than a circular arc in the vicinity of the throat and one with a lower slope. These two variations are then simulated and the computed flow field is compared to the one obtained using a standard circular arc as a converging section.

To design the new convergent part a Bèzier curve has been used using four control points. To adjust the slope, its starting point is held at a constant vertical position, as this quantity is a function of the desired inlet Mach. Using the position of the circular arc starting point as a reference, the Bèzier curve starting point is shifted nearer or further from the throat.

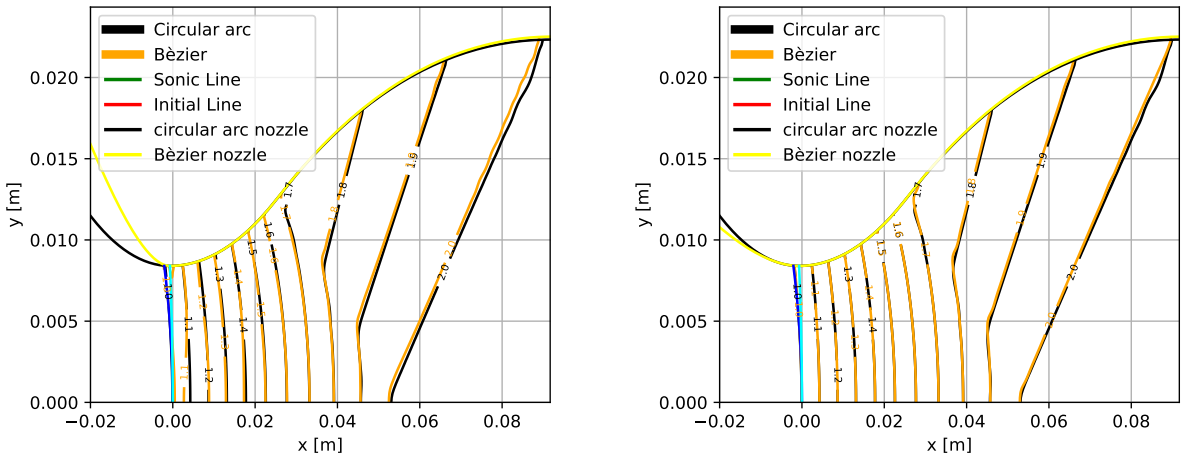

(a) (b)

Figure 4.6: Comparison between the flow field with the convergent part draw as a circular arc and a Bèzier curve with (a) higher and (b) lower slope for a symmetric nozzle.

The conclusions are consistent for both symmetric and asymmetric: with a higher slope (see Figures 4.6a and 4.7a), some differences between the iso-lines are present, especially for the asymmetric nozzle. In the case of a lower slope (see Figures 4.6b and 4.7b), the iso-lines between the circular arc and Bèzier curve cases are near coincident. With the exclusion of the asymmetric case with a higher slope, all the treated cases predict the flow field with acceptable accuracy. Interestingly in all four case studies, Bèzier's reflex

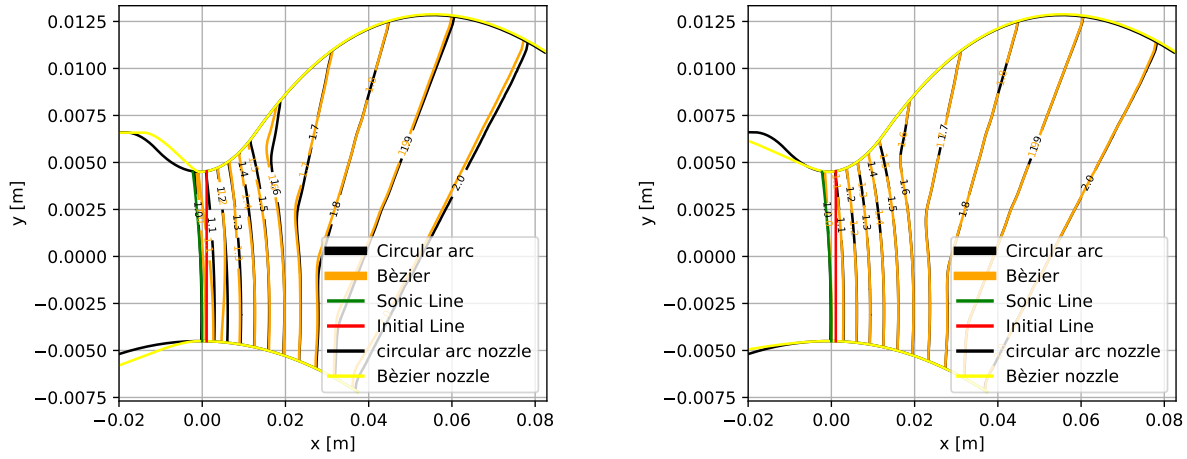

(a) (b)

Figure 4.7: Comparison between the flow field with the convergent part draw as a circular arc and a Bèzier curve with (a) higher and (b) lower slope for an asymmetric nozzle.

region presents a slightly higher passage area. Considering that the mass flow is equal to their circular arc counterparts, a possible explanation may be a slightly different end of the kernel region, causing a very limited shift of the wall.

4.3. Comparison between symmetric and asymmetric blades: similarities and differences

Here, a comparison between the blades designed using symmetric and asymmetric MoC is presented. Three cases for each blade type are reported. The common data between all the cases include the pitch $p = 10$ mm, the trailing edge thickness $t_{TE} = 0.5$ mm, the throat height $Y_t = 18$ mm, the outlet Mach number equal to 2, and the radius of curvature of the higher wall (the only one for the symmetric vane) equal to $3Y_t/2$ and $100Y_t/2$ for the lower one. The main differences are presented by the fluid, the total inlet conditionts, and φ_a. For the first case, CO_2 is selected as the fluid, with total quantities $T_t = 500$ C, $P_t = 200$ bar, and $\varphi_a = 70°$, giving the case name $CO2-70$. The second and third cases are called $MDM-70$ and $MDM-65$. The quantities in common are the fluid used, MDM, and the total condition at $P_t = 8$ bar, and $T_t = 272C$ [49]. The only difference is the outlet, selected respectively equal to $\varphi_a = 70$ and $\varphi_a = 65$.

All the simulations are viscous, so the k-ω-SST turbulence model has been used, initializing it with a turbulence intensity equal to 5% and a length scale equal to the blade chord. The mesh has been realized using *Ansys*® Turbogrid Student Version 2023 R1

with a total number of nodes equal to 500k, just below the limit of 512k of the student version of Fluent, and a total number of elements around 330k. Because Turbogrid can produce only three-dimensional mesh, in reality, a quasi-three-dimensional simulation has been made. For this reason, two spanwise layers with nearly 160k elements for each one are preset. These layers are created by stacking spanwise the same profile and applying a symmetric boundary condition. For the inlet, situated at half a chord from the profile, total pressure and temperature, as well as the flow direction are fixed. At the outlet, situated at three chords from the profile, the average pressure has been fixed, accepting a maximum oscillation of 5% from the mean. Periodic conditions are then used for the walls that connect the sides of the two layers. As it is possible to observe in Figures 4.15, the value of y^+ along the profiles is always below 2.5.

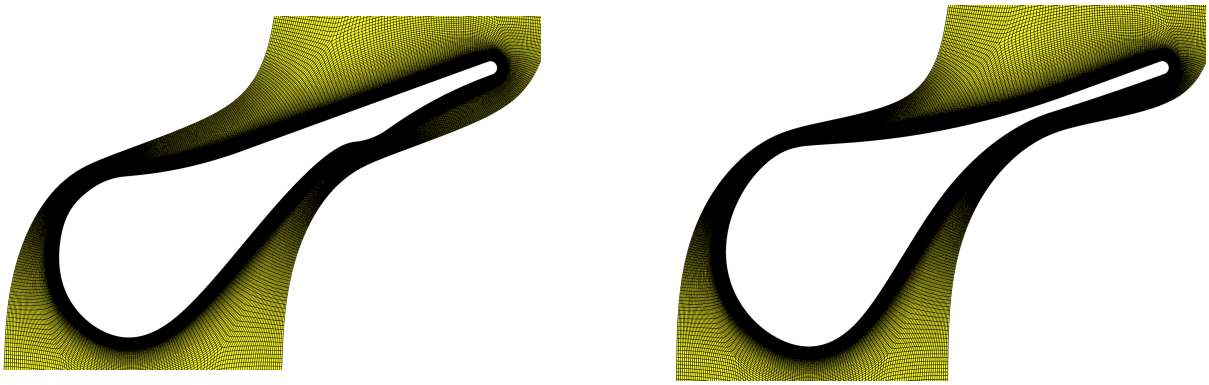

(a) (b)

Figure 4.8: Particular of the mesh for (a) symmetric and (b) asymmetric CO2-70.

4.3.1. Performance assessment of the designed blade

The initial observation (see Figures 4.10, 4.11, and 4.12) reveals a complete absence of shocks within the blade passage for all the cases considered. Fish-tails are visible at the blades trailing edge, but their presence is anticipated. Regarding the expansion, a higher gradient in the kernel region is evident for the symmetric cases, along with slightly stronger fish-tail shocks.

By analyzing the losses expressed as functions of the pressure losses reported in Table 4.1, it is possible to determine that the symmetric stator guarantees equal or lower losses compared to the asymmetric counterpart, as also observed by Anand [2]. These losses are high but comparable to the ones found in the literature. For example, the case presented by Persico et al. [49] shows, in the baseline blade, $Y = 18.3\%$ for the same thermodynamic condition and near the same exit angle as MDM-70.

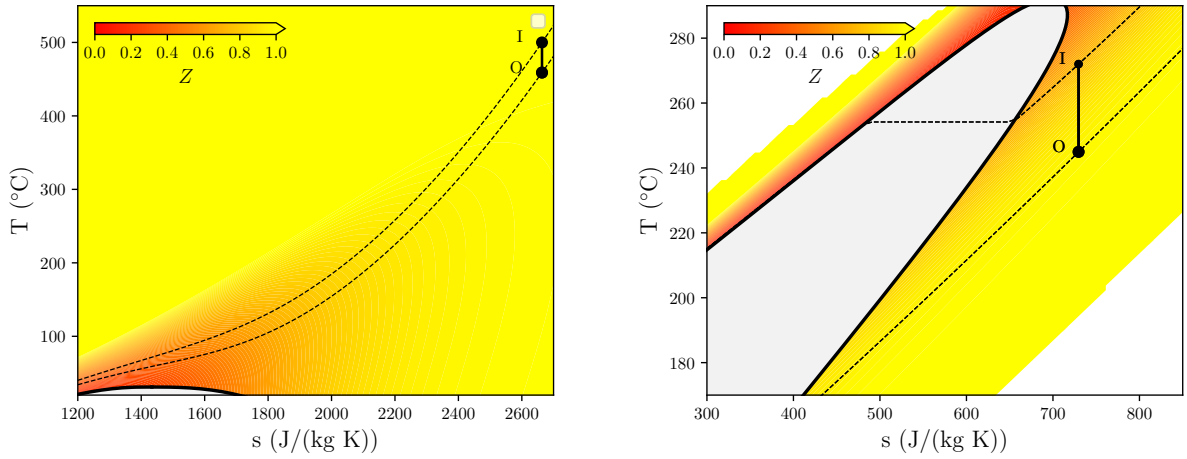

Figure 4.9: T-s plane with the computed value of Z for the isentropic expansion in the case of(a) $C0_2$ and (b) MDM for the thermodynamic conditions used for the test of the blades.

The Mach numbers at one axial chord downstream of the profile are consistently lower than the design values (see Table 4.1), probably due to the formation of the boundary layer, which is not adequately considered by a boundary layer correction on the divergent part designed by the MoC. The symmetric cases generally exhibit higher Mach number and lower outlet velocity angle than their asymmetric counterparts. From this observation, it is evident that a blade design using a symmetric MoC is more aligned with the design data. If the pitchwise distribution of the aforementioned quantities is observed, see Figure 4.13, it is possible to notice that the outlet flow angle presents a higher maximum and lower minimum for the asymmetric case, which, in general, present also a less uniform flow. Except for the $CO2-70$ case, where the difference in the flow velocity due to the presence of the wake and the fish-tail shocks are limited, this behavior is also present in the evolution of the Mach number.

If we observe the blade loading (see Figure 4.14), it is apparent at which streamwise position the fish-tail shocks make contact with the suction side. The position is always at lower streamwise in the asymmetric case. At the same streamwise position, a symmetric blade exhibits lower pressure on both the suction and pressure sides, indicating that the expansion occurs earlier than with an asymmetric blade.

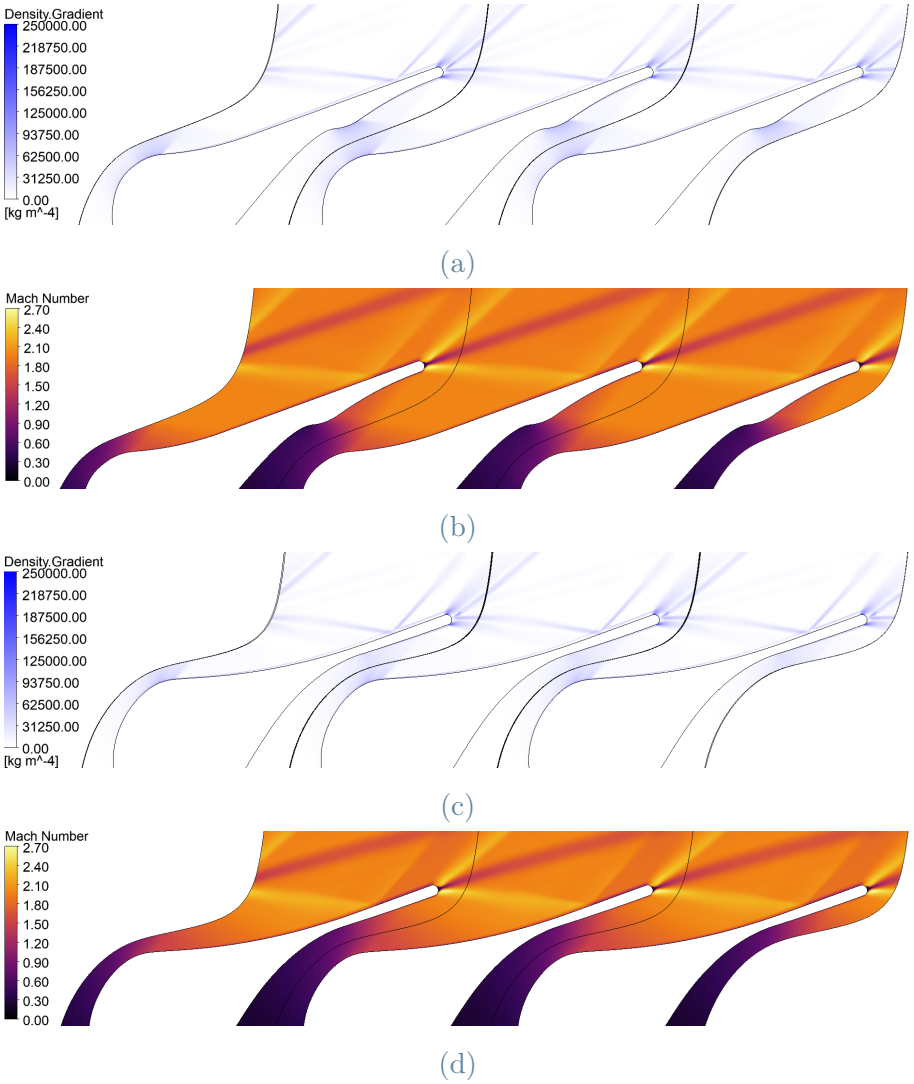

Figure 4.10: (a) Density gradient and (b) Mach for CO2-70 symmetric. (c) Density gradient and (d) Mach for CO2-70 asymmetric.

	Symmetric			**Asymmetric**		
Case	Y [%]	M	φ_a [°]	Y [%]	M	φ_a [°]
CO2-70	17	1.9	71.96	17	1.88	73.98
MDM-70	19.3	1.87	73.2	24.3	1.83	75.73
MDM-65	15.8	1.88	68.80	18.7	1.87	72.00

Table 4.1: Pressure losses computed as $Y = \frac{P_{t,in} - P_{t,out}}{P_{t,in} - P_{out}}$ and mass-weighted value of Mach number and outlet flow angle for the analyzed cases at one axial chord downwind of the profile, where the quantities P_t and $P_{t,out}$ are also computed.

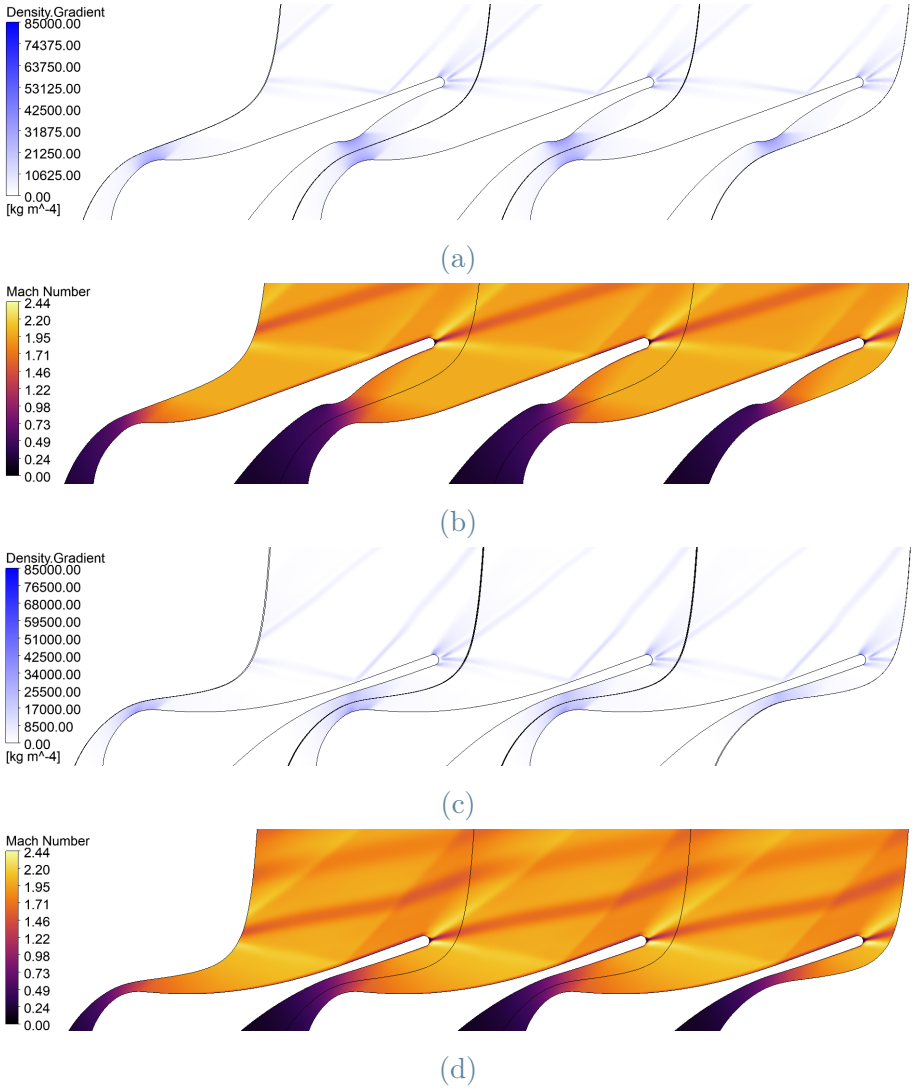

Figure 4.11: (a) Density gradient and (b) Mach for MDM-70 symmetric. (c) Density gradient and (d) Mach for MDM-70 asymmetric.

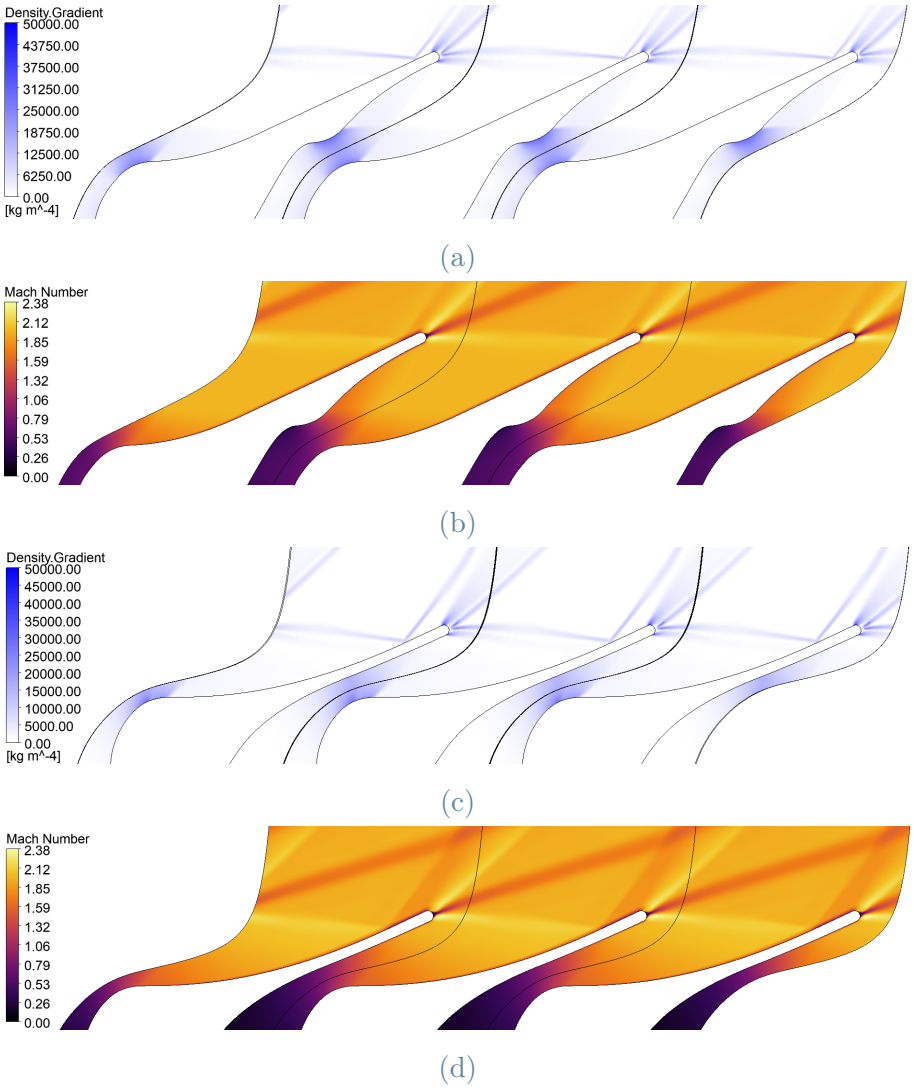

Figure 4.12: (a) Density gradient and (b) Mach for MDM-65 symmetric. (c) Density gradient and (d) Mach for MDM-65 asymmetric.

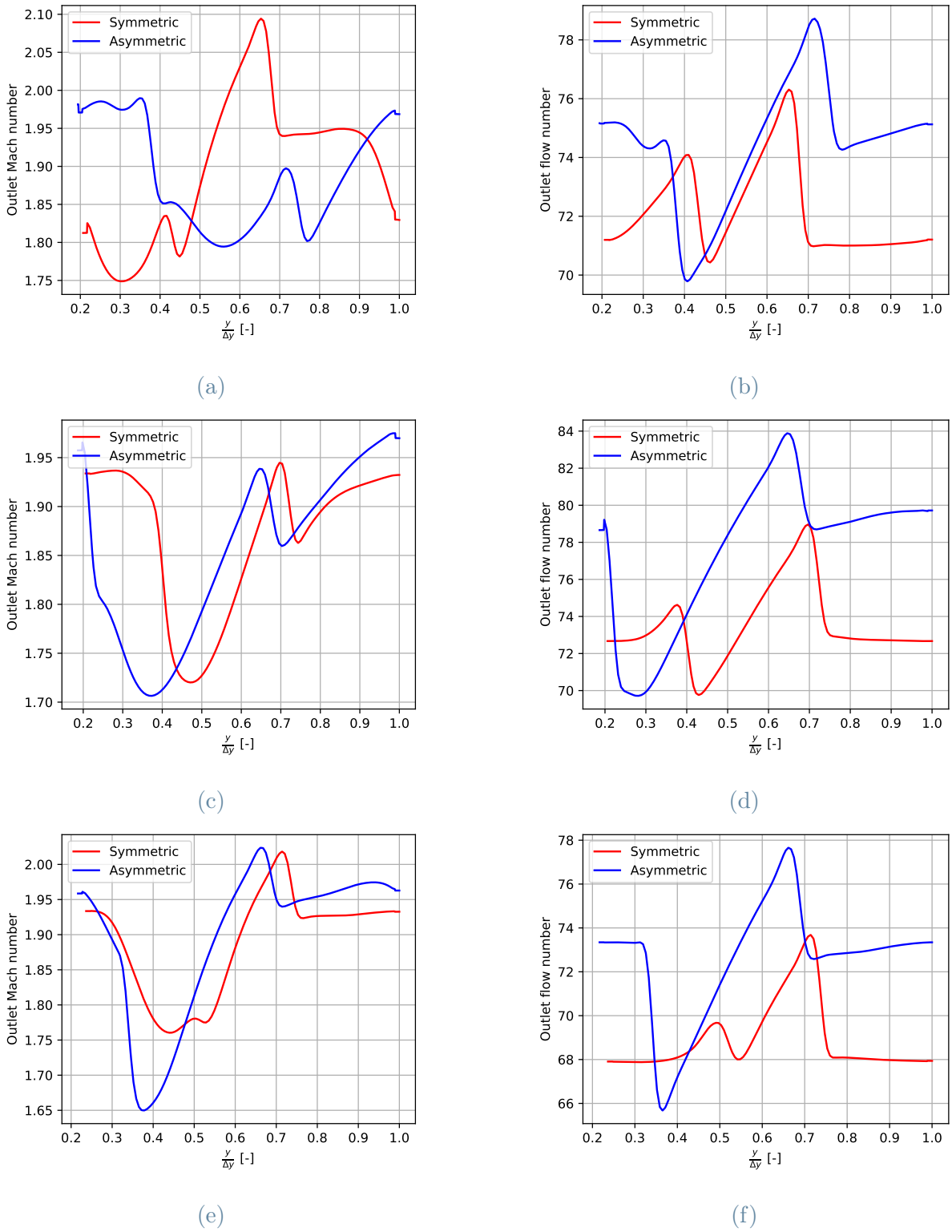

Figure 4.13: Flow properties at one axial chord from the trailing edge (a) Mach and (b) flow angle for CO2-70. (c) Mach and (d) flow angle for MDM-70. (e) Mach and (f) flow angle for MDM-65.

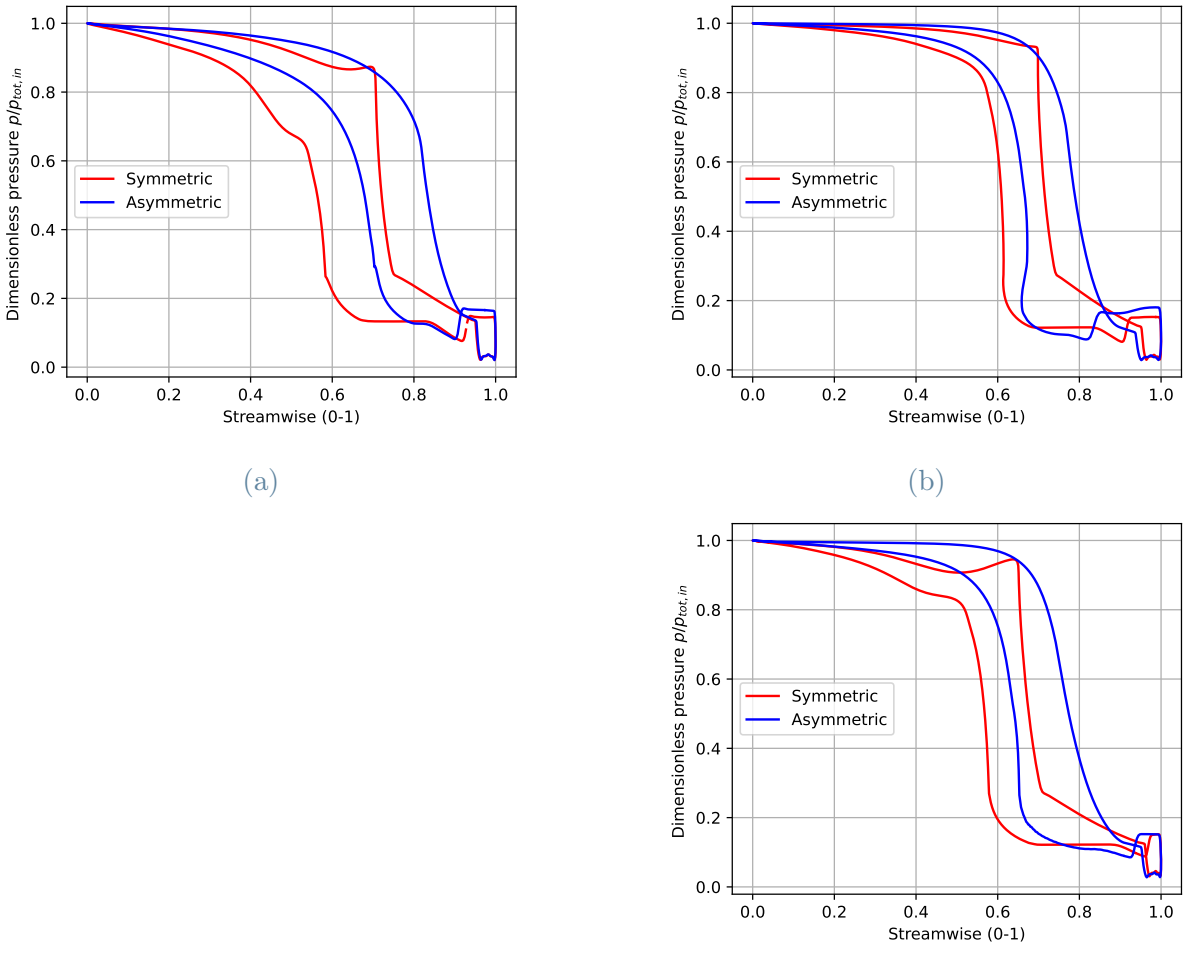

(a)

(b)

(c)

Figure 4.14: Dimensionless blade loading distribution for (a) CO2-70, (b) MDM-70 (c) MDM-65.

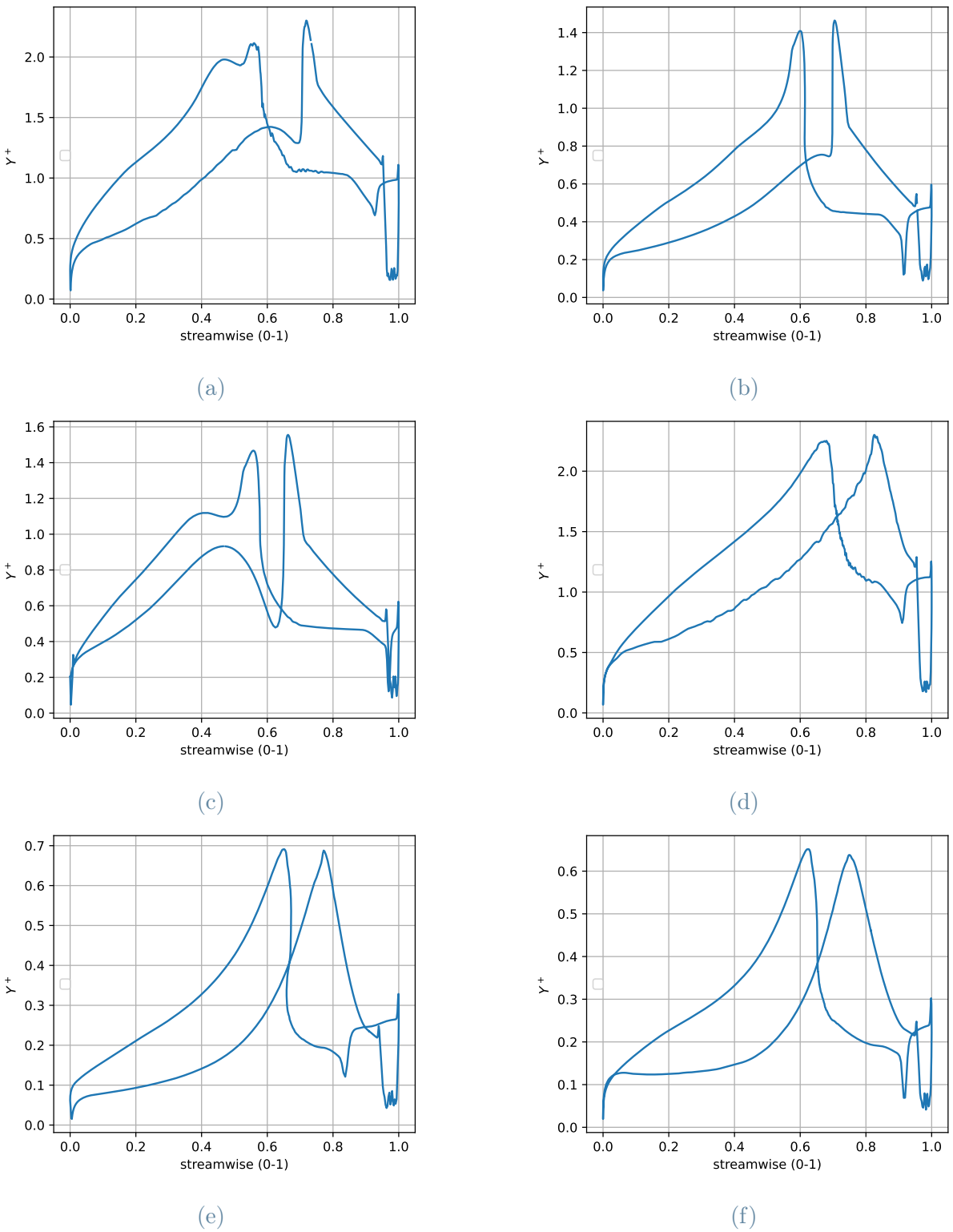

Figure 4.15: Value of Y^+ for (a) CO2-70, (b) MDM-70 and (c) MDM-65 symmetric. Value of Y^+ for (d) CO2-70, (e) MDM-70 and (f) MDM-65 asymmetric.

5 | Conclusions

In this thesis, two MoCs have been developed and subsequently extended to the design of converging-diverging nozzle cascades. In pursuing this, two potential geometries for divergent nozzles were explored—symmetric and asymmetric—to discern whether there is a means to enhance the efficiency of a supersonic turbine.

The motivation for this work stems from the growing interest in this technology in recent years, owing to its potential applications in a range of low-carbon technologies that can contribute to decarbonization. To achieve this goal, it is imperative to enhance the efficiency of these turbines, for both economic and environmental reasons.

In the initial section of the dissertation, a symmetric planar MoC has been implemented in Python and verified through dedicated CFD simulations for both perfect and non-ideal flows. While the first case has successfully passed its verification, it is unable to predict flows with pronounced non-ideal effects, which can be prevalent in various real-world applications, for example, an ORC expander. This limitation is well-documented in the literature and is the primary reason why a non-ideal equation of state must be employed when the goal is to design a nozzle inside which the desired expansion happens.

The development of these two codes has also showcased a significant advantage of the MoC presented by Zucrow and Hoffman: the main code is entirely decoupled from the equation of state used to define the speed of sound. This means that it is ready for any model necessary to describe the desired flow. This stands in contrast, for example, with the method presented by Anderson, where a Prandl-Meyer angle must be computed, and thus, the type of flow directly affects the main algorithm. It is also noteworthy that there is no direct expression to compute the Prandtl-Meyer angle for a non-ideal and non-polytropic flow, necessitating an additional iterative cycle to calculate it

Another noteworthy observation pertains to the type of prescribed wall: in this case, as well, the method used to compute the intersection point and the local slope is decoupled from the main algorithm. Consequently, any change in its shape, if necessary, can be implemented straightforwardly.

Deriving a model for transonic non-ideal flow in the vicinity of the throat from an ideal one is not a straightforward process. It involves more significant modifications to the theory used in deriving the original model. To describe this part of the flow, two models have been employed: one based on Γ and devised by Guardone, and another based on k developed in this thesis.

Conceptually, the two aforementioned models are similar as they both describe the relationship between the flow field velocity and the speed of sound through two non-dimensional quantities traditionally used to characterize a non-ideal flow. Both of these quantities express how a gas behaves during an expansion. Additionally, the main assumption made, that their values are constant and equal to their value in the sonic state in the vicinity of the throat, is in common between the two models. The perturbation equation for the k-model is arguably easier to derive from the perfect one, but this represents the only difference between them.

The two aforementioned models, along with the general planar symmetric MoC, have successfully passed the verification process. This demonstrates their capability to design a shock-free nozzle and accurately describe the flow inside it for different fluids, geometries, and levels of flow non-ideality.

The only critical points identified are the slight difference in mass flow when computed at the throat and at the end of the nozzle, and the potential existence, in certain cases, of small shocks at the interface between the kernel and the reflex region. These shocks are attributed to a non-perfectly C^2 connection between the prescribed wall and the turning contour. While the former has no significant effects on the flow inside the nozzle, the same cannot be definitively asserted for the latter. However, as demonstrated by the results, the presence of this shock does not have a disruptive effect on the efficiency of the expansion.

In the third chapter, the planar asymmetric MoC with opposite curvature has been developed and verified, with a specific emphasis on highlighting the main differences from its symmetric counterpart.

Even though the literature on it is relatively poor compared to a symmetric MoC, the conceptual similarities between the two have facilitated a relatively straightforward derivation of the asymmetric MoC from the symmetric one. Thanks to these similarities, it is theoretically possible and suggested to develop a code that implements both cases.

The primary challenges in implementing this method lie in modeling the flow in the vicinity of the throat, thus defining the initial-value line, and ensuring a C^2 turning

contour.

The first difficulty is promptly addressed by the model devised by Zocca et al., which provides a mathematical representation of the non-ideal flow in the vicinity of the throat for this specific geometry by adapting the theory developed by Sauer for the description of a transonic flow along a profile. The non-ideal formulation is based on the Γ-model. However, it can be readily reformulated for the k-model using the knowledge obtained during the derivation of the same model for the symmetric case.

The resolution of the second difficulty is accomplished by translating the initial line to a higher Mach number to decrease the extension of the low accuracy zone and reshaping the turning contour to delete the zones that are not C^2. From these solutions, two observations can be made. The first one is that it is possible to move the initial-value line in a relatively unconstrained manner, ensuring that $M > 1$ along the entire initial-value line and that the Mach number remains slightly higher than one, maintaining the validity of the small perturbation model. The second observation is that very limited modifications of the turning contour are possible and, in some cases, also beneficial. In this case, as well, the verification can be considered successful for both the initialization method and the general MoC.

Finally, the two previously defined MoCs are extended to the design of nozzle cascades for axial turbines, but the results are not as positive. The asymmetric MoC has been developed to enhance the efficiency of vanes by designing the semibladed region with a studied method, rather than as a simple curve connecting the end of the divergent part of the suction side with the trailing edge while keeping the exit angle constant.

However, by comparing the two different types of blades for various cases, it is evident that the symmetric blade arguably remains the preferable choice. It exhibits lower losses and an outlet flow closer to the design target compared to the asymmetric counterparts. These differences align with the observations made by Anand in his study on asymmetric vanes, which, to be precise, are constructed by an asymmetric MoC consisting of a curve and a straight line, and not by two curves. The design algorithm of the asymmetric case is still in its preliminary stages and future refinement can alter the reported conclusion.

Another peculiar aspect is the pressure side of the presented asymmetric vane, which has its section of minimum thickness in the interface between the converging and diverging parts of the blades. Further investigation is likely necessary to understand the potential effects of this unusual characteristic.

In conclusion, several future developments regarding the treated topics are possible. Here

are some examples:

- To ensure that the turning contour is made by a C^2 curve, an indirect upper and lower point unit may be employed as a substitution for the two solutions presented here. The use of these process units, implemented following Hoffman and Zucrow, although more complex from a development point of view, can be more straightforward for a user.
- The asymmetric MoC with concordant curvature may be developed, allowing a larger design space for both nozzles and nozzle cascades. It is worth noting that this type of MoC has already been formulated by Zocca et al.
- An investigation of the extension of an asymmetric MoC with concordant curvature to nozzle cascades is necessary, focusing on whether this method can shift the section with minimum thickness in the correspondence of the trailing edge.
- More in-depth investigations of blade design with asymmetric MoC for both radial and axial turbines are necessary. For example, understanding the behavior of this type of blade in a three-dimensional simulation, and exploring how off-design conditions affect performance.

In summary, the importance of supersonic turbines is expected to increase in the next years, along with the need for more refined methods to enhance their efficiency. The utilization of nozzle cascades designed employing asymmetric MoC may be beneficial for this purpose, but further investigations are necessary to understand if the added flexibility of this design methodology can be effectively exploited.

Bibliography

[1] Various authors. *World Energy Outlook 2022*. OECD, 10 2022. ISBN 9789264425446. doi: 10.1787/3a469970-en.

[2] Nitish Anand. Progress in cfd-based automated design with application to unconventional turbomachines. 10 2021. doi: 10.4233/uuid:9d050254-0ff8-4f1c-81e0-15b02450edc6.

[3] April Lee, Owen Zinaman, Jeffrey Logan, Morgan Bazilian, Douglas Arent, and Robin L. Newmark. Interactions, complementarities and tensions at the nexus of natural gas and renewable energy. *The Electricity Journal*, 25:38–48, 12 2012. ISSN 1040-6190. doi: 10.1016/J.TEJ.2012.10.021.

[4] Antonio García-Olivares, Jordi Solé, and Oleg Osychenko. Transportation in a 100% renewable energy system. *Energy Conversion and Management*, 158:266–285, 2 2018. ISSN 0196-8904. doi: 10.1016/J.ENCONMAN.2017.12.053.

[5] Paolo Chiesa, Giovanni Gustavo Lozza, and Luigi Mazzocchi. Using hydrogen as gas turbine fuel. *Journal of Engineering for Gas Turbines and Power-transactions of The Asme*, 127:73–80, 2003. URL `https://api.semanticscholar.org/CorpusID:15261675`.

[6] Jia Qi Guo, Ming Jia Li, Ya Ling He, Tao Jiang, Teng Ma, Jin Liang Xu, and Feng Cao. A systematic review of supercritical carbon dioxide(s-co2) power cycle for energy industries: Technologies, key issues, and potential prospects. *Energy Conversion and Management*, 258:115437, 4 2022. ISSN 0196-8904. doi: 10.1016/J.ENCONMAN.2022.115437.

[7] Piero Colonna, Emiliano Casati, Carsten Trapp, Tiemo Mathijssen, Jaakko Larjola, Teemu Turunen-Saaresti, and Antti Uusitalo. Organic rankine cycle power systems: From the concept to current technology, applications, and an outlook to the future. *Journal of Engineering for Gas Turbines and Power*, 137, 10 2015. ISSN 15288919. doi: 10.1115/1.4029884.

[8] Jorge Sousa, Guillermo Paniagua, and Elena Collado Morata. Thermodynamic anal-

ysis of a gas turbine engine with a rotating detonation combustor. *Applied Energy*, 195:247–256, 6 2017. ISSN 0306-2619. doi: 10.1016/J.APENERGY.2017.03.045.

[9] Sriraj Gokarakonda, Peter Hennicke, Christopher Moore, Stefan Thomas, and Maike Venjakob. Relevant technologies for the energy transition in germany, with potential relevance for japan : a preparatory study in the framework of the gjetc project, 2018. URL `http://nbn-resolving.de/urn:nbn:de:bsz:wup4-opus-69911`.

[10] T. P. Moffitt. Design and experimental investigation of a single-stage turbine with a rotor entering relative mach number of 2, 1958. URL `https://ntrs.nasa.gov/citations/19630010654`.

[11] Sylvain Quoilin, Martijn Van Den Broek, Sébastien Declaye, Pierre Dewallef, and Vincent Lemort. Techno-economic survey of organic rankine cycle (orc) systems. *Renewable and Sustainable Energy Reviews*, 22:168–186, 6 2013. ISSN 1364-0321. doi: 10.1016/J.RSER.2013.01.028.

[12] Damiano Perusi and Marco Astolfi. Comparison between direct and indirect orcs for csp applications. 5^{th} International Seminar on ORC Power Systems, September 9-11, 2019.

[13] E Bufi. Robust optimization of orc turbine expanders. *Theses, Ecole nationale supérieure d'arts et métiers-ENSAM*, 2016.

[14] Olgun Konur, C. Ozgur Colpan, and Omur Y. Saatcioglu. A comprehensive review on organic rankine cycle systems used as waste heat recovery technologies for marine applications. *Energy Sources, Part A: Recovery, Utilization, and Environmental Effects*, 44:4083–4122, 6 2022. ISSN 1556-7036. doi: 10.1080/15567036.2022.2072981.

[15] Sebastian Eyerer, Fabian Dawo, Christopher Schifflechner, Anne Niederdränk, Hartmut Spliethoff, and Christoph Wieland. Experimental evaluation of an orc-chp architecture based on regenerative preheating for geothermal applications. *Applied Energy*, 315, 6 2022. ISSN 03062619. doi: 10.1016/j.apenergy.2022.119057.

[16] David Baumgärtner. Real gas effects in orc turbines. 2021. doi: 10.17863/CAM.69867. URL `https://www.repository.cam.ac.uk/handle/1810/322410`.

[17] A. V. Srimvasan. Flutter and resonant vibration characteristics of engine blades. *Journal of Engineering for Gas Turbines and Power*, 119:742–775, 10 1997. ISSN 0742-4795. doi: 10.1115/1.2817053. URL `https://dx.doi.org/10.1115/1.2817053`.

[18] Andrew P.S. Wheeler and Jonathan Ong. The role of dense gas dynamics on organic

rankine cycle turbine performance. *Journal of Engineering for Gas Turbines and Power*, 135, 2013. ISSN 07424795. doi: 10.1115/1.4024963.

[19] M J Zucrow and J D Hoffman. *Gas Dynamics Volume 2*. Krieger Publishing Company, 1977. ISBN 9780898748406. URL https://books.google.it/books?id=Pa3vAAAAMAAJ.

[20] A W Reichert and H Simon. Design and flow field calculations for transonic and supersonic radial inflow turbine guide vanes, 1995. URL http://asmedigitalcollection.asme.org/GT/proceedings-pdf/GT1995/78781/V001T01A022/2406016/v001t01a022-95-gt-097.pdf.

[21] Marta Zocca, Antti Uusitalo, Teemu Turunen-Saaresti, and Alberto Guardone. Method of characteristics-based design and numerical simulation of a micro-orc supersonic turbine nozzle ring. 5^{th} International Seminar on ORC Power Systems, September 9-11, 2019.

[22] Marta Zocca, Paolo Gajoni, and Alberto Guardone. Nimoc: A design and analysis tool for supersonic nozzles under non-ideal compressible flow conditions. *Journal of Computational and Applied Mathematics*, page 115210, 3 2023. ISSN 03770427. doi: 10.1016/j.cam.2023.115210. URL https://linkinghub.elsevier.com/retrieve/pii/S0377042723001541.

[23] M J Zucrow and J D Hoffman. *Gas Dynamics, Volume 1*. Wiley, 1976. ISBN 9780471984405. URL https://books.google.it/books?id=uqzvAAAAMAAJ.

[24] J D Anderson. *Modern Compressible Flow: With Historical Perspective*. McGraw-Hill, 2004. ISBN 9780071241366. URL https://books.google.it/books?id=bdy_PwAACAAJ.

[25] Julián C. Restrepo, Andrés F. Bolaños-Acosta, and José R. Simões-Moreira. Short nozzles design for real gas supersonic flow using the method of characteristics. *Applied Thermal Engineering*, 207:118063, 5 2022. ISSN 1359-4311. doi: 10.1016/J.APPLTHERMALENG.2022.118063.

[26] Nitish Anand, Salvatore Vitale, Matteo Pini, Gustavo J. Otero, and Rene Pecnik. Design methodology for supersonic radial vanes operating in nonideal flow conditions. *Journal of Engineering for Gas Turbines and Power*, 141, 2 2019. ISSN 15288919. doi: 10.1115/1.4040182.

[27] Sauer R. General characteristics of the flow through nozzles at near critical

speeds - nasa technical reports server (ntrs), 1947. URL https://ntrs.nasa.gov/citations/20050019415.

[28] Ian M Hall. Transonic flow in two-dimensional and axially-symmetric nozzles. *Quarterly Journal of Mechanics and Applied Mathematics*, 15:487–508, 1962. URL https://api.semanticscholar.org/CorpusID:119968561.

[29] Lloyd H Back, H L Gier, and Paul F Massier. Comparison of measured and predicted flows through conical supersonic nozzles, with emphasis on the transonic region. *AIAA Journal*, 3:1606–1614, 1965. URL https://api.semanticscholar.org/CorpusID:118685906.

[30] Lloyd H Back, Robert Cuffel, and Paul F Massier. Transonic flowfield in a supersonic nozzle with small throat radius of curvature. *AIAA Journal*, 7:1364–1366, 1969. URL https://api.semanticscholar.org/CorpusID:117855932.

[31] James R Kliegel and Jay N Levine. Transonic flow in small throat radius of curvature nozzles. *AIAA Journal*, 7:1375–1378, 1969. URL https://api.semanticscholar.org/CorpusID:117767823.

[32] S Croquer, S Poncet, and Z Aidoun. Turbulence modeling of a single-phase r134a supersonic ejector. part 1: Numerical benchmark. *international journal of refrigeration*, 61:140–152, 2016.

[33] E W Lemmon, I H Bell, M L Huber, and M O McLinden. Nist standard reference database 23: Reference fluid thermodynamic and transport properties-refprop, version 10.0, national institute of standards and technology, 2018. URL https://www.nist.gov/srd/refprop.

[34] Procedure for estimation and reporting of uncertainty due to discretization in cfd applications. *Journal of Fluids Engineering*, 130, 7 2008. ISSN 0098-2202. doi: 10.1115/1.2960953. URL https://doi.org/10.1115/1.2960953.

[35] Ismail Celik and Ozgur Karatekin. Numerical experiments on application of richardson extrapolation with nonuniform grids. *Journal of Fluids Engineering*, 119:584–590, 9 1997. ISSN 0098-2202. doi: 10.1115/1.2819284. URL https://dx.doi.org/10.1115/1.2819284.

[36] Alberto Guardone, Andrea Spinelli, and Vincenzo Dossena. Influence of molecular complexity on nozzle design for an organic vapor wind tunnel. *Journal of Engineering for Gas Turbines and Power*, 135, 2013. ISSN 07424795. doi: 10.1115/1.4023117.

[37] P A Thompson. *Compressible-fluid Dynamics*. McGraw-Hill, 1971. ISBN 9780070644052. URL https://books.google.it/books?id=LP8oAQAAMAAJ.

[38] Alessandro Romei, Davide Vimercati, Giacomo Persico, and Alberto Guardone. Non-ideal compressible flows in supersonic turbine cascades. *Journal of Fluid Mechanics*, 882:A12, 2020. doi: 10.1017/jfm.2019.796.

[39] Mdm — coolprop 6.5.0 documentation. URL http://www.coolprop.org/fluid_properties/fluids/MDM.html.

[40] Ian H Bell, Jorrit Wronski, Sylvain Quoilin, and Vincent Lemort. Pure and pseudo-pure fluid thermophysical property evaluation and the open-source thermophysical property library coolprop. *Industrial & Engineering Chemistry Research*, 53:2498–2508, 2014. doi: 10.1021/ie4033999. URL http://pubs.acs.org/doi/abs/10.1021/ie4033999.

[41] Alberto Guardone. Effects of molecular complexity and reservoir conditions on the discharge coefficient of adapted planar nozzles. *Journal of Physics: Conference Series*, 633:12092, 10 2015. doi: 10.1088/1742-6596/633/1/012092.

[42] Andrea Spinelli, Giorgia Cammi, Simone Gallarini, Marta Zocca, Fabio Cozzi, Paolo Gaetani, Vincenzo Dossena, and Alberto Guardone. Experimental evidence of non-ideal compressible effects in expanding flow of a high molecular complexity vapor. *Experiments in Fluids*, 59:1–16, 8 2018. ISSN 07234864. doi: 10.1007/S00348-018-2578-0/FIGURES/10. URL https://link.springer.com/article/10.1007/s00348-018-2578-0.

[43] Nitish Anand, Piero Colonna, and Matteo Pini. Design guidelines for supersonic stators operating with fluids made of complex molecules. *Energy*, 203, 7 2020. ISSN 03605442. doi: 10.1016/j.energy.2020.117698.

[44] Clarence A Syvertson and Raymond C Savin. The design of variable mach number asymmetric supersonic nozzles by two procedures employing inclined and curved sonic lines. 1953. URL https://api.semanticscholar.org/CorpusID:109753076.

[45] C Osnaghi. *Teoria delle Turbomacchine*. Società Editrice Esculapio, 2020. ISBN 9788835896739. URL https://books.google.it/books?id=qPv9DwAAQBAJ.

[46] Martin T. White, Christos N. Markides, and Abdulnaser I. Sayma. Working-fluid replacement in supersonic organic rankine cycle turbines. *Journal of Engineering for Gas Turbines and Power*, 140, 9 2018. ISSN 15288919. doi: 10.1115/1.4038754.

[47] Eli Reshotko and Maurice Tucker. Approximate calculation of the compressible tur-

bulent boundary layer with heat transfer and arbitrary pressure gradient. 1957. URL https://api.semanticscholar.org/CorpusID:118057382.

[48] Onur Rauf Bingol and Adarsh Krishnamurthy. Nurbs-python: An open-source object-oriented nurbs modeling framework in python. *SoftwareX*, 9:85–94, 1 2019. ISSN 23527110. doi: 10.1016/j.softx.2018.12.005.

[49] Giacomo Persico, Pablo Rodriguez-Fernandez, and Alessandro Romei. High-fidelity shape optimization of non-conventional turbomachinery by surrogate evolutionary strategies. *Journal of Turbomachinery*, 141, 8 2019. ISSN 15288900. doi: 10.1115/1.4043252/726096. URL https://dx.doi.org/10.1115/1.4043252.